Universidade Federal de Minas Gerais

Curso de Pós-Graduação em Engenharia Metalúrgica e de Minas

Tese de Doutorado

"Nova metodologia de obtenção de nanopartículas de vidro bioativo, poliuretanas biodegradáveis e seus compósitos para aplicações biomédicas"

Autora: Agda Aline Rocha de Oliveira

Orientadora: Prof. Marivalda de Magalhães Pereira, Dra.

Co-orientador: Prof. Rodrigo Lambert Oréfice, Dr.

Abril 2011

Universidade Federal de Minas Gerais
Curso de Pós-Graduação em Engenharia Metalúrgica e de Minas

Agda Aline Rocha de Oliveira

NOVA METODOLOGIA DE OBTENÇÃO DE NANOPARTÍCULAS DE VIDRO BIOATIVO, POLIURETANAS BIODEGRADÁVEIS E SEUS COMPÓSITOS PARA APLICAÇÕES BIOMÉDICAS

Defesa de tese a ser apresentada ao Curso de Pós-Graduação em Engenharia Metalúrgica e de Minas da Universidade Federal de Minas Gerais
Área de Concentração: Ciência dos Materiais
Orientadora: Prof. Marivalda de Magalhães Pereira, Dra.
Co-orientador: Prof. Rodrigo Lambert Oréfice, Dr.

Belo Horizonte
Escola de Engenharia da UFMG
Abril 2011

Dedico este trabalho à minha querida mãe,
meu maior exemplo de força e superação.

AGRADECIMENTOS

A conclusão deste trabalho de tese é o término de uma grande etapa do contínuo processo de pesquisa e aprendizagem. Não o considero como o final de um trabalho, porque muitas respostas ainda precisam ser dadas, hipóteses formuladas não foram testadas, possibilidades não foram exploradas, mas acredito que a motivação para a pesquisa reside no fato de se intrigar com os resultados obtidos e, principalmente, com perguntas não respondidas. Assim, sinto-me extremamente feliz com o trabalho realizado e acredito que as contribuições geradas por ele são de grande relevância. Não foi um processo fácil, mas ao mesmo tempo foi estimulante e de grande valor para meu crescimento intelectual e pessoal.

A realização desse trabalho só foi possível porque contei com a valiosa ajuda de diversas pessoas e gostaria de deixar registrada aqui minha imensa gratidão:

À professora *Marivalda de Magalhães Pereira*, por aceitar me orientar tão prontamente, por ter sempre acreditado na minha proposta de trabalho e em minhas novas idéia. Agradeço ainda por seus ensinamentos de grande valor, sugestões e correções que contribuiram para o crescimento e consitência do trabalho, pelos recursos disponibilizados e, principalmente, pela grande amizade ao longo dessa jornada.

Ao professor *Rodrigo Lambert Oréfice*, pela disponibilidade de recursos e infra-estrutura, pelos ensinamentos, pelas correções e críticas valiosas que ajudaram muito na conclusão do trabalho.

Aos professores *Vicente Buono* e *Herman Sander Mansur*, pela compreensão e apoio como coordenadores do curso de pós-graduação e pelas dicas importantes e estímulo durante esse período.

Aos professores *Dagoberto Brandão Santos* e *Edwin Auza Vilegas*, por disponibilizarem seus laboratórios e me ajudarem sempre que precisei.

Aos professores *Claudio Luis Donnici (DEQ)* e *Roberto Moreira (Física)*, por disponibilizarem os equipamentos de infravermelho para a caracterização das amostras. Ao *Marcos Abreu Alves*, por ajudar tão prontamente na execução dos ensaios.

Agradeço à *Iaci Pereira* e *Eliane Ayres* pela constante e valiosa ajuda na etapa de desenvolvimento da metodologia de síntese da poliuretana.

À Sandhra Carvalho e à professora *Maria de Fátima Leite* pelos ensaios biológicos, que foram realizados com grande cuidado e atenção e que contribuíram imensamente com os resultados desse trabalho.

Aos alunos de iniciação científica *Luisa Lima* e *Dickson Alves de Souza* pela dedicação e disponibilidade em me ajudar durante a caracterização dos resultados.

Ao funcionário do ICB, *Jamil Oliveira*, que se prontificou, por inúmeras vezes, em liofilizar as amostras obtidas, tornando possível a obtenção dos materiais na forma de pó e espuma. A sua ajuda foi decisiva para a conclusão do trabalho.

À *Denise Sousa e Livio Jacques da Silva*, pelo tempo e dedicação dispendidos durantes os ensaios mecânicos dos materiais.

Ao *Mateus Prata*, por disponilizar o equipamento de Espalhamento Dinâmico de Luz para medidas dos diâmetros das partículas e por doar tanto do seu tempo para me ajuda na realização das análises.

A todos os meus colegas de laboratório, que ao longo do tempo se transformaram em queridos amigos, o que tornou a convivência no laboratório uma experiência muito prazerosa. Além dos já citados, gostaria de agradecer aos amigos: *Alessandra Nogueira, Alexandra Rodrigues, Carolina Lins, Elke Lemos, Ezequiel Costa, Hermes Costa, Joyce Santos, Magda Rocha, Marco Elisio, Tadeu Lima e Regina Coeli.*

Aos Professores e funcionários do Departamento de Metalurgia e de Materiais, em especial, às funcionárias *Andreia Bicalho, Ilda Batista*, *Maria Aparecida Pacheco, Nelson Azevedo e Patrícia Azevedo*, pela paciência e profissionalismo em me atender sempre a tempo e com muito carinho.

Às minhas irmãs, *Alessandra*, *Andreza e Amanda*, e sobrinhas, *Aline e Julia*, e, em especial, à minha mãe, *Ângela*, pelo amor, paciência, cuidado e apoio incondicional, que me fortaleceram tanto e me fizeram acreditar em minha capacidade.

Ao *Mateus*, pelo amor, atenção e carinho dedicados mim nos últimos anos e por sua paciência e compreensão durante os últimos meses.

Ao *Tobias* e à *Brigite*, por trazerem leveza e ternura à minha vida.

Por fim, agradeço a *Deus*, por me dar força e saúde necessárias para atingir minha meta.

Sumário

Índice de Figuras

Índice de Tabelas

Lista de Siglas e Abreviaturas

Sigla/ Abreviatura	Significado
APTES	3-aminopropyltriethoxysilane
BG	Bioactive Glass s
BGMP	Bioactive Glass Microparticles
BGNP	Bioactive Glass Nanoparticles
BPU	Biodegradable Polyurethane
BET	Brunauer-Emmett-Teller
CP	Calcium Phosphorous
DLS	Dynamic Light Scattering
DMEM	Dulbecco's Modified Eagle Medium
DMPA	2,2-Bis(Hydroxymethyl) Propionic Acid
DMSO	Dimetil Sulfóxido
FBS	Fetal Bovine Serum
FTIR	Fourier Transform Iinfrared
HS	Hard Segment
HDI	Hexamethylene Diisocyanate
HA	Hydroxyl Apatite
HZ	Hidrazine
HCA	Hydroxyl Carbonate Apatite
MTT	(3-(4,5-Dimethylthiazol)-2,5-diphenyltetrazolium bromide
NP	Nanoparticles
SA	Surface Area
SDS	Sodium Dodecyl sulfate
SEM	Scanning Electron Microscope
SS	Soft Segment
PCL	Poly(ε-Caprolactone)
PDI	Polydispersity Index
PU	Polyurethane
PVA	Polyvinyl Alcohol
SBF	Simulate Body Fluid

TEA	Triethylamine
TEM	Transmission Electron Microscope
TEOS	Tetraethyl Orthosilicate
TEP	Triethyl Phosphate
XRD	X-ray Diffraction
ρ_b	Bulk Density
ρ_s	Skeletal Density (True Density)

Resumo

Desde que foi desenvolvido por Hench como um material promissor para o reparo ósseo com elevadas bioatividade e biocompatibilidade, o vidro bioativo é objeto de estudo para diversos grupos de pesquisa. Várias investigações foam conduzidas com a finalidade de se obter vidros bioativos pelo método sol-gel na forma de materiais densos, pós e matrizes porosas. A nanotechologia fornece uma nova estratégia para o desenvolvimento de vidros bioativos, uma vez que materiais em nanoescala exibem aumento em sua biocompatibilidade e bioatividade. Sistemas compósitos nanopartículas de vidro bioativo/biopolímero vem sendo extensivamente estudados. Um dos objetivos deste trabalho é o desenvolvimento de materias compósitos produzidos a partir de nanopartículas desenvolvidas pelo método de Stober modificado. Diâmetro, composição, capacidade dispersiva e bioatividade das nanopartículas obtidas foram estudados por diversas técnicas. Foram obtidas nanopartículas (NPs) esféricas com diâmetros de 20 nm, como preparadas, e 90 nm, após tratamento térmico. As NPs apresentaram cinética de deposição da camada de hidroxiapatita e viabilidades celulares significativamente maiores que as micropartículas. Elas apresentaram boa dispersabilidade em solventes polares e podem fornecer desempenho superior no desenvolvimento de matrizes poliméricas. A fase polimérica é de extrema importância no design das propriedades dos compósitos. A alta variedade química da síntese de poliuretanas (PUs) permite que esses materiais apresentem propriedades desde elastômeros a materiais rígidos. Os produtos de degradação dos componentes da PU devem ser biocompatíveis, não tóxicos e metabolizados ou eliminados por organismos vivos. Outro objetivo desse trabalho é o desenvolvimento de uma nova rota de síntese para produzir dispersão de poliuretana com 20% de sólidos. Membranas foram obtidas pela secagem da dispersão em moldes à temperatura ambiente. Espumas porosas foram obtidas por liofilização. As membranas produzidas apresentaram 250% de deformação, e as espumas apresentaram macroporos interconectados. O estudo dos produtos de degradação da PU apresentou efeito tóxico moderado e precisa ser investigado mais detalhadamente. O objetivo final é a associação desses novos materiais produzidos em compósitos biocompatíveis, como propriedades físicas e mecânicas adequadas à *aplicação em engenharia de tecidos. Os materiais compósitos foram obtidos pela dispersão de nanopartículas de vidro bioativo em uma solução álcool polivinílico e, então, essa mistura foi adicionada à dispersão de PU, com composição de nanopartículas de 10 e 25% em massa. As membranas apresentaram 350% de deformação, e as espumas, macroporos interconectados. As espumas compósitas com 10% de nanopartículas apresentaram viabilidade celular elevada e deposição de camada de HA ao longo da superfície do material.*

Abstract

Since developed by Hench as a promising bone repairing material with high bioactivity and biocompatibility, bioactive glass has attracted extensive studies. Various investigations were directed to obtain sol–gel derived bioactive glasses as bulk, powder or porous scaffolds. Nanotechnology gives a new strategy to develop bioactive glasses, since nanoscaled biomaterials exhibit an enhanced biocompatibility and bioactivity.The development of polymer/bioactive glass has been recognized as a strategy to improve the mechanical behavior of bioactive glass-based materials. Several studies have reported systems based on bioactive glass nanoparticles/ biopolymer composites. In this work it was developed a composite system based on bioactive glass nanoparticles (BGNP), obtained by a modified Stober method. The size, composition, shape and dispersion capability of the obtained particles were studied by several techiques. The BGNP obtained have spherical shape and average size of 20 nm, as prepared, and 90 nm, after heat treatment. Nanoparticles presented significant increase in cell viability when compared to microparticles. They present good dispensability on polar solvents and could offer superior performance for developing tissue scaffolds.The polymeric phase is extremely important to design the final properties of the composites. The highly variable synthesis chemistry of segmented polyurethanes (PU's) may be exploited to generate polymers having properties ranging from very soft elastomers to very rigid plastics. In addition to the physical properties, a great care has to be taken in the choice of the building blocks. Their degradation products have to be biocompatible, non-toxic and metabolized or eliminated by the living organism.Another aim of this work is the developed of a new chemical route to obtain aqueous dispersive biodegradable polyurethane. This chemical procedure was well succeeded in producing PU dispersions with solid content about 20%. Films were obtained by casting the dispersions in molds and allowing them to dry at room temperature. Porous scaffold were produced by dilution and freeze drying of the dispersion obtained. The films had 250% of deformation and the foams presented interconnected macroporous. The study of degradations products showed a moderated toxic effect and more studies have to be done to evaluated the release of these products at concentrations closer to the in vivo *conditions.The ultimate goal was associated the newly developed components (BGNP and PU aqueous dispersions) to produce membranes and scaffolds, intending to associate biocompatibility, mechanical and physical properties in a material designed for tissue engineering applications. The composites were obtained by the dispersion of BGNP in a polivynyl alcohol solution and then, the mixture was added to PU dispersion, with BGNP composition of 0, 10 and 25%. The films had 350% of deformation and the foams presented mechanical properties adequaded for tissue engineering applications. The materials presented good cell viability and hydroxyapatite layer formation.*

1 Introdução

Vidros bioativos (*bioactive glasses* - BGs) possuem excelente aplicação em engenharia de tecidos, especialmente em engenharia de tecido ósseo. Quando implantados no corpo, os BGs induzem uma resposta biológica específica na interface do material, o que resulta na formação de uma forte ligação entre o tecido e material [1]. Esses vidros formam uma camada de hidroxiapatita carbonatada (*hydroxyl carbonate apative* - *HCA*) em sua superfície e, através dessa camada, se ligam ao tecido ósseo vivo quando são implantados em defeitos ósseos [2]. A formação dessa camada de HA é requerimento essencial para materiais artificiais exibirem bioatividade [2].

Uma elevada área superficial, rica em sílica, é determinante para a formação da camada de HAC, levando os pesquisadores a utilizarem o processo sol-gel para criar BGs com áreas superficiais muito mais elevadas que os vidros produzidos pelo processo de fusão dos componentes. A composição e estrutura dos BGs produzidos pelo método sol-gel tem um efeito significativo em sua morfologia e taxa precipitação de microcristais HAC formados sobre sua superfície. Os componentes básicos da maioria dos vidros bioativos são SiO_2, Na_2O, CaO e P_2O_5 [1].

Vidros tri-componente 60% SiO_2-36% CaO-4% P_2O_5 foram estudados na forma densa e em pó e apresentaram altos níveis de bioatividade com excelente potencial para aplicação em engenharia de tecido [3]. Porém, o desenvolvimento de tecidos em matrizes depende de arranjos tridimensionais das células, requerendo, portanto, a síntese de materiais com estruturas apropriadas, consistindo uma arquitetura que define as formas para o tecido em crescimento e guia a sua formação. Assim, além de bioatividade e biocompatibilidade, essas matrizes devem apresentar: (i) estrutura tridimensional com alta porosidade de macroporos (diâmetros da ordem de 100 µm) interconectados para que haja migração celular e nutrição em todo o material, (ii) propriedades mecânicas adequadas às condições fisiológicas e ao tecido substituído, assim como os tecidos vizinhos e (iii) boa distribuição espacial e uniformidade de estrutura para promover ancoramento homogêneo de células [4].

Assim, com o avanço nas pesquisas sobre BGs e com objetivo de se adequar cada vez mais suas propriedades a os inúmeros requisitos que devem ser satisfeitos para que os materiais sejam aplicados como matrizes em engenharia de tecidos, vários trabalhos sobre vidros bioativos derivados do método sol-gel foram publicados incluindo vidros densos e partículas [3, 5-8], materiais porosos e matrizes tridimensionais (*scaffolds*) [9-16].

S*caffold*s podem ser obtidos adicionando-se um agente espumante na etapa de gelificação do processo sol-gel e promovendo-se agitação vigorosa, obtendo-se um volume de espuma que dependerá da concentração do surfactante, do tempo de agitação e da viscosidade da solução. O volume de espuma está diretamente relacionado à porosidade e ao tamanho de poros [14, 15]. Essas estruturas possuem porosidade e interconectividade de poros adequadas para aplicação em engenharia de tecidos (Fig. 1.1),

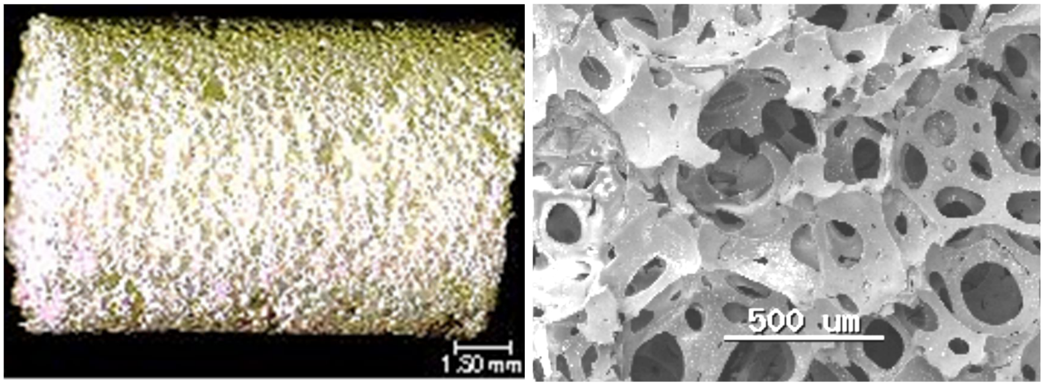

(a) (b)

Figure 1.1: Espumas de vidro bioativo com composição, em massa, de 60% SiO_2, 36% CaO e 4% P_2O_5. Imagens . (a) óptica. (b) obtida por microscopia electronica de varredura (MEV).

No entanto, em comparação com tecidos ósseos naturais, os vidros bioativos, especialmente quando processados na forma de espumas, apresentam propriedades mecânicas inferiores. Em particular, os baixos valores de tenacidade limitam o seu uso em situações onde haja aplicação de cargas [16]. Valores gerais das propriedades mecânicas de materiais de vidro bioativo foram resumidos por Rezwan et al. [17].

Uma abordagem para melhorar as propriedades mecânicas dos vidros bioativos é a produção de híbridos orgânico/inorgânico, na qual uma fase inorgânica, com dimensões manométricas, é inserida na matriz polimérica. O processo sol-gel apresenta-se potencialmente útil em possibilitar a combinação de polímeros com materiais cerâmicos em escalas moleculares e nanométricas. Isso por que permite a preparação de materiais cerâmicos em temperaturas compatíveis com o processamento de polímeros. Compósitos de vidro bioativo/biopolímeros têm sido desenvolvidos com base nessa estratégia [18-28].

A fase polimérica desempenha papel fundamental nas propriedades finais do compósito. Vários polímeros biodegradáveis, naturais ou sintéticos têm sido estudados como suporte para cultura de células. O hidrogel de álcool polivinílico (*Polyvinyl Alcohol* - PVA) possui excelente transparência, consistência macia quando na forma de membrana, além de apresentar excelente resistência química e também ser biocompatível e biodegradável [29, 30]. Um estudo promovido pelo *European Food Safety Authority* (http://www.efsa.europa.eu/) em 2005 indicou que o PVA com massa molar de até 30kg/mol não apresenta evidência de toxicidade em 90 dias e duas gerações de estudos com altos níveis de dosagem administradas (5,000mg/kg dia). O PVA não é mutagênico nem genotóxico nem apresentou atividade carcinogênica.

Espumas híbridas do sistema BG/PVA com composição nominal de PVA de 20 a 90% foram obtidas pelo método sol-gel [18-20]. A obtenção das espumas ocorreu pela hidrólise dos alcóxidos e subsequente adição de solução de PVA, surfactante e ácido fluorídrico (para catalisar a reação de gelificação) sob intensa agitação mecânica. O aumento da fração de PVA nos híbridos melhorou suas propriedades mecânicas, como resistência à compressão e tenacidade, porém houve redução do tamanho de poros e da porosidade total das espumas (Fig. 1.2).

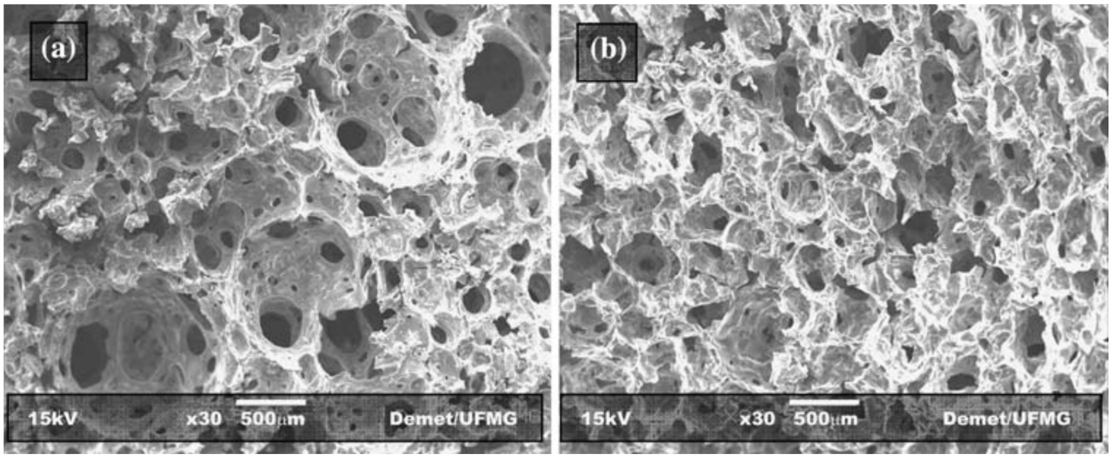

Figure 1.2: Imagens de MEV das espumas híbridas obtidas com frações de (a) 20 e (b) 60% de PVA.

Poliuretanas (PUs) são uma boa alternativa para substituir o PVA na produção de sistemas compósitos com vidro bioativo a fim de se obter materiais com propriedades mecânicas distintas das obtidas anteriormente, como espumas flexíveis. Tal abordagem pode ampliar a aplicação dos *scaffolds* produzidos como, por exemplo, suporte para o crescimento de células cardíacas e guias para crescimento de nervos e células epiteliais, uma vez que vários estudos comprovam que esse células proliferam e se desenvolvem bem em *scaffolds* flexíveis [22-33].

Além disso, uma nova estratégia que vem sendo desenvolvida por empresas e grupos de pesquisa da área de engenharia de tecidos é o entrelaçamento de três ou mais fios do biomaterial de maneira altamente complexa e precisa, para se criar estruturas planas, tridimensionais ou oca, com um alto grau de resistência mecânica. Fabricados a partir de um mesmo material ou uma combinação de diferentes fibras, essas tranças podem resultar em um material para degradação parcial ao longo do tempo ou manter uma geometria precisa para implantes. Esses tecidos biomédicos possuem resistência à fadiga e à abrasão, capacidade de compressão, e podem manter sua composição estrutural sem sacrificar a flexibilidade, resultando em uma adaptação mais facilitada dentro do corpo do que os materiais produzidos pelos métodos convencionais. As aplicações para esses trançados incluem: suturas, materiais para fixação de tecidos e implantes, tubos de reforço, scaffolds para engenharia de tecidos, entre outros (*Biomedical Structures* - http://www.bmsri.com/; *Medical Products and Technology* - http://www.qmed.com/mpmn).

Poliuretanas são uma classe de polímeros extremamente versátil que podem ser utilizadas em diversas aplicações devido à possibilidade de se alterar sua estrutura química a fim de se obter materiais com diferentes propriedades mecânicas, como alta flexibilidade, podendo ter aplicação como matrizes para cultura de células do tecido cartilaginoso ou como membranas flexíveis para diversos outros usos [31, 32].

A síntese de PU envolve a reação entre um poliisocianato com um poliol e um extensor de cadeia, formando copolímeros segmentados que consistem em segmentos rígidos e macios alternados, que originam micro separações de fases causadas pela incompatibilidade entre esses segmentos. O segmento macio é derivado do poliol e governa as propriedades a baixa temperatura. O segmento rígido é formado a partir do diisocianato e do extensor de cadeia e fornece resistência extra aos materiais, devido às ligações de hidrogênio envolvendo as ligações uretana. Propriedades físico-químicas podem ser modificadas, alterando a relação entre esses segmentos para atender a aplicação pretendida [31-33].

PUs biodegradáveis podem ser obtidas através da introdução de grupos susceptíveis à hidrólise, como dióis de poli(ε-caprolactona) (PCL), nos segmentos macios do esqueleto do polímero. Pode-se também aumentar sua taxa de degradação e/ou alterar sua resposta ao meio biológico pela inserção de diversos tipos de entidades inorgânicas tais como: partículas de vidro bioativo, fibras naturais, argila, nanotubos de carbono entre outros [33]. Além disso, a inserção de partículas bem dispersas e em tamanho diminuto pode atuar como reforço na estrutura do polímero, melhorando sua resitência mecânica [31].

Outro fator que deve ser levado em consideração no desenvolvimento de PU biodegradáveis, é que os produtos de degradação dos seus constituintes devem ser biocompatíveis, atóxicos e metabolizados ou eliminados pelo organismo vivo. Nesse quesito, a maior dificuldade reside na escolha do diisocianato, uma vez que os diisocianatos comumente usados na indústria são compostos aromáticos, que se degradam em diaminas tóxicas e cancerígenas. Diissocianatos alifáticos, como butano diisocianato (BDI), lisina diisocianato (LDI), hexametileno diisocianato (HDI) e isoforona diisocianato (IPDI), são preferencialmente utilizados na síntese de materiais biodegradáveis, mas poucos estudos foram realizados sobre os efeitos dos seus produtos de degradação quando implantados em organismos vivos [31-33].

Ayres [34, 35] desenvolveu com sucesso uma rota para a produção de dispersões aquosas de poliuretanas a partir de poliois PCL e diisocianato IPDI, utilizando trietilamina, como extensor de cadeia, e dibutil dilaurato de estanho, como catalisador, e obteve filmes com até 900% de deformação.

A idéia inicial desse trabalho era associar, pelo método sol-gel, a poliuretana desenvolvida por Ayres ao vidro bioativo com composição 60% SiO_2-36% CaO-4% P_2O_5, para produzir materiais compósitos flexíveis, bioativos e biodegradáveis. Porém, devido ao preço elevado e à dificuldade de importação do diisocianato IPDI, fez-se necessária a utilização de outro diisocianato na síntese. O primeiro candidato para a substituição do IPDI foi o LDI, por ser um diisocianato que se degrada em um aminoácido natural, componente de ossos, cartilagens e outros tecidos conectivos [33]. Porém, mais uma vez, a dificuldade de importação inviabilizou sua utilização. Assim, o HDI foi escolhido para substituir o IPDI na síntese de PU, por ser um diisocianato alifático e não apresentar dificuldades de importação. Assim, após inúmeras tentativas, os parâmetros de síntese foram ajustados (temperatura e tempo de reação) e eliminou-se a necessidade do uso de catalisador, uma vez que o HDI é mais reativo que o IPDI. Outra modificação feita na síntese foi a inserção de grupos silanos terminais nas cadeias da poliuretana para possibilitar a formação de ligações primárias entre o polímero e o vidro.

Resultados preliminares mostraram a incompatibilidade entre as dispersões de PU produzidas e a síntese do BG pelo método sol-gel. Ocorria a precipitação da poliuretana no momento em que essa entrava em contato com o sol produzido. Para possibilitar a obtenção dos compósitos, foi necessário desenvolver outro método de incorporação do vidro bioativo na fase polimérica.

Um método de obtenção de compósitos orgânico/inorgânicos amplamente utilizado é a incorporação de uma fase inorgânica nanométrica, na forma de partículas ou fibras, na matriz polimérica. Em comparação com partículas em microescala, partículas nanométricas apresentam área superfícial significativamente maior e podem formar uma interface mais coesa em compósitos de matriz polimérica e, portanto, possibilitam o desenvolvimento de materiais com altas performances em propriedades mecânicas [36]. Além disso, estudos demonstraram que materiais em nanoescala apresentaram uma maior biocompatibilidade [36-38]. Ostomel et al. revelou igualmente que a redução das partículas de vidro bioativos a tamanhos nanométricos poderia estimular sua bioatividade [38].

Estudos reportam a preparação de nanopartículas de vidro bioativo pelo método sol-gel em emulsões (co-precipitação), através do controle das concentrações dos alcóxidos, catalisadores e pH [39-43]. Ao controlar tais parâmetros, ao invés de se produzir géis silicatos poliméricos, como ocorre normalmente na produção de vidros densos e espumas, pode-se obter partículas com dimensões manométricas [39].

Géis silicatos poliméricos são produzidos por reações de hidrólise e condensação aquosa do precursor alcóxido. A reação de hidrólise substitui um grupo alcóxido (OR) por um grupo hidroxila (OH) (Eq. 1.1). Duas moléculas hidrolisadas parcialmente podem se ligar em uma reação de condensação envolvendo grupos silanol (*Si-OH*) para produzir ligações siloxanas (*Si-O-Si*) mais água ou álcool como subproduto (Eq. 1.2 e 1.3).

$$-[Si-OR+H_2O \rightarrow -[Si-OH+ROH \qquad \text{Eq. 1.1:}$$

$$-[Si-OR+HO-Si]- \rightarrow -[Si-O-Si]-+ROH \qquad \text{Eq. 1.2}$$

$$-[Si-OH+OH-Si]- \rightarrow -[Si-O-Si]-+H_2O \qquad \text{Eq. 1.3}$$

Tais reações podem continuar pelo processo de polimerização do alcóxido, resultando em um polímero ramificado. Por outro lado, sob certas condições, como baixa concentração de água, as reações de hidrólise incompletas podem capacitar a condensação, resultando em cadeia poliméricas com braços relativamente pequenos. Altas concentrações de água favorecem a hidrólise e inibem a condensação, uma vez que a água é um produto dessa reação.

A natureza do catalisador, ácido ou básico, influencia fortemente a cinética de reação, assim como a estrutura final do gel. Se a hidrólise for catalisada por base, a reação deve se processar através de uma substituição nucleofílica, e a velocidade de hidrólise será maior que a velocidade de condensação, levando à formação de cadeias mais ramificadas no início do processo. Se a hidrólise for catalisada por ácido, vai ocorrer uma reação eletrofílica, e a velocidade da condensação será maior que a da hidrólise, levando à formação de cadeias mais longas e menos ramificadas no início do processo.

O processo de polimerização pode ser divido em três domínios de pH’s: pH abaixo de 2, entre 2 e 7 e acima de 7. Esses domínios são estabelecidos de acordo com as características superficiais da sílica como o ponto de carga zero (PCZ), onde a carga superficial é zero, e o ponto isoelétrico (PIE), onde a mobilidade das partículas da sílica é zero, ambos na faixa de pH entre 1 e 3. O limite de pH igual a 7 aparece porque tanto a solubilidade como a taxa de dissolução são maximizadas e porque as partículas de sílica são ionizáveis apreciavelmente acima desse valor de pH, de forma que o crescimento das partículas ocorre sem agregação ou gelificação.

Abaixo do pH 2, a formação e a agregação de partículas primárias ocorrem simultaneamente, as partículas carregam pouca carga, o que permite a colisão entre elas, dando origem a cadeias e, posteriormente, a um sólido tridimensional (Fig. 1.3).

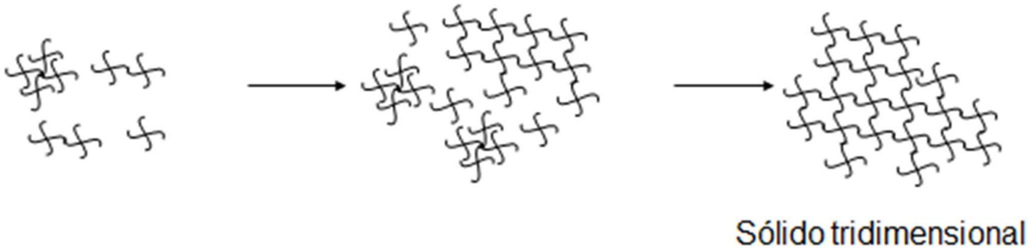

Figure 1.3: Representação esquemática da reação sol-gel em pH menor que 2.

Em pHs entre 2 e 7, a polimerização ocorre entre espécies condensadas, uma vez formados os dímeros, eles reagem preferencialmente com monômeros para formar trímeros e, que tornam a reagir para formar tetrâmeros. O crescimento e agregação ocorrem por contínua adição de moléculas pequenas às moléculas mais condensadas, formando cadeias e, por fim, uma rede tridimensional (Fig. 1.4).

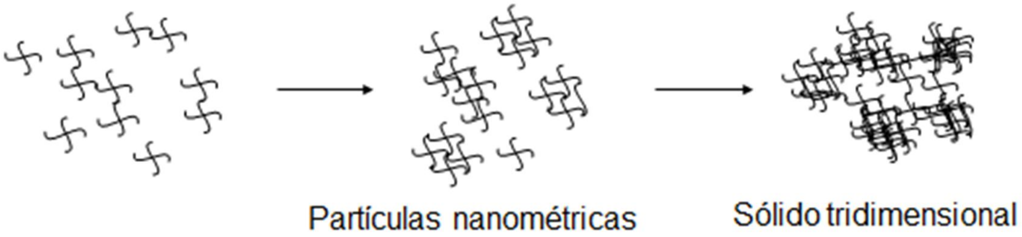

Figure 1.4: Representação esquemática da reação sol-gel em pH entre 2 e 7.

Acima do pH 7, as partículas são carregadas negativamente e repelem-se mutuamente. Assim sendo, elas não colidem, proporcionando um crescimento das partículas sem agregação. A taxa de crescimento dessas partículas está ligada às suas solubilidades, que dependem da sua distribuição de tamanho. Como partículas pequenas são mais solúveis do que as grandes, têm-se uma tendência geral de crescimento do tamanho médio das partículas e uma diminuição no seu número total (Fig. 1.5).

Figure 1.5: Representação esquemática da reação sol-gel em pH acima de 7.

Partículas de vidro bioativo produzidas pelo método sol-gel apresentam formas variadas e se mostraram termodinamicamente instáveis devido às altas energias interfaciais, resultantes das grandes áreas superficiais e geometrias irregulares obtidas [39-43]. Em geral, essas nanopartículas tendem a se aglomerar durante a fase de preparação e durante o processo de dispersão na fase polimérica, na tentativa de minimizar a energia livre do sistema. Se isso ocorre no compósito, pode causar uma redução no efeito de reforço das partículas, o que acabará por afetar as propriedades mecânicas do compósito [36].

Stober relatou um método pioneiro para a síntese de nanopartículas de sílica, esféricas e monodispersas, a partir do alcóxido teraetil ortosilicato (TEOS) na presença de amônia, com tamanhos variando de 10 nm a pouco mais de 1 μm e distribuição granulométrica estreita. Cinco parâmetros desempenham um papel importante no tamanho e na distribuição de tamanho de nanopartículas de sílica: (i) concentração do alcóxido, (ii) concentração de água, (iii) a concentração de catalisador, (iv) temperatura de reação e v) álcool utilizado [39].

Este trabalho tem como um dos objetivos utilizar, pela primeira vez, o método Stober para produzir nanopartículas de vidro bioativo (*Bioactive glass nanoparticles* – BGNP) no sistema tricomponente 60% SiO_2-36% CaO-4% P_2O_5 e obter partículas esféricas, monodispersas e bioativas. Outro objetivo é a produção de compósitos pela incorporação dessas nanopartículas na poliuretana biodegradável obtida, desenvolvendo, assim, sistemas compósitos, na forma de membranas e matrizes tridimensionais, com excelente potencial para aplicações biomédicas.

Os estudos introduzidos nesse capítulo foram realizados na elaboração da presente tese de doutorado. Os objetivos específicos e da tese em geral são apresentados no capítulo 2. O capítulo 3 apresenta as informações gerais sobre as técnicas de caracterização utilizadas no trabalho. Com exceção dos capítulos de introdução, objetivos e considerações finais, o conteúdo da tese foi escrito em inglês, no formato de artigos, e dividido em capítulos de acordo com objetivos específicos. Cada capítulo é independente e, por essa razão, muitas vezes fez-se necessária a repetição de algumas definições e metodologias já descritas em capítulos anteriores.

No capítulo 3, é apresentada a síntese e caracterização das nanopartículas de vidro bioativo produzidas, avaliando-se o tratamento térmico utilizado, diâmetro das partículas antes e após tratamento térmico, estrutura química, área superficial, porosidade total e dispersibilidade em diferentes meios e teste biológico.

O efeito do tamanho da partícula na bioatividade do BG foi avaliado no capítulo 4 por estudos *in vitro,* comparando-se nanopartículas com micropartículas obtidas com a mesma composição nominal de 60% SiO_2-36% CaO-4% P_2O_5.

O capítulo 5 é dedicado ao desenvolvimento de dispersões aquosas de poliuretanas biodegradáveis produzidas a partir de PCL e HDI e terminadas com grupos silanos, bem como à produção de membranas e espumas desse material e avaliação de suas propriedades mecânicas e do potencial tóxico dos seus produtos de degradação em contato com culturas de osteoblastos.

O capítulo 6 descreve o processo de obtenção de compósitos PU/BGNP, com frações de vidro de 10 e 25% em massa, na forma de filmes e espumas, e sua caracterização mecânica e biológica, além da avaliação *in vitro* da camada de HA produzida na superfície desses materiais.

Referências

1. Larry L. Hench. The story of bioglass. J Mater Sci: Mater Med (2006) 17:967–978
2. Tadashi Kokubo, Design of bioactive bone substitutes based on biomineralization process Materials Science and Engineering C 25 (2005) 97–104
3. Marivalda M Pereira, Arthur E Clark and Larry L Hench. Homogeneity of bioactive sol-gel derived glasses in the system SiO_2-CaO-P_2O_5. Journal of Material synthesis and processing 2 (1994) 3:189-195
4. Buckley, C.T.; O'Kelly, K.U.: Topics in Bio-Mechanical Engineering. Trinity Centre for Bioengineering & National Centre for Biomedical Engineering Science. Dublin, Ireland (2004) 147-166
5. Xiaofeng Chen, Yongchun Meng, Yuli Li, Naru Zha. Investigation on bio-mineralization of melt and sol–gel derived bioactive glasses. Applied Surface Science 255 (2008) 562–564
6. Delia S. Brauer, Natalia Karpukhina, Matthew D. O'Donnell, Robert V. Law, Robert G. Hill. Fluoride-containing bioactive glasses: Effect of glass design and structure on degradation, pH and apatite formation in simulated body fluid. Acta Biomaterialia 6 (2010) 3275–3282
7. Julian R. Jones, Olga Tsigkoua, Emily E. Coatesa, Molly M. Stevensa, Julia M. Polakb, Larry L. Hench. Extracellular matrix formation and mineralization on a phosphate-free porous bioactive glass scaffold using primary human osteoblast (HOB) cells Biomaterials 28 (2007) 1653–1663
8. Shuyi Li, Lynsa Nguyen, Hairong Xiong, Meiyao Wang, Tom C Hu, Jin-Xiong She, Steven M. Serkiz, George G. Wicks, William S. Dynan. Porous-wall hollow glass microspheres as novel potential nanocarriers for biomedical applications. Nanomedicine: Nanotechnology, Biology, and Medicine 6 (2010) 127–136
9. Julie Elizabeth Gougha, Julian R. Jones, Larry L. Hench. Nodule formation and mineralisation of human primary osteoblasts cultured on a porous bioactive glass scaffold Biomaterials 25 (2004) 2039–2046
10. Qiang Fu, Mohamed N. Rahaman, B. Sonny Bal, Roger F. Brown, Delbert E. Day. Mechanical and in vitro performance of 13–93 bioactive glass scaffolds prepared by a polymer foam replication technique Acta Biomaterialia 4 (2008) 1854–1864
11. Yufang Zhu, Chengtie Wu, Yogambha Ramaswamy, Emanuel Kockrick, Paul Simon, Stefan Kaskel, Hala Zreiqat. Preparation, characterization and in vitro bioactivity of mesoporous bioactive glasses (MBGs) scaffolds for bone tissue engineering. Microporous and Mesoporous Materials 112 (2008) 494–503
12. Devis Bellucci, Valeria Cannillo, Antonella Sola. Shell Scaffolds: A new approach towards high strength bioceramic scaffolds for bone regeneration. Materials Letters 64 (2010) 203–206

13. Juan Peña, Jesús Román, M. Victoria Cabañas, María Vallet-Regí, An alternative technique to shape scaffolds with hierarchical porosity at physiological temperature. Acta Biomaterialia 6 (2010) 1288–1296
14. Marivalda M Pereira and Larry L Hench. Mechanisms of hydroxyapatite formation on porous gel-silica substrates. Journal of Sol-Gel Science and Technology 7 (1996) 59-68
15. Marlene B Coelho and Marivalda M Pereira. Sol-gel synthesis of bioactive glass scaffolds for tissue engineering: effect of surfactant type and concentration. Journal of Biomedical Materials Research Part B: Applied Biomaterials (2005) 75B (2) 451-456
16. Jeffrey O. Hollinger Thomas A. Einhorn, Bruce A. Doll and Charles Sfeir. Bone tissue engineering. CRC Press (2000) ISBN: 0-8493-1621-9
17. K. Rezwan, Q.Z. Chena, J.J. Blakera, Aldo Roberto Boccaccinia. Biodegradable and bioactive porous polymer/inorganic composite scaffolds for bone tissue engineering. Biomaterials 27 (2006) 3413–3431
18. Marivalda M Pereira, Julian R Jones and Larry L Hench Bioactive glass and hybrid scaffolds prepared by sol-gel method for bone tissue engineering. Adv in Applied Ceram 104 (2005) 35:42
19. Oliveira AAR, Ciminelli V, Dantas MSS, Mansur HS, Pereira MM Acid Character Control of Bioactive Glass/Polyvinyl Alcohol Hybrid Foams Produced by Sol-Gel J Sol-Gel Sci Technol (2008) DOI 10.1007/s10971-008-1777-1
20. Herman S. Mansur, Hermes S. Costa. Nanostructured poly(vinyl alcohol)/bioactive glass and poly(vinyl alcohol)/chitosan/bioactive glass hybrid scaffolds for biomedical applications. Chemical Engineering Journal 137 (2008) 72–83
21. R. Ravarian, F. Moztarzadeh, M. Solati Hashjin, S.M. Rabiee, P. Khoshakhlagh, M. Tahriri Synthesis, characterization and bioactivity investigation of bioglass/hydroxyapatite composites Ceramics International 36 (2010) 291–297
22. K. Rezwan, Q.Z. Chena, J.J. Blakera, Aldo Roberto Boccaccinia. Biodegradable and bioactive porous polymer/inorganic composite scaffolds for bone tissue engineering. Biomaterials 27 (2006) 3413–3431
23. Tiiu Niemela, Henna Niiranen, Minna Kellomaki. Self-reinforced composites of bioabsorbable polymer and bioactive glass with different bioactive glass contents. Part II: In vitro degradation. Acta Biomaterialia 4 (2008) 156–164
24. V. Cannillo, F. Chiellini, P. Fabbri, A. Sola. Production of Bioglass 45S5 – Polycaprolactone composite scaffolds via salt-leaching. Composite Structures 92 (2010) 1823–1832
25. Chengtie Wu, Yufeng Zhang, Yufang Zhu, Thor Friis, Yin Xiao. Structure–property relationships of silk-modified mesoporous bioglass scaffolds. Biomaterials 31 (2010) 3429–3438
26. Abeer M. El-Kady, Ebtsam A. Saad, Bothaina M. Abd El-Hady, Mohmmad M. Farag aSynthesis of silicate glass/poly(L-lactide) composite scaffolds by freeze-extraction technique: Characterization and in vitro bioactivity evaluation Ceramics International 36 (2010) 995–1009
27. Superb K. Misra, F. Ohashi, Sabeel P. Valappil, Jonathan C. Knowles, I. Roy f, S. Ravi P. Silva, Vehid Salih, Aldo R. Boccaccini. Characterization of carbon nanotube (MWCNT) containing

P(3HB)/bioactive glass composites for tissue engineering applications Acta Biomaterialia 6 (2010) 735–742

28. Mathew Petera, N.S. Binulala, S.V. Naira, N. Selvamurugana,b, H. Tamurac, R. Jayakumara, Novel biodegradable chitosan–gelatin/nano-bioactive glass ceramic composite scaffolds for alveolar bone tissue engineering Chemical Engineering Journal 158 (2010) 353–361
29. Chiellini, E., Corti, A., D'Antone, S., Solaro, R. Biodegradation of poly(vinyl alcohol) based materials. Progress in Polymer Science 28 (2003) 963-1014
30. Lin, W.C. e. al. Blood compatibility of novel poly(γ-glutamic acid)/poly(vinyl alcohol hydrogels. Colloids and Surfaces B: Biointerfaces 47 (2006) 43-49
31. Patrick Vermette, Hans J. Griesser, Gaétan Laroche and Robert Guidoin. The tissue engineering intelligence unit 6: biomedical applications of polyurethanes. Landes Bioscience (2001) ISBN: 1-58706-023-X.
32. Tim Thomson. Polyurethanes as specialty chemicals: principles and applications. CRC Press (2005) ISBN: 0-8493-1857-2.
33. J Santerrea, K Woodhouse, G Laroche, RS Labow. Understanding the biodegradation of polyurethanes: From classical implants to tissue engineering materials. Biomaterials 26 (2005) 7457–7470.
34. Eliane Ayres, Rodrigo L. Oréfice, M. Irene Yoshida. Phase morphology of hydrolysable polyurethanes derived from aqueous dispersions. European Polymer Journal 43 (2007) 3510–3521.
35. Gisele Rodrigues da Silva, Armando da Silva-Cunha Jr., Francine Behar-Cohen, Eliane Ayres, Rodrigo L. Oréfice. Biodegradation of polyurethanes and nanocomposites to non-cytotoxic degradation products. Polymer Degradation and Stability 95 (2010) 491-499.
36. K.A. Padmanabhan. Mechanical properties of nanostructured materials. Materials Science and Engineering A304–306 (2001) 200–205
37. T.J. Webster, R.W. Siegel, R. Bizios. Osteoblast Adhesion on Nanophase Ceramics. Biomaterials 20 (1999) 1221.
38. T.J. Webster, C. Ergun, R.H. Doremus, R.W. Siegel, R. Bizios. Nanoceramic surface roughness enhances osteoblast and osteoclast functions for improved orthopaedic/dental implant efficacy j. Biomed. Mater. Res. 51 (2000) 475.1261.
39. C. Jeffrey Brinker and George W. Scherer. The sol-el science the physics and chemistry of sol-gel processing. Academic Press, Inc. (1990) ISBN 0-12-134970-5.
40. Mathew Petera, N.S. Binulala, S.V. Naira, N. Selvamurugana,b, H. Tamurac, R. Jayakumara, Novel biodegradable chitosan–gelatin/nano-bioactive glass ceramic composite scaffolds for alveolar bone tissue engineering Chemical Engineering Journal 158 (2010) 353–361
41. Aixue Liu, Zhongkui Hong, Xiuli Zhuang, Xuesi Chen, Yang Cui, Yi Liu, Xiabin Jing. Surface modification of bioactive glass nanoparticles and the mechanical and biological properties of poly(L-lactide) composites Acta Biomaterialia 4 (2008) 1005–1015

42. Daniela S. Couto, Zhongkui Hong, João F. Mano. Development of bioactive and biodegradable chitosan-based injectable systems containing bioactive glass nanoparticles. Acta Biomaterialia 5 (2009) 115–123
43. Wadcharawadee Noohom, Kevin S Jack, Darren Martin and Matt Trau. Understanding the roles of nanoparticle dispersion and polymer crystallinity in controlling the mechanical properties of HA/PHBV nanocomposites Biomed. Mater. 4 (2009) 015003 13pp

2 Objetivos

2.1 Objetivos gerais:

Desenvolvimento e caracterizações físicas, químicas, mecânicas e biológicas de materiais bioativos, produzidos na forma de partículas, membranas e matrizes porosas, a partir de nanopartículas de vidro bioativo, poliuretanas biodegradáveis e compósitos formados pela associação desses materiais.

2.2 Objetivos específicos por capítulo:

Capítulo 3:

- Desenvolvimento de uma metodologia para obtenção de nanopartículas esféricas de vidro bioativo com composição nominal de 60% SiO_2-30% CaO-4% P_2O_5.
- Caracterização das nanopartículas produzidas quanto ao seu diâmetro, porosidade, área superficial específica, composição química e sua estabilidade quando dispersas diferentes meios.
- Caracterização das micropartículas de vidro bioativo com mesma composição com a finalidade de comparar as propriedades obtidas.
- Estudo de viabilidade celular das nanopartículas em comparação com as micropartículas

Capítulo 4:

- Avaliação da bioatividade das nanopartículas obtidas, em comparação com as micropartículas de mesma composição nominal, pela análise variação de potencial zeta em função de diferentes períodos de imersão das partículas em SBF.

- Avaliação da bioatividade pela caracterização da camada de HA formada na superfície das partículas obtidas.
- Estudos de viabilidade celular e atividade de fosfatase alcalina das partículas incubadas em diferentes períodos de tempo.

Capítulo 5:

- Desenvolvimento de dispersões aquosas de poliuretanas biodegradáveis produzidas a partir de PCL e HDI e terminadas com grupos silanos
- Produção e caracterização das membranas e espumas a partir das dispersões poliméricas obtidas.
- Avaliação da porosidade das espumas obtidas em relação à concentração de sólidos da dispersão.
- Estudo das propriedades mecânicas dos materiais obtidos.
- Análise do potencial tóxico dos seus produtos de degradação em ensaios de viabilidade celular.

Capítulo 6:

- Produção e caracterização das membranas e espumas compósitas a partir da associação da poliuretana com as nanopartículas produzidas, com composição, em massa, de 10 e 25% de BGNP.
- Avaliação da porosidade das espumas obtidas em relação à concentração nanopartículas.
- Estudo das propriedades mecânicas dos materiais obtidos.
- Análise do potencial tóxico dos seus produtos de degradação em ensaios de viabilidade celular.
- Avaliação da bioatividade pela caracterização da camada de HA formada na superfície dos compósitos obtidos.

3 Synthesis and characterization of 60%SiO_2-36%CaO-4%P_2O_5 bioactive glass nanoparticles by modified Stöber method

Abstract. *Since developed by Hench as a promising bone repairing material with high bioactivity and biocompatibility, bioactive glass has attracted extensive studies. Various investigations were directed to obtain sol–gel derived bioactive glasses as bulk, powder or porous scaffolds. Nanotechnology gives a new strategy to develop bioactive glasses, since nanoscaled biomaterials exhibit an enhanced biocompatibility and bioactivity. Stober developed a method for the synthesis of spherical and monodisperse silica nanoparticles from aqueous alcohol solutions of silicon alkoxides in the presence of ammonia as a catalyst. In this work a modified Stober Method was used in order to synthesize bioactive glass nanoparticles (BGNP) with dispersion capability and bioactivity. The BGNP obtained have spherical shape and average size of 20 nm, as prepared, and 90 nm, after heat treatment. Nanoparticles presented significant increase in cell viability when compared to microparticles. They present good dispensability on polar solvents and may offer superior performance for developing tissue scaffolds.*

3.1 Introduction

Since developed by Hench, as a promising bone repairing material with high bioactivity and biocompatibility, bioactive glass (BG) has attracted extensive investigations [1-34]. These materials have the capacity to form a layer of hydroxyapatite (HA) and bond to the living bone through this layer. The rate of tissue bonding to BGs depends on the rate of HA formation, which depends on the glass composition [1, 2]. The first BGs contained Na_2O, CaO, P_2O_5 and SiO_2 with varing compositions [1]. The three-component 60% SiO_2, 36% CaO and 4% P_2O_5 (% wt) sol-gel glasses presented high level of bioactivity and develop a HA layer, which shows an excellent potential for bone tissue engineering applications [3].

In the last decade, several researches have been directed towards the development of bioactive glass materials. Investigations regarding sol–gel derived BG have been published including bulk and powder bioactive glasses [1-20] and porous bioactive glass scaffolds [21-34]. However, compared with natural bone tissue, bioactive glasses, especially processed as foams, exhibit lower mechanical properties. In particular, the low fracture toughness limits the application of bioactive glasses as scaffold structures in load-bearing situations. General values of mechanical properties for bulk bioactive glass materials were summarized by Rezwan et al. [35].

The development of polymer/bioactive glass has been recognized as a strategy to improve the mechanical behavior of bioactive glass-based materials [35]. Compared with microsized bioactive ceramic particles, nanosized particles have a large surface area and can form a tighter interface with polymer matrix in composites, and hence, a high performance in mechanical properties can be expected [36]. Furthermore, studies reported that nanoscaled biomaterials exhibited an enhanced biocompatibility [37, 38] and some also revealed that reducing BG particles’ size to nanoscale could stimulate their bioactivity [39, 40]. In this context, several studies have been reporting systems based on nanoestructured bioactive glass/ biopolymer composites [39-56]. Studies showed that increasing specific surface area and pore volume of bioactive glass may greatly accelerate the deposition process of hydroxyapatite (HA) [39, 40].

Recently, BG nanopowders were prepared by Brunner et al. using flame synthesis [57], but the flame synthesis needs high temperature environment. On the contrary, the sol–gel technology is a low temperature preparation method, and the glasses prepared by sol–gel method have porous structure with high specific surface area. However, the particle size of the traditional sol–gel-derived bioactive glasses was larger than 1 μm [58]. In addition, the time of the synthesis of bioactive glasses by traditional sol–gel process is quite long because of the long gelation and ageing time [59]. Studies report the preparation of bioactive glass nanoparticles (BGNP) by controlling the concentration of the reagents, catalyst, alcohol medium and pH, mediated sol–gel process used in water/oil emulsions and coprecipitation method [58-66].

Nano-sized particles have a large surface area that results in a high interfacial energy, with the nanoparticles being thermodynamically unstable with respect to the suspension. In general, these particles will tend to agglomerate both during the preparation of the particles and during the mixing with the polymer phase in an attempt to minimize the free energy of the system. If this occurs in the composite, it can cause a reduction in the reinforcing effect of the particles which will ultimately affect the mechanical properties of the composite [55-58]. To maintain the stability of the particles, because of the spherical shape, various studies focused on the surface modification of Stober SiO_2 nanoparticles to create a bioactive material with dispersion capability [67-72].

Stöber et al. [73], in 1968, reported a pioneering method for the synthesis of spherical and monodisperse silica nanoparticles from aqueous alcohol solutions of silicon alkoxides in the presence of ammonia as a catalyst, and different sizes of silica particles were obtained. Silicic acid is produced during hydrolysis and when its concentration is above its solubility limit in the alcohol, it nucleates homogeneously and forms silica particles of submicron size. Particles obtained can be from 10 nm to more than 1 μm of diameter with a narrow size distribution. However, it was difficult to prepare monodispersed silica nanospheres with diameter smaller than 100 nm. Below this size, the spheres obtained are generally non-uniform in size, resulting in a multidispersed range of particles and, often, they are disform in spherical shape [73-86].

Some of the earliest research on Stöber particles is primarily concerned with empirically predicting the final particle size for a range of the initial reactant concentrations (0.1–0.5 M Tetraethyl Orthosilicate [TEOS]; 0.5–17.0 M [H_2O]; and 0.1–3.0 M ammonia [NH_3]) that produce monodisperse colloids [73-75]. Particle diameter can be controlled by finely tuning variable parameters such as, reagent concentration and reaction temperature. According to Bogush and Zukoski [75, 76], five parameters play an important role in the size and size distribution of silica nanoparticles: (i) concentration of TEOS, (ii) concentration of ammonia, (iii) concentration of water, (iv) effect of alcohol, and (v) reaction temperature. In addition, the effect of the molar ration R = H_2O/TEOS on particles size was studied [77-86].

Summarizing, these studies showed that low concentrations of TEOS provide monodisperse uniform-sized silica nanoparticles. The size of the silica nanoparticles was found to increase with TEOS and with increasing concentration of water and ammonia up to 7 and 2 M, respectively, after which the effect was reversed [73-86]. A decrease of particle size with increasing TEOS was also noticed at 4 M of ethanol and 14 M of ammonia [73, 75-79, 83-86]. An increase in particle size was observed with increasing ammonia concentration. R values ranging from 20 to 50 and [NH_3] ranging from 1 to 7 M results in monodispersed spherical particles [74, 78-83, 86]. The effect of R on particles size at different temperatures was also studied. The particle size increased with increasing temperature at higher R values, whereas at lower values the particle size decreases with increasing temperature. The temperature effect was related to the saturation concentration of ammonia, which decreased with increasing temperature [73, 75-81]. A distorted spherical shape of silica nanoparticles were observed at 70 ºC [86]. Particles prepared in methanol solutions are the smallest, while the particle size increases with increasing chain length of the alcohol. The particle size distribution also becomes broader when longer-chain alcohols are used as solvents. Particles prepared in methanol and ethanol-glycerol solutions resulted in a stable sol, but when butanol and ethanol were used, precipitation could be easily observed [74, 82-91].

Stöber method can be modified to produce particles with compositions different than pure silica. However, it is difficult to control the uniformity in size because of the potential for secondary nucleation resulting from multiple subsequent additions of alkoxide. Also, it takes a long time to obtain large particles, as limited amount of alkoxide (below a critical value) has to be added in any step to minimize the production of new particles [74, 87-91]. When changing the alkoxide differences in the nuclei occurred, attributed to differences in thermodynamic interactions between the solvent and the hydrolyzed intermediates. Once formed, the solid particles may increase in size by molecular addition, where soluble species deposit on the solid surface, or by aggregation with other solid particles. In the aggregation model, particles are assumed to be colloidal unstable and to grow solely by aggregation. It was shown that the final size depends on the balance of nucleation and aggregation rates and those systems giving the largest particles are characterized, after a short transient, by a size distribution where aggregation is dominant [74, 90, 91]. Owing to different thermodynamic interactions, a different nuclei size can be expected in the hydrolysis and poly-condensation of different alkoxides. In the case of mixed alkoxides the nuclei size should depend on the ratio of alkoxides hydrolyzed [90].

In this work, the Stöber method was used for the first time in order to get BGNP in the system 60% SiO_2-36% CaO-4% P_2O_5 by mixing different alkoxides and solubilizing calcium salt during the synthesis process to create a unique bioactive nanoparticles with dispersion capability. The alkoxides TEOS and Triethyl Phosphate (TEP) hydrolyses occurred in methanol/water mix in the presence of ammonium hydroxide under mechanical stirring. The size, composition, shape and dispersion capability of the obtained particles were studied by several analysis techniques.

3.2 Materials and Methods

The reagents used in the BGNP synthesis were Tetraethyl Orthosilicate 98% (TEOS) and Triethyl Phosphate 99% (TEP) by *Sigma-Aldrich*, Methanol and Calcium Nitrate

($Ca(NO_3)_2.4H_2O$) by *Synth*, Nitric Acid (HNO_3) and 33% Ammonium Hydroxide solution (NH_4OH) by *Merck*.

Synthesis of Bioactive Glass Nanoparticles (BGNP). BGs, with the nominal compositon in weight % of 60% SiO_2, 36% CaO, and 4% P_2O_5, were extensively studied previously [3, 23, 24] and showed an excellent potential for bone tissue engineering applications by presenting high level of bioactivity and development of a HA layer. For these reasons, as a starting point, it was decided to maintain the molar ratio H_2O/TEOS=12 and to keep the composition wt % of the glass used in sol-gel bioactive glass previously studied. The molar ratio catalyst/TEOS was the same used before, but the catalyst HNO_3 was substituted by NH_3. Also, methanol, at molar ratio CH_3OH/TEOS=4, was added to prevent liquid-liquid phase separation during the initial stage of the hydrolysis reaction [74]. Methanol was chosen as the solvent because particle size increases with increasing chain length of the alcohol [82-87]. The sol was diluted and reacted following the synthesis procedure described.

The synthesis procedure was used schematized in Fig. 3.1 and was as follows: (1) 200 ml of methanol was mixed with 0.12 ml of ammonium hydroxide 33% and 5.40 ml of water and stirred for 5 min. (2) Then 5.57 ml TEOS and 0.56 ml TEP were added dropwise for 10 min. The sol was mechanically stirred for 48 h. (3) The formed sol was placed in an oven at 50°C until the complete ammonium evaporation (about 3 h). (4) Then, the sol was filtered in a 0.22 μm *Milipore*. (5) 3.46 g $Ca(NO_3)_2.4H_2O$ was dissolved in the sol and mixed for 24 h. (6) The nanoparticles formed were separated by subsequent filtrations in 0.22 and 0.11 μm *Milipore*. (7) The sol filtered under 0.11 μm was submitted to freeze drying, to prevent the secondary aggregation of gel particles via the linkage of water molecules during the drying process [74]. (8) The powders obtained were thermally treated at two temperatures, 200ºC and 700 °C for 40 min, with heating rate of 1ºC/min. It is known that the thermal treatment just causes the particle agglomeration above temperatures of 900ºC or long time periods [81]. (9) At the end of the process well dispersed bioactive glass nanoparticles were obtained without grinding and sieving.

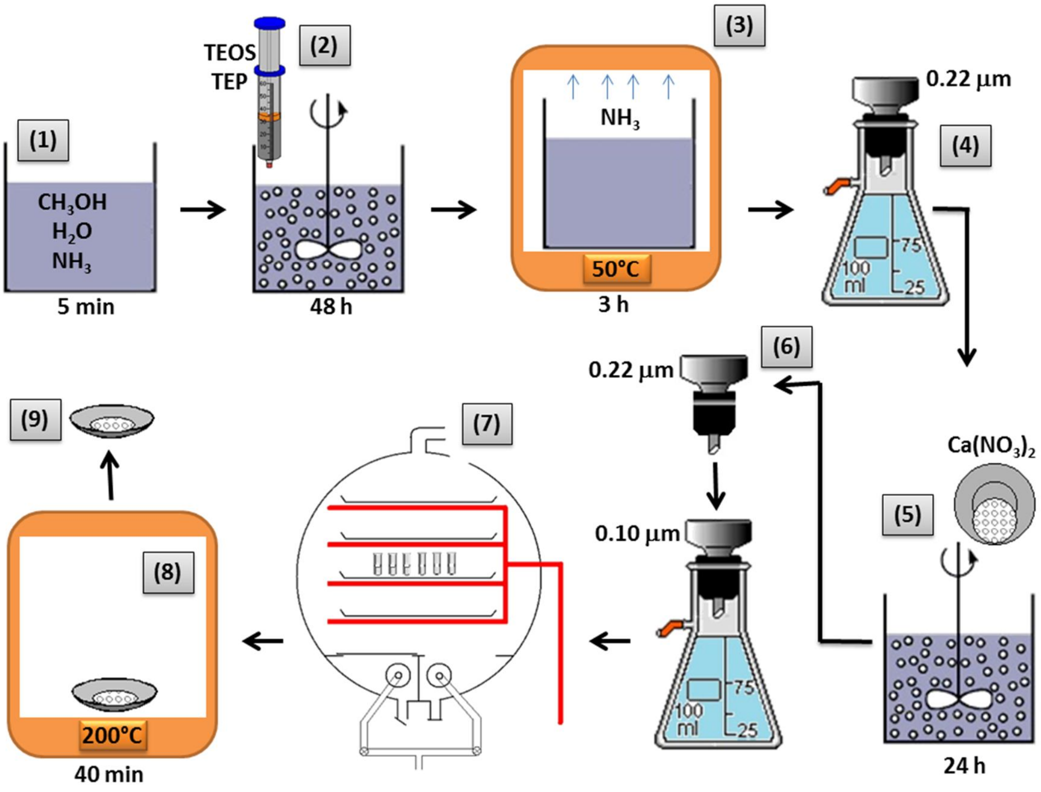

Figure 3.1: Schematic representation of BGNP synthesis.

The synthesis parameters described above, especially the methanol, ammonium hydroxide and water concentrations, were established after some initial evaluation of their effect on the nanoparticles characteristics was conducted. The synthesis parameters were varied as shown in Table 3.1.

Table 3.1: BGNP synthesis parameters.

Sample	***Compositions (M)***						***Reaction***
	TEOS	*TEP*	*NH_3*	*H_2O*	*CH_3OH*	*$Ca(NO_3)_2$*	***Time (h)***
Route 1	0.025	0.003	0.001	0.300	0.100	0.01	48
Route 2	0.025	0.003	0.040	0.030	4.938	0.01	48

Synthesis of Bioactive Glass Microparticles (BGMP). In order to compare the effect of particle size on the performance of bioactive glass, BGMP were prepared as described in previous papers [23, 24]. The synthesis was schematized in Fig. 3.2 and was as follows: (1) 131.8 ml of water was mixed with 22.0 ml of nitric acid 1M and stirred for 5 min. (2) Then 137.0 ml TEOS and 13.8 ml TEP were added and the sol was mechanically stirred for 2 hours. (3) 85.0 g $Ca(NO_3)_2.4H_2O$ was dissolved in the sol and mixed for 1 more hour. (4) The gel obtained was aged for 72 hours and (5) subsequently thermally treated at 700ºC for 360 min, with heating rate of 1ºC/min. (6) The solids were ground and separated by sieving in the range of 38-150 μm.

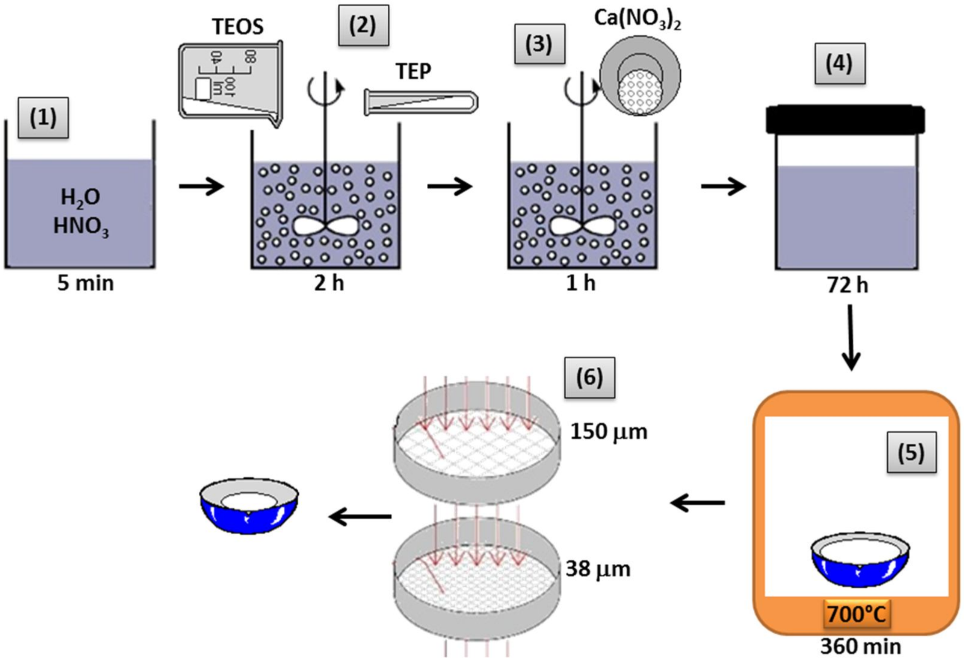

Figure 3.2: Schematic representation of BGMP synthesis.

Material characterization. The structure of the BGNP was analyzed by Fourier transform infrared (FTIR), Perkin Elmer 100 Spectrum. Spectra were collected in the mid-infrared range from 550 to 4000 cm^{-1} in μATR mode. Samples for FTIR analysis were diluted and ground in KBr with a sample to KBr dilution ratio of 1:100. X-ray Diffraction (XRD) spectra were collected on a Philips PW1700 series automated powder diffractometer using Cu Kα radiation at 40 KV/40 mA. Data was collected between 4.05 and 89.95º with a step of 0.06° and a dwell time of 1.5 second to identify any crystallization of the particles.

Morphologies and atomic composition of the BGNP were observed by Scanning Electron Microscope (SEM) Tecnai G220 FEI and transmission electron microscope (TEM) Quanta 200v FEG FEI, both equipped with energy-dispersive X-ray (EDS). The EDS spectra were all obtained at the same intensity of 12 kV. In order to quantify particle size, BGNPs were dispersed in water/ethanol and then collected on 400 mesh copper TEM grids and coated with lacey carbon film. The grids were pre-treated with ammonium hydroxide/water mixture, used to improve the deposition of NP in the grid surface. The diameter of individual particles was measured from TEM micrographs in ImageJ software. Two grids were prepared and analyzed in 8 different regions. Each region was divided in 9 different areas and, in each area it was measured the diameter of, at least, 3 particles, resulting in a minimum of 432 measurements. A shrinkage of 5% in diameter, that occurs when silica particles are subjected to intense radiation in the TEM analysis [74], were taken into account and all measurements of particle diameter were increased by 5%.

The particles surface area (*SA*) can be estimated using the value of average diameter obtained by TEM, assuming that the particles are solid, have spherical shape with smooth surface and same size. The surface area can be related to the average equivalent particle size by the equation 3.1:

$$SA = \frac{6000}{\rho_s \cdot D} \qquad \text{Eq.3.1}$$

Where ρ_s is the skeletal density (true density) in g/cm^3, which was determined from Quantachrome Helium Pycnometry.

The dynamic light scattering (DLS) analysis was used to measure the hydrodynamic diameter of the nanoparticles in a Zetasizer 3000 HS Data Type 1256. This system is equipped with a 4 mW helium/neon laser at 633 nm wavelength and measures the particle size with the noninvasive backscattering technology at a detection angle of 173°. Light scattering measurements were made at 25 ± 1°C. Hydrodynamic measurements were performed at 90° angle, after dilution of the sample to 10 µg/mL in saline solution, according to standards ISO 14488:2007 (*Particulate materials - Sampling and sample splitting for the determination of particulate properties*) and ISO13321 Part 8 1996 (*International Standard on Determination of Particle Size Distributions by Photon Correlation Spectroscopy*). The data were analyzed according to the cumulative method for apparent mean diameter and polydispersity index (PDI), the final value was a mean of 10 measurements. The samples were prepared in 10 mM NaCl, an indifferent electrolyte solution. In order to avoid the agglomeration of the particles and to evaluate the size of NP as prepared, the dispersion of BGNP produced was placed in an oven until the evaporation of methanol and, as the methanol evaporated, it was replaced by prepared saline solution to keep the initial volume. The heat treated particles were dispersed in saline solution for 10 minutes in an ultrasound bath, to evaluate the agglomeration of the water suspension. Zeta potential measurements were carried out to determine the stability of the BGNP dispersions in saline solutions of water and dimethyl sulfoxide (DMSO).

The N_2 adsorption–desorption isotherms were measured at 77 K on a Quantachrome 9. Specific surface area (*SA*) was determined with the Brunauer-Emmett-Teller (BET) method using adsorption data points in the relative pressure (P/Po) range of 0.01–0.30 [92]. The pore diameter distribution was calculated by the BJH method applied to the desorption curves. Desorption is preferred to adsorption for these calculations because it usually occurs at lower relative pressure, which is considered to be a better approximation of thermodynamic equilibrium [93]. The types of isotherms were evaluated according to their shape and type of hysteresis between adsorption-desorption modes [94].

In order to evaluated the differences of measurement obtained by different techniques, the relative deviation (Δ) between the different methods used was calculated. The results of the comparison between two techniques were considered good agreement for relative discrepancies until around 30% [95].

Biological response. For the biological tests, neonatal Male Wistars rats, obtained from *Centro de Bioterismo da Universidade Federal de Minas Gerais* (CEBIO) were used for all studies. The investigation conforms to the Guide for the Care and Use of Laboratory Animals published by the US National Institutes of Health (*NIH publication No. 85-23, revised 1996*). Osteoblasts were isolated from calvaria of 1-5 days old neonatal Wistar rats. Then the calvaria were dissected and cut into small fragments and rinsed in Dulbecco's phosphate buffered saline without calcium and magnesium. The fragments were sequential digested, first with 1% trypsin/EDTA for 5 minutes followed by four sequential digestions with 2% collagenase (180 unites/mL), *Sigma-Aldrich USA*, for 30 minutes each at 37°C. The first two digestions were discarded and the other three digestions produced a suspension of cells with osteoblasts. The three suspensions of cells were centrifuged for 5 minutes at 1000 G. The cells were cultured in DMEM with 10% fetal bovine serum (FBS), penicillin G sodium (10 unites/mL), streptomycin sulfate (10mg/ml) and 0.25 anfotericin-b, all *Gibco BRL USA*, in a humidified atmosphere of 5% CO_2 at 37°C. The cells were used for experiments on passage two.

The biological tests were performed according to ISO 10993 (*Part 5 - tests for in vitro cytotoxicity*). The cell viability was determined by MTT assay with 3-(4,5-dimethylthiazol-2-yl)-2,5-diphenyl-tetrazolium bromide, *Sigma-Aldrich*. It was used phosphate-buffered saline (PBS), as positive control and polyethylene, as negative control. Osteoblasts were plated in 96 well culture plates at density of 1×10^3 cells/cm^3 per well. Cells were normalized with DMEM without FBS. BG particles were sterilized under UV radiation and mixed in the medium, with weight-to-solution volume ratio of 0.1 mg/ml, and soaked for 5 min. The mixture was placed directly over the osteoblast culture on the plates and maintained at 37°C under 5% CO_2 atmosfere for 24 hours. After this period the medium was aspirated and 70 µl of new culture medium supplemented with 10% of FBS was added. 50 µl de MTT (5mg/ml) was added to each well. Four hours later, formazan salts were dissolved with isopropanol 10%/HCl. The absorbance was measured at spectrophotometer ADAP 1.6 (Netherlands) with 595nm filter. The experiments were performed with n=8 ($p<0.05$ statistical analysis: One way/ ANOVA/ Bonferroni/ GraphPad Prism. Background signal (wells with no cells) was deducted from the absorbance values. To compare the results obtained, the absorbance values were expressed as a function of the control (without materials). The absorbance value obtained with the control was considered as indicating 100% viability. The relative percentages of viability were expressed in terms of the control.

3.3 Results and Discussion

Synthesis parameter determinations. Fig. 3.3 (a) shows the particles obtained, using route 1, and Fig. 3.4 (a) shows the respective EDS. For this synthesis conditions, one of the two goals, which is to obtain spherical shape, was reached. However, the particle size (about 200 nm) was too large to consider these particles as nanoparticles.

With the objective of obtain particles of lower average diameter (about 20 nm), the catalyst concentration was adjusted by the corrected Bogush equation (Eq. 3.2) [91]. Bogush proposed an empiric equation predicting particle diameter, in nm, as a function of concentrations (mol.l^{-1}) at 25°C. Later, Razink corrected the equation by having a more reliable method to adjust reaction conditions. According to this equation, one can produce silica nanoparticles with nearly monodisperse size, ranging within 20% of the predicted target value, and for some initial conditions, considerably closer.

$$D = A \cdot \left[H_2O\right]^2 \cdot \exp\left(-B \cdot \sqrt{\left[H_2O\right]}\right) \qquad \text{Eq. 3.2}$$

Where A and B were defined as:

$$A = \sqrt{\left[TEOS\right]} \cdot \left(82 - 151 \cdot \left[NH_3\right] + 1200 \cdot \left[NH_3\right]^2 - 366 \cdot \left[NH_3\right]^3\right) \qquad \text{Eq. 3.3}$$

$$B = 1.05 + 0.523 \cdot \left[NH_3\right] - 0.128 \cdot \left[NH_3\right]^2 \qquad \text{Eq. 3.4}$$

Fig. 3.3 (b) shows the nanoparticles obtained, using route 2, and Fig. 3.4 (b) shows the corresponding EDS. The particles have diameter near the estimated value, 20 nm. The particles have diameter near the estimated value, 20 nm. An estimate by EDS analyses indicates that the particles obtained by the two different routes have similar oxide composition. Also, the EDS peak intensities shown for BGNP is similar to the obtained for BGMP [23, 24].

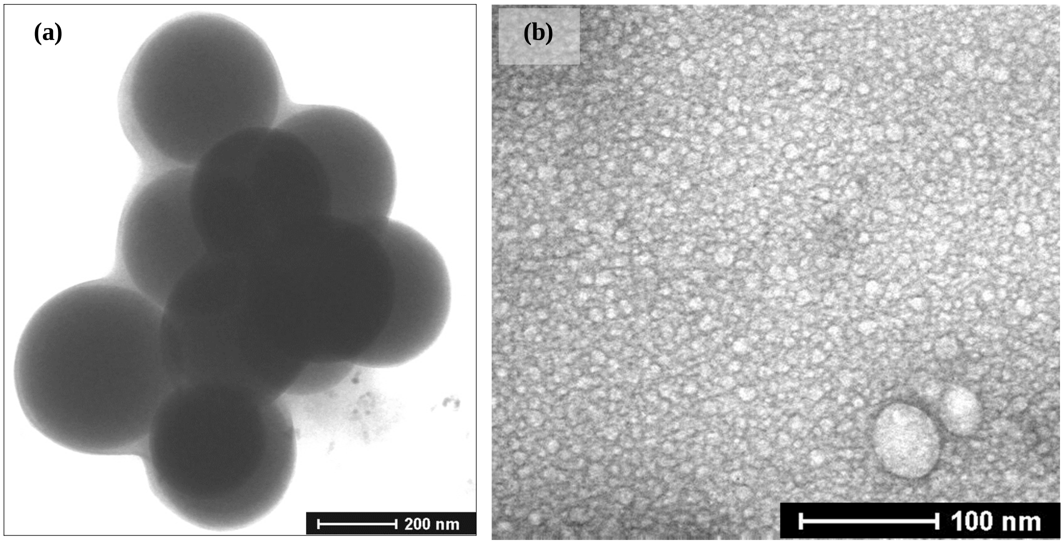

Figure 3.3: SEM images of transmitted electrons of BGNPs obtained from variations of synthesis parameters. (a) route 1 and (b) route 2, both as prepared on TEM grids.

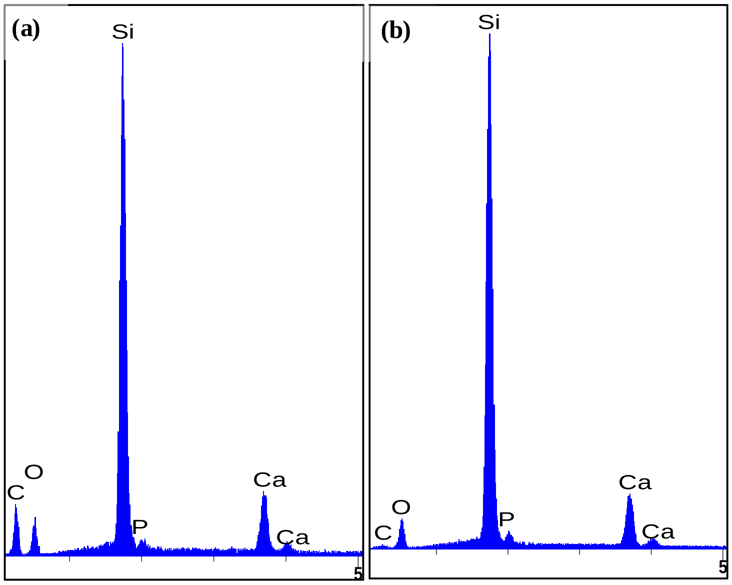

Figure 3.4: EDS, obtained at 12 kV, from respective SEM images of BGNs obtained from variations of synthesis parameters. (a) route 1 and (b) route 2.

Is noteworthy that the Bogush equation does not take into account the addition of another alkoxide (TEP), so, the TEP contribution was not considered. Then, there is an error associated with possible differences in diameter caused by the addition of TEP. The particle diameter should depend on the ratio of alkoxides hydrolyzed [90]. As the TEP nominal contribution is 4% of the particles total weight (molar ratio TEP/TEOS=0.12), it is reasonable to consider that this addition results in a small error. But it is important to emphasize that the TEP molar ratio is not the only parameter to be take into account, it is necessary also consider the differences in thermodynamic interactions between the solvent and the hydrolyzed intermediates when changing the alkoxide. When another alkoxide is added to the synthesis, the spheres obtained are generally non-uniform in size, resulting in a multidispersed range of particles and, often, non-spherical shape [73-76]. Despite all the considerations, the Bogush equation was adequate to predict the average size of nanoparticles as shown in Fig. 3.3 (b).

Structural characterization. The analysis of bioactive glass SiO_2-CaO-P_2O_5 by FTIR and XRD has been reported by several research groups in literature [96-102]. Fig. 3.5 shows the XRD patterns for untreated and heat treated at 700°C microparticles. It can be seen that the MP patterns are amorphous. No diffraction peaks were observed and the two broad bands of 2θ, between 15 and 40°, referred to amorphous silica, and 32 to 50°, referred to calcium silicate, were detected. Fig. 3.6 shows the BGNP XRD patterns. The untreated nanoparticles presented amorphous structure but, when the nanoparticles were treated at temperature of 700°C, crystalline peaks appeared in patterns at 2θ values of 29.3, 34.1 and 46.8, assigned to crystalline wollastonite ($CaSiO_3$) [101]. Wollastonite is formed due to the enhanced mobility of Si, Ca and P cations in the SiO_2-based glass structure during the heat treatment. The detailed mechanism of this crystallization is not well known, and is still under evaluation [102].

With the intent to prevent agglomerations and sintering during the heat treatment and to work with more amorphous sample to allow the comparison with MP, lower treatment temperatures were tested. NPs treated at temperature of 200°C at the short time interval of 40 minutes presented amorphous XRD pattern and was the choice as temperature of heat treatment for the nanoparticles produced.

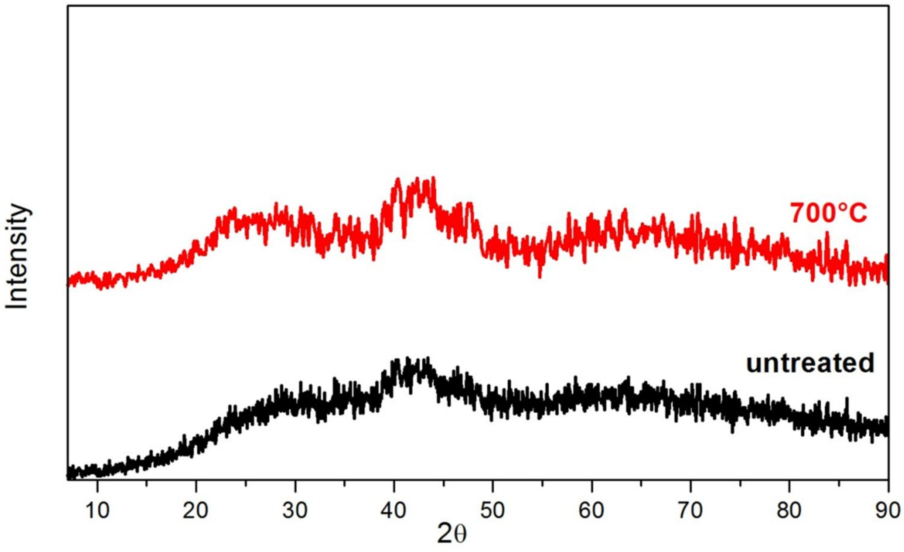

Figure 3.5: XRD patterns of BGMPs untreated and treated at 700°C.

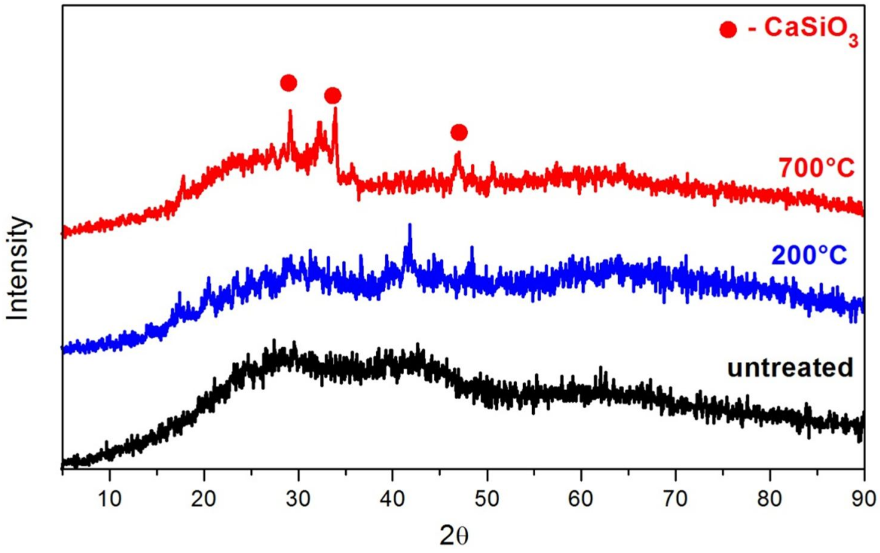

Figure 3.6: XRD patterns of BGNPs untreated and treated at 200 and 700°C.

Figure 3.7 shows the FTIR spectra of the BGNP treated at 200°C. The spectrum of the MP treated at 700°C is shown for comparison. The bands at 1200 and 1090 cm^{-1} are associated with transverse (TO) and longitudinal (LO) vibration modes, respectively, of asymmetric stretching in several cyclical species, species with 4 to 8 Si atoms and the network. The peak at 1160 cm^{-1} corresponds to P–O symmetric stretching.

From 1350 to 850 cm^{-1} there is a broad band that includes the asymmetric stretching of Si-O-Si at 1050-1070 cm^{-1}, the stretching of Si-O in the $SiO^- Ca^{2+}$ at 960-980 $cm^{-1}$and the bending of the OH bond and the SiO stretching in the Si-OH group at 880 cm^{-1}. It can be seen the dislocation of this broad band in BGNP spectrum, in comparison to BGMP, to lower wave numbers. This change can be attributed to the high density of Si-OH and $Si\text{-}O^-$ groups in the nanoparticles.

The band at 780-760 cm^{-1} is related to the Si-O-Si symmetric stretching and vibration modes of rings.

The divided bending vibration peak between 600 and 500 cm^{-1} is assigned to P-O asymmetric vibration of PO_4^{3-} groups [96-102] and appears only in the NP spectrum. This band is assigned to the crystalline calcium phosphate, which can be attributed to the formation of amorphous calcium phosphate in the NP during the heat treatment. The XRD pattern did not show this crystalline phase, probably because the formation of calcium phosphate occurred in low concentration in the material.

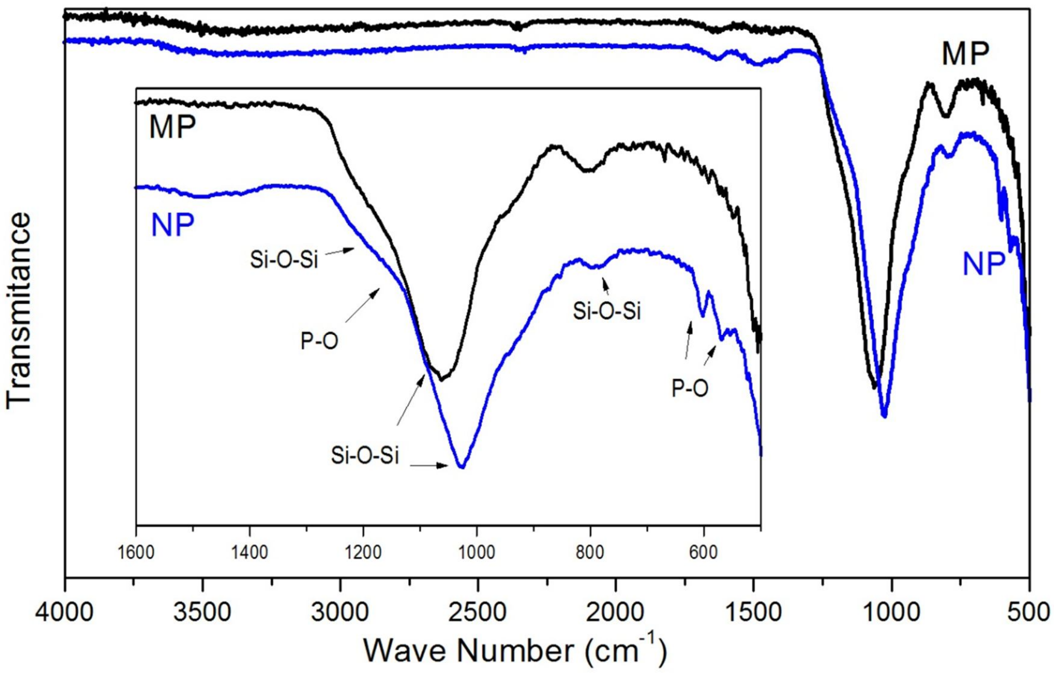

Figure 3.7: FTIR spectra of BG micro and nanoparticles obtained.

Size measurements by TEM. TEM images of BGNP produced are shown in Fig. 3.8. The images indicate that the particles are quite uniform spherical nanostructures, with multidisperse distribution.

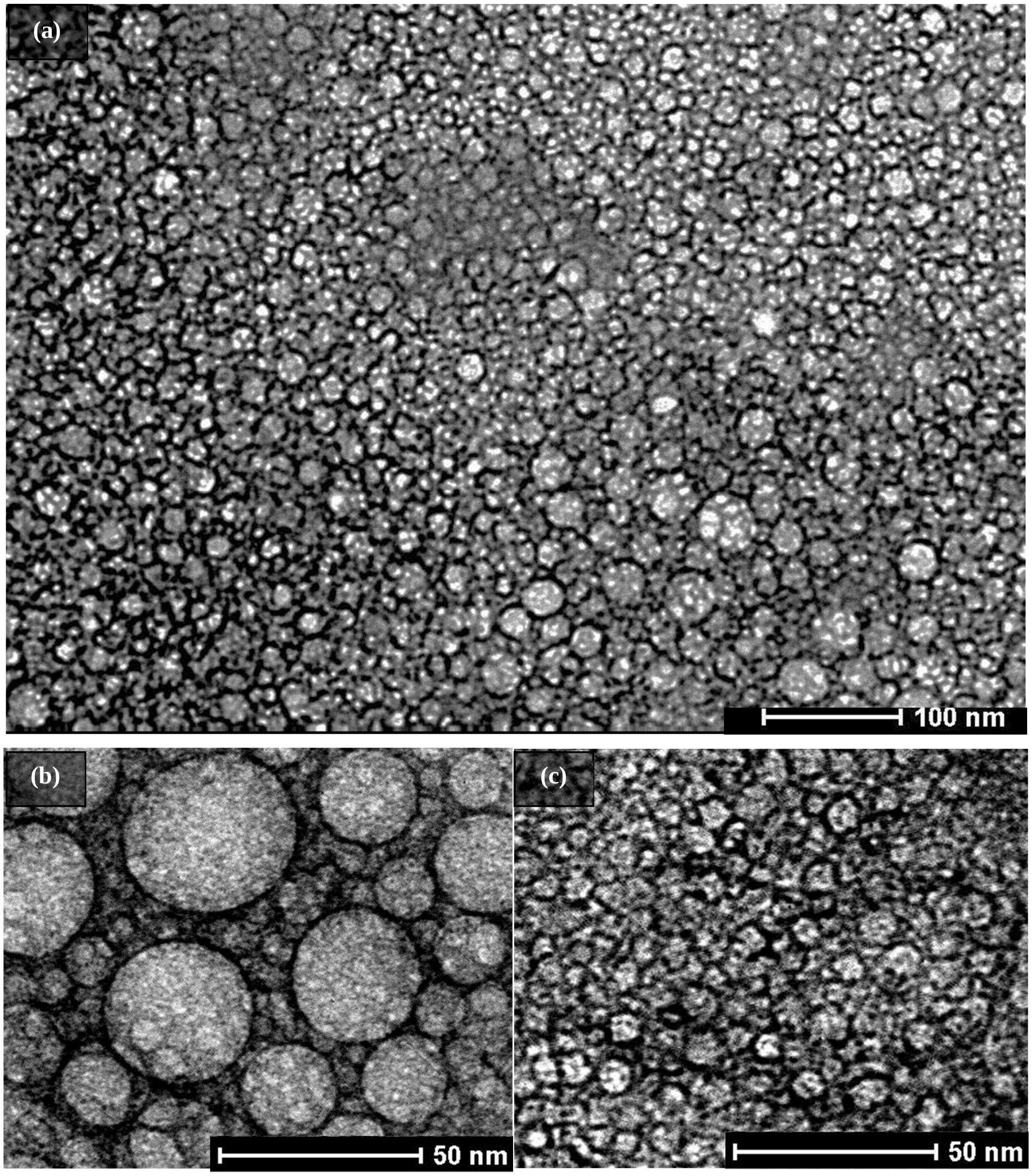

Figure 3.8: TEM images of BGNP as prepared. (a) Shows a general distribution of NP. Images (b) and (c) evidence differences in the particle sizes. The samples were prepared on TEM grids.

Tab. 3.2 presents the results of BGNP average diameter and diameter distribution obtained by TEM images. The average diameter calculated was (19 ± 9) nm, with minimum and maximum values of 4 and 70 nm respectively. The diameters were separated in rages of 10 nm and individual averages were calculated in each range. The distribution of average diameter in relationship with the % of total measurements is shown in Fig. 3.9. The major part of the particles (91%) presented diameter range between 7 and 27 nm. These results suggest that particle size obtained from TEM method agrees with the Bogush prediction (relative deviation Δ = 17%), but they also indicate that the particles are multidispersed. The geometrical surface area was calculated by Eq. 3.1 from the particle diameter measured by TEM and the obtained value is 148 m^2/g.

Table 3.2: Diameter distributions of BGNP obtained from TEM images.

Parameters	***Diameter Distributions (nm)***							
	0-10	*11-20*	*21-30*	*31-40*	*41-50*	*51-60*	*61-70*	*0-70*
n	130	204	100	31	8	1	3	477
% n	27.3	42.7	21.0	6.5	1.7	0.2	0.6	100
Average Diameter (nm)	9 ± 2	16 ± 3	25 ± 3	36 ± 2	45 ± 1	57	69 ± 1	19 ± 9

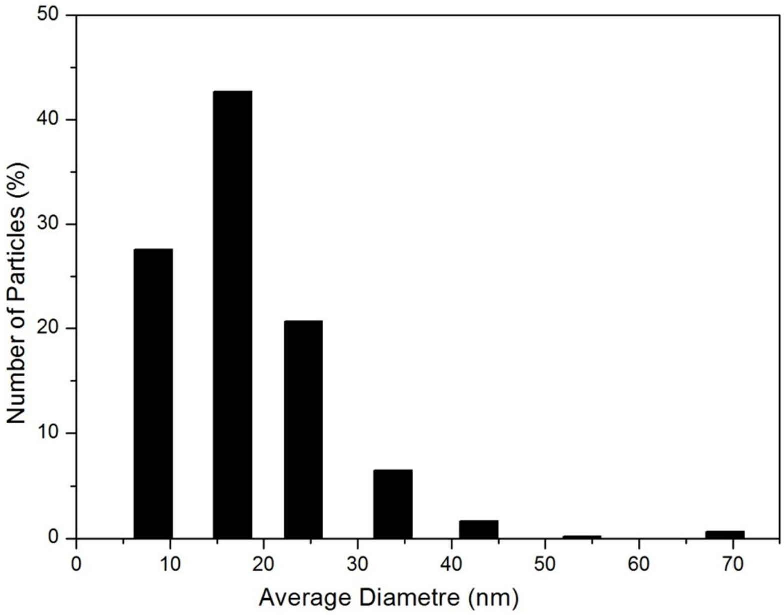

Figure 3.9: BGNP average diameter distribution obtained from TEM images.

Size measurements by DLS. The DLS measurements for nanoparticles as prepared and after heat treatment are showed in Fig. 3.10. Table 3.3 summarized the results obtained for average nanoparticles diameter obtained from different techiques. The cumulative analysis for the NP as prepared gives an average particle diameter of (22 ± 6) nm and a polydispersity index (PDI) of (0.23 ± 0.01), which is similar to TEM results (relative deviation Δ = 22%). For the heat treated and re-dispersed NP, the average particle diameter is (87 ± 4) nm with PDI of (0.10 ± 0.01), suggesting that these particles aggregated and/or were sintered, consequently, increasing in diameter, resulting in a narrower size distribution than the particles as prepared. This increase from about 22 to 87 nm, almost 300%, is probably because the large surface area of NP leads to a driving force great enough to produce aggregation and sintering at low temperatures [74, 82-87]. During drying and heat treatment, linkages between the materials and water molecules occurred resulting on secondary aggregation: small particles disappear and small pores are filled in, so the interfacial area decreases and the average pore size increases. This process does not produced shrinkage, because the centers of the particles do not move towards each other so, the particles can increase to micron size [74]. In order to minimize secondary aggregation, freeze drying was used to remove the water from material interface and the heat treatment occurred at low temperature and reduced time.

The Zeta Potential (ZP) measured for NP as prepared and re-dispersed shows they were highly negatively-charged, (-17 ± 4) and (-13 ± 2) mV, respectively, suggesting the particles are stable in both systems. The ZP of nanoparticles in dimethyl sulfoxide (DMSO) was (-47 ± 2) mV, showing that the BGNP has good dispersability in polar solvents.

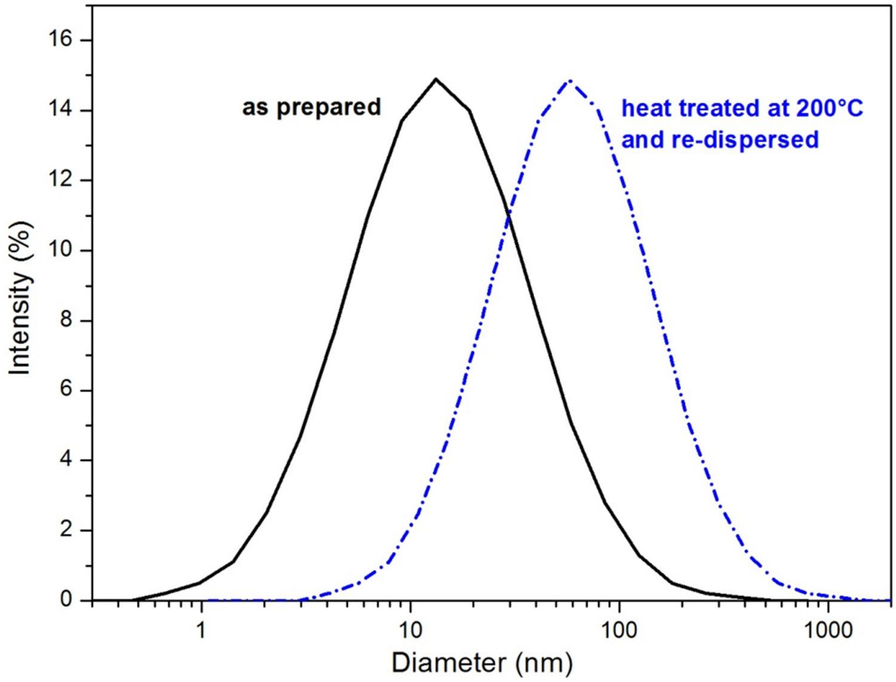

Figure 3.10: BGNP average diameter obtained from DLS. Each data point represents the mean of values calculated based on the average of nine histograms (n = 9).

Table 3.3: Average diameter of BGNP obtained from several techiques.

Samples	*Average Diameter (nm)*		
	Bogush	*TEM*	*DLS*
NP as prepared	20	19 ± 9	22 ± 6
NP after treatment	-	-	87 ± 4

BET analysis. Fig. 3.11 shows the N_2 adsorption/ desorption isotherms for BGNP. The BET BGMP analysis is also shown to compare how the nano scale affects pore structure and surface area of sol-gel BG. The isotherms can be identified as type II, which is characteristic of mesoporous materials. Mesoporosity (2-50 nm) is indicated by the presence of adsorption desorption hysteresis and by the slope of the adsorption step. The isotherms exhibited type H2 hysteresis loops, characterized by the narrow, steep and parallel adsorption and desorption branches. Type H2 hysteresis loops correspond to inkbottle-shaped pores. The cross-section of these pores is not necessarily uniform but the radius of the wider parts must be smaller than twice the radius of the narrow ends [90-92]. For MP adsorption isotherm, the hysteresis loop is smaller, thus indicating a decrease of the overall mesopore volume. On the contrary, the hysteresis loop of NP isotherm is much bigger, and this corresponded to a higher overall mesopore volume.

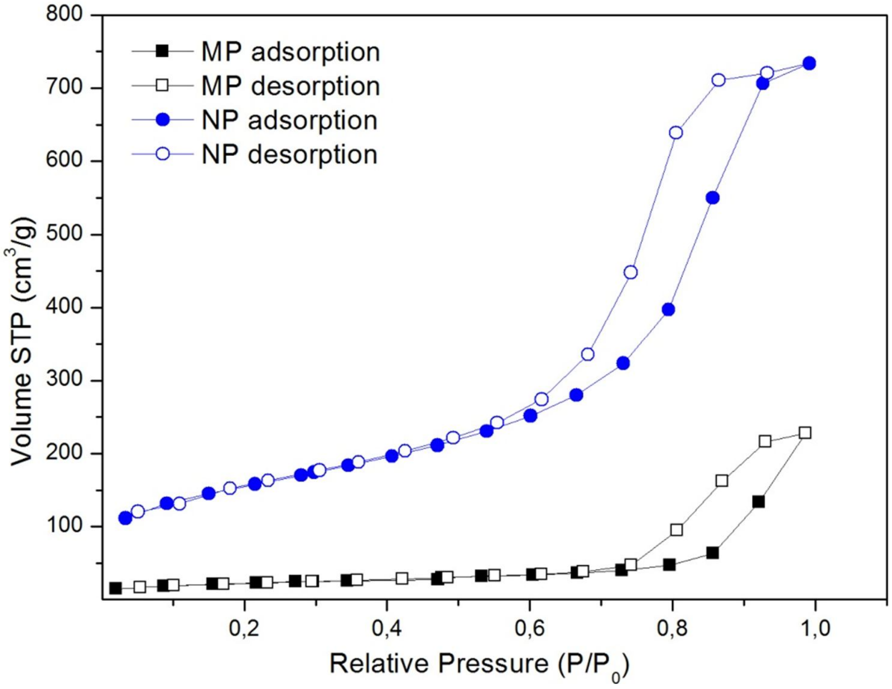

Figure 3.11: Nitrogen sorption isotherms of BG nano and micro sized.

Fig. 3.12 shows the pore-size distribution obtained from the desorption branch of the nitrogen sorption isotherms using BJH analysis. The vertical axis is a derivative of the volume of nitrogen adsorbed on the surface of the particles at each pore diameter. The pore volume of NP is significantly higher than MP, 1.11 and 0.38 cm^2/g, respectively. The micro and nano particle pore diameters are in the range of mesoporous materials (2-50 nm). The modal pore diameter (d_{mode}) was 9.6 nm for the MP and 9.7 for the NP, which was not a significant difference, because a variation of 0.1 nm was within the accuracy limits of the nitrogen sorption analysis technique (± 0.5 nm).

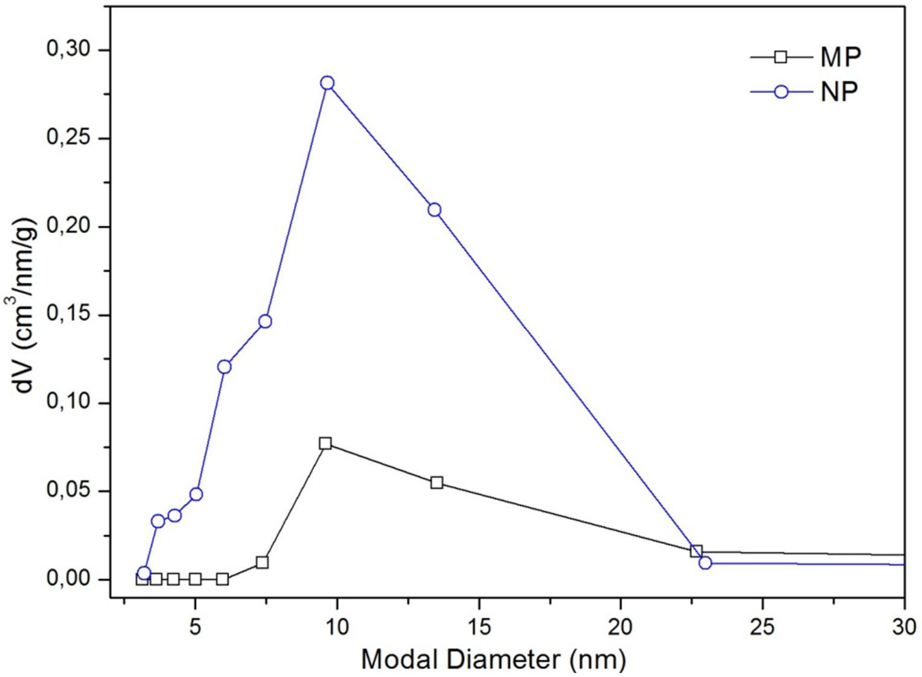

Figure 3.12: Pore size distributions of nano and micro bioactive glasses, obtained from BJH analysis of nitrogen sorption data.

The values for multipoint BET specific surface area (SA), BJH total pore volume, BJH pore diameter and average diameter of a spherical particle calculated from BET (Eq. 3.1) are listed in Table 3.4. Nanoparticles have a larger specific surface area than microparticles, 533.5 and 77.4 m^2/g, respectively, which means, a value almost 7 times higher, hence their properties can be dominated mostly by surfaces rather than bulk as compared to MP. The BET surface area is much greater than the calculated from TEM (Δ = 260%) because in the TEM estimative, it is considered dense particles, which means that the particle porosity is not take in acount. The particles present lower skeletal density when compared to theoretical density (2.62 g/cm^3). The diameter estimated from the BET method is also significantly lower than the measured by DLS analysis (relative deviation Δ = 860%). These results are attributed to the high porosity presented by the nanoparticles, as shown in the N_2 adsorption-desorption isotherms.

Table 3.4: Characterization summary obtained from nitrogen sorption isotherms of BGs particles.

Samples	ρ_s ***(g/cm^3)***	***SA (m^2/g)***	***Pore Volume (cm^3/g)***	***Pore Diameter (nm)***	****BET Estimated Diameter (nm)***
NP	2.25	533.5	1.11	9.7	5.0
MP	2.47	76.4	0.38	9.6	29.6

** Calculation considering the hypothesis that the particles are dense spheres*

Direct cytotoxicity evaluation. The mitochondrial activity of osteoblasts was evaluated by MTT assay after 24 hours (Fig. 3.13). There are significant differences between NP and MP when compared to control. MP exhibit an increase of 30% and NP of 80% in osteoblasts proliferation. Also, the difference is significant when nano and micro particles are compared. These results suggest that osteoblasts exhibit an increase in proliferation when in contact with nanoparticles, 50% higher than MP.

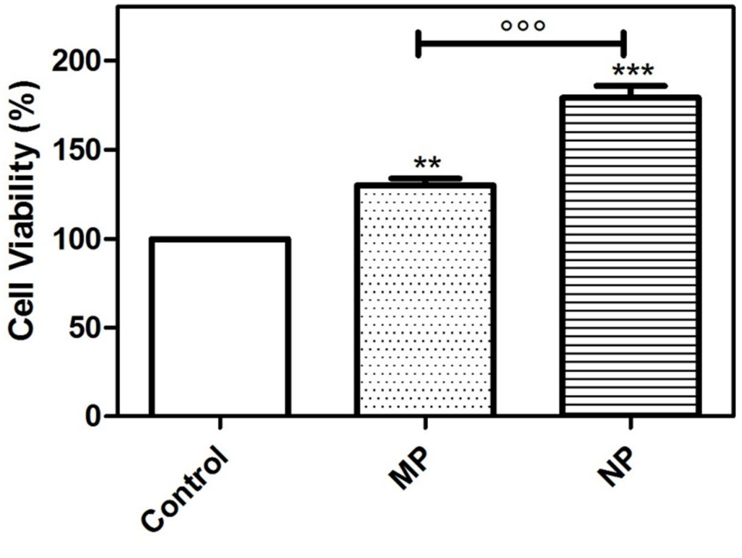

Figure 3.13: Osteoblast viability in contact with BG micro and nano particles after 24 hours of culture, by MTT assay. (* Represents significant difference compared to control and ° represents significant difference between MP and NP at a significance level of 0.05 %)

The difference in cell viability obtained between nano and micro particles can be explained by the differences in surface area and porosity, since the oxide composition was considered similar after EDS analysis. When the glasses are soaked in the medium, they release calcium ions from their surfaces via exchange with H_3O^+ ion in SBF, and the silica networks of the glasses are hydrated. As a result, a lot of Si-OH groups are formed on their surfaces. These *Si-OH* groups might be responsible for the apatite nucleation [1, 2]. As the NP presented significant larger surface are, it is reasonable to assume that density the of *Si-OH* groups is also significantly increased in this glass surface. It is known that the prerequisite for biomaterials to bond to living tissues is the formation of a crystalline HA layer on their surfaces under physiological conditions and that the formation of HA layers on BGs significantly enhances their biocompatibility by promoting cellular processes. BGNPs are expected to be able to chemically bond to bone tissue with high biocompatibility when implanted *in vivo* with superior performance in comparison to the bioactive glass microparticles.

3.4 Conclusions

BGNP with spherical shape and controlled particle size of (87 ± 5) nm were obtained by modified Stöber method. The particle size can be controlled by synthesis parameters and heat treatment. The nanoparticles presented high specific surface area (534 m^2/g) and pore volume (1.11 cm^2/g). They have good dispersability on polar solvents, water and DMSO, which enable their use in composites. Also, the NPs show a considerable increase in cell viability as compared to microparticles (50% higher). These results suggest that BGNP could offer superior performance for developing bioactive materials in comparison to the bioactive glass microparticles.

References

1. Larry L. Hench. The story of bioglass. J Mater Sci: Mater Med (2006) 17:967–978
2. Tadashi Kokubo, Design of bioactive bone substitutes based on biomineralization process Materials Science and Engineering C 25 (2005) 97–104
3. Marivalda M Pereira, Arthur E Clark and Larry L Hench. Homogeneity of bioactive sol-gel derived glasses in the system SiO_2-CaO-P_2O_5. Journal of Material synthesis and processing 2 (1994) 3:189-195
4. Marivalda M Pereira, Arthur E Clark and Larry L Hench. Effect of texture on the rate of hydroxyapatite formation on gel-silica surface. J. Am. Ceram. Soc. 78 (1995) 9:2463-68
5. C. Pritsos, E. Kontonasaki, X. Chatzistavrou, L. Papadopoulou, F. Pappas, P. Koidis, K.M. Paraskevopoulos. Studying morphological characteristics of thermally treated bioactive glass ceramic using image analysis J. Eur. Ceram. Soc 25 (2005) 891
6. Daniel C. Cluppera, John J. Mecholsky Jra, Guy P. LaTorreb, David C. Greenspan. Bioactivity of tape cast and sintered bioactive glass-ceramic in simulated body fluid. Biomaterials 23 (2002) 2599–2606
7. Xiaofeng Chen, Yongchun Meng, Yuli Li, Naru Zha. Investigation on bio-mineralization of melt and sol–gel derived bioactive glasses. Applied Surface Science 255 (2008) 562–564
8. Delia S. Brauer, Natalia Karpukhina, Matthew D. O’Donnell, Robert V. Law, Robert G. Hill. Fluoride-containing bioactive glasses: Effect of glass design and structure on degradation, pH and apatite formation in simulated body fluid. Acta Biomaterialia xxx (2010) xxx–xxx (article in press)
9. Akiko Obata, Satoshi Nakamura, Kimihiro Yamashita. Interpretation of electrical polarization and depolarization mechanisms of bioactive glasses in relation to ionic migration Biomaterials 25 (2004) 5163–5169
10. Julian R. Jones, Olga Tsigkoua, Emily E. Coatesa, Molly M. Stevensa, Julia M. Polakb, Larry L. Hench. Extracellular matrix formation and mineralization on a phosphate-free porous bioactive glass scaffold using primary human osteoblast (HOB) cells Biomaterials 28 (2007) 1653–1663
11. Ian A. Silver, Judith Deas, Maria Erecinska. Interactions of bioactive glasses with osteoblasts in vitro: effects of 45S5 Bioglass, and 58S and 77S bioactive glasses on metabolism, intracellular ion concentrations and cell viability Biomaterials 22 (2001) 175-185
12. E. Hatzistavrou, X. Chatzistavrou, L. Papadopoulou, N. Kantiranis, E. Kontonasaki, A.R. Boccaccini, K.M. Paraskevopoulos. Characterisation of the bioactive behaviour of sol–gel hydroxyapatite–CaO and hydroxyapatite–CaO–bioactive glass composites Materials Science and Engineering C 30 (2010) 497–502
13. A. Balamurugan, G. Sockalingum, J. Michel, J. Fauré, V. Banchet, L. Wortham, S. Bouthors, D. Laurent-Maquin, G. Balossier. Synthesis and characterisation of sol gel derived bioactive glass for biomedical applications Materials Letters 60 (2006) 3752–3757

14. J.P. BorrajoT, P. Gonzalez, S. Liste, J. Serra, S. Chiussi, B. Leon, M. Perez-Amor The role of the thickness and the substrate on the in vitro bioactivity of silica-based glass coatings Materials Science and Engineering C 25 (2005) 187–193
15. Angela L. Andrade, Patrıcia Valerio, Alfredo M. Goes, Maria de Fatima Leite, Rosana Z. Domingues. Influence of morphology on in vitro compatibility of bioactive glasses Journal of Non-Crystalline Solids 352 (2006) 3508–3511
16. Chim H, Hutmacher DW, Chou AM, Oliveira AL, Reis RL, Lim TC, Schantz J-T. A comparative analysis of scaffold material modifications for load-bearing applications in bone tissue engineering. Int J Oral Max Surg (2006) 35 928–934.
17. Xiaohong Wanga, Hongchen Suna, Jiang Chang. Characterization of $Ca_3SiO_5/CaCl_2$ composite cement for dental application dental materials 24 (2008) 74–82
18. Mohammad Ahmad, Julian R Jones and Larry L Hench. Fabricating sol–gel glass monoliths with controlled nanoporosity. Biomed. Mater. 2 (2007) 6–10
19. Jung Sang Cho, Yun Chan Kang. Synthesis of spherical shape borate-based bioactive glass powders prepared by ultrasonic spray pyrolysis Ceramics International 35 (2009) 2103–2109
20. Oana Bretcanu, Xanthippi Chatzistavrou, Konstantinos Paraskevopoulos, Reinhard Conradt, Ian Thompsond, Aldo R. Boccaccini, Sintering and crystallisation of 45S5 Bioglass powder. Journal of the European Ceramic Society 29 (2009) 3299–3306
21. Shuyi Li, Lynsa Nguyen, Hairong Xiong, Meiyao Wang, Tom C Hu, Jin-Xiong She, Steven M. Serkiz, George G. Wicks, William S. Dynan. Porous-wall hollow glass microspheres as novel potential nanocarriers for biomedical applications. Nanomedicine: Nanotechnology, Biology, and Medicine 6 (2010) 127–136
22. Julie Elizabeth Gougha, Julian R. Jones, Larry L. Hench. Nodule formation and mineralisation of human primary osteoblasts cultured on a porous bioactive glass scaffold Biomaterials 25 (2004) 2039–2046
23. Marivalda M Pereira and Larry L Hench. Mechanisms of hydroxyapatite formation on porous gel-silica substrates. Journal of Sol-Gel Science and Technology 7 (1996) 59-68
24. Marlene B Coelho and Marivalda M Pereira. Sol-gel synthesis of bioactive glass scaffolds for tissue engineering: effect of surfactant type and concentration. Journal of Biomedical Materials Research Part B: Applied Biomaterials (2005) 75B (2) 451-456.
25. Valério P, Guimarães MHR, Pereira MM, Leite MF, Goes AM. Primary osteoblast cell response to sol-gel derived bioactive glass foams. J M S: Materials in Medicine. 2005; 16(9) 851-856.
26. Wei Xia, Jiang Chang. Well-ordered mesoporous bioactive glasses (MBG): A promising bioactive drug delivery system. Journal of Controlled Release 110 (2006) 522 – 530
27. Qiang Fu, Mohamed N. Rahaman, B. Sonny Bal, Roger F. Brown, Delbert E. Day. Mechanical and in vitro performance of 13–93 bioactive glass scaffolds prepared by a polymer foam replication technique Acta Biomaterialia 4 (2008) 1854–1864
28. Yufang Zhu, Chengtie Wu, Yogambha Ramaswamy, Emanuel Kockrick, Paul Simon, Stefan Kaskel, Hala Zreiqat. Preparation, characterization and in vitro bioactivity of mesoporous

bioactive glasses (MBGs) scaffolds for bone tissue engineering. Microporous and Mesoporous Materials 112 (2008) 494–503

29. Bo Lei, Xiaofeng Chen , Yingjun Wang, Naru Zhao, Chang Du, Liming Fang. Synthesis and bioactive properties of macroporous nanoscale SiO_2–CaO–P_2O_5 bioactive glass Journal of Non-Crystalline Solids 355 (2009) 2678–2681
30. R. Ravarian, F. Moztarzadeh, M. Solati Hashjin, S.M. Rabiee, P. Khoshakhlagh, M. Tahriri Synthesis, characterization and bioactivity investigation of bioglass/hydroxyapatite composites Ceramics International 36 (2010) 291–297
31. Devis Bellucci, Valeria Cannillo, Antonella Sola. Shell Scaffolds: A new approach towards high strength bioceramic scaffolds for bone regeneration. Materials Letters 64 (2010) 203–206
32. C.J. Shih, W.C. Chen, Y.T. Wang, Synthesis and in vitro bioactivity of mesoporous bioactive glass scaffolds, Materials Science & Engineering C (2010), doi: 10.1016/j.msec.2010.02.006
33. Juan Peña, Jesús Román, M. Victoria Cabañas, María Vallet-Regí, An alternative technique to shape scaffolds with hierarchical porosity at physiological temperature. Acta Biomaterialia 6 (2010) 1288–1296
34. Daniel Arcos, María Vallet-Regí. Sol–gel silica-based biomaterials and bone tissue regeneration. Acta Biomaterialia xxx (2010) xxx–xxx (article in press)
35. K. Rezwan, Q.Z. Chena, J.J. Blakera, Aldo Roberto Boccaccinia. Biodegradable and bioactive porous polymer/inorganic composite scaffolds for bone tissue engineering. Biomaterials 27 (2006) 3413–3431
36. Pereira MM, Jones J, Hench LL: Bioactive glass and hybrid scaffolds prepared by sol–gel method for bone tissue engineering Adv in Appl Ceram (2005) 104:35-42.
37. K.A. Padmanabhan. Mechanical properties of nanostructured materials. Materials Science and Engineering A304–306 (2001) 200–205
38. T.J. Webster, R.W. Siegel, R. Bizios. Osteoblast Adhesion on Nanophase Ceramics. Biomaterials 20 (1999) 1221.
39. T.J. Webster, C. Ergun, R.H. Doremus, R.W. Siegel, R. Bizios. Nanoceramic surface roughness enhances osteoblast and osteoclast functions for improved orthopaedic/dental implant efficacy j. Biomed. Mater. Res. 51 (2000) 475.1261.
40. Ostomel TA, Shi Q, Tsung CK, Liang H, Stucky GD., Spherical bioactive glass with enhanced rates of hydroxyapatite deposition and hemostatic activity. Small. (2006) 11 1261-5.
41. D.Z. Chen, C.Y. Tang, K.C. Chan, C.P. Tsui, Peter H.F. Yu, Mason C.P. Leung, P.S. Uskokovic. Dynamic mechanical properties and in vitro bioactivity of PHBHV/HA nanocomposite. Composites Science and Technology 67 (2007) 1617–1626
42. Oliveira AAR, Oréfice, RL, Mansur HS, Pereira MM. Effect of Increasing Polyvinyl Alcohol Content on the Porous Structure and Mechanical Properties of Sol-Gel Derived Hybrid Foams Key Engineering Materials. 361-363 (2008) 555-558
43. Costa H, Oliveira AAR, Oréfice, RL, Mansur HS, Pereira MM. Tailoring Mechanical Behavior of PVA-Bioactive Glass Hybrid Foams Key Engineering Materials. 361-363 (2008) 289-292

44. Herman S. Mansur, Hermes S. Costa. Nanostructured poly(vinyl alcohol)/bioactive glass and poly(vinyl alcohol)/chitosan/bioactive glass hybrid scaffolds for biomedical applications. Chemical Engineering Journal 137 (2008) 72–83
45. Tiiu Niemela, Henna Niiranen, Minna Kellomaki. Self-reinforced composites of bioabsorbable polymer and bioactive glass with different bioactive glass contents. Part II: In vitro degradation. Acta Biomaterialia 4 (2008) 156–164
46. V. Cannillo, F. Chiellini, P. Fabbri, A. Sola. Production of Bioglass 45S5 – Polycaprolactone composite scaffolds via salt-leaching. Composite Structures 92 (2010) 1823–1832
47. Chengtie Wu, Yufeng Zhang, Yufang Zhu, Thor Friis, Yin Xiao. Structure–property relationships of silk-modified mesoporous bioglass scaffolds. Biomaterials 31 (2010) 3429–3438
48. Xuejun Wang, Guojun Song, Tao Lou. Fabrication and characterization of nano-composite scaffold of PLLA/silane modified hydroxyapatite Medical Engineering & Physics 32 (2010) 391–397
49. Kyung-Tae Noh, Hye-Young Lee, Ueon-Sang Shin, Hae-Won Kim. Composite nanofiber of bioactive glass nanofiller incorporated poly(lactic acid) for bone regeneration Materials Letters 64 (2010) 802–805
50. Abeer M. El-Kady, Ebtsam A. Saad, Bothaina M. Abd El-Hady, Mohmmad M. Farag aSynthesis of silicate glass/poly(L-lactide) composite scaffolds by freeze-extraction technique: Characterization and in vitro bioactivity evaluation Ceramics International 36 (2010) 995–1009
51. Superb K. Misra, F. Ohashi, Sabeel P. Valappil, Jonathan C. Knowles, I. Roy f, S. Ravi P. Silva, Vehid Salih, Aldo R. Boccaccini. Characterization of carbon nanotube (MWCNT) containing P(3HB)/bioactive glass composites for tissue engineering applications Acta Biomaterialia 6 (2010) 735–742
52. Mathew Petera, N.S. Binulala, S.V. Naira, N. Selvamurugana,b, H. Tamurac, R. Jayakumara, Novel biodegradable chitosan–gelatin/nano-bioactive glass ceramic composite scaffolds for alveolar bone tissue engineering Chemical Engineering Journal 158 (2010) 353–361
53. Aixue Liu, Zhongkui Hong, Xiuli Zhuang, Xuesi Chen, Yang Cui, Yi Liu, Xiabin Jing. Surface modification of bioactive glass nanoparticles and the mechanical and biological properties of poly(L-lactide) composites Acta Biomaterialia 4 (2008) 1005–1015
54. Daniela S. Couto, Zhongkui Hong, João F. Mano. Development of bioactive and biodegradable chitosan-based injectable systems containing bioactive glass nanoparticles. Acta Biomaterialia 5 (2009) 115–123
55. Wadcharawadee Noohom, Kevin S Jack, Darren Martin and Matt Trau. Understanding the roles of nanoparticle dispersion and polymer crystallinity in controlling the mechanical properties of HA/PHBV nanocomposites Biomed. Mater. 4 (2009) 015003 (13pp)
56. Abeer M. El-Kady, Ashraf F. Ali, Mohmmad M. Farag. Development, characterization, and in vitro bioactivity studies of sol–gel bioactive glass/poly(L-lactide) nanocomposite scaffolds Materials Science and Engineering C 30 (2010) 120–131

57. Tobias J. Brunner, Robert N. Grass and Wendelin J. Stark. Glass and bioglass nanopowders by flame synthesis. Chem. Commun. (2006) 1384–1386
58. Sen Lin, Claudia Ionescu, Kevin J. Pike, Mark E. Smithb and Julian R. Jones. Nanostructure evolution and calcium distribution in sol–gel derived bioactive glass J. Mater. Chem., 2009, 19,
59. Wei Xia, Jiang Chang. Preparation and characterization of nano-bioactive-glasses (NBG) by a quick alkali-mediated sol–gel method Materials Letters 61 (2007) 3251–3253
60. Wei Xia a,b, Jiang Chang. Preparation and characterization of nano-bioactive-glasses (NBG) by a quick alkali-mediated sol–gel method. Materials Letters 61 (2007) 3251–3253
61. G.S. Pappas, P. Liatsi, I.A. Kartsonakis, I. Danilidis, G. Kordas. Synthesis and characterization of new SiO2–CaO hollow nanospheres by sol–gel method: Bioactivity of the new system. Journal of Non-Crystalline Solids 354 (2008) 755–760
62. Zhongkui Hong, Esther G. Merino, Rui L. Reis and Joao F. Mano. Novel Rice-shaped Bioactive Ceramic Nanoparticles. Advanced Engineering Materials (2009) 11 (5) 25-29
63. Zhongkui Hong, Aixue Liu, Li Chen, Xuesi Chen. Xiabin Jing. Preparation of bioactive glass ceramic nanoparticles by combination of sol–gel and coprecipitation method. Journal of Non-Crystalline Solids 355 (2009) 368–372
64. Hong Z, Reis RL, Mano JF. Preparation and in vitro characterization of novel bioactive glass ceramic nanoparticles. J Biomed Mater Res A, in press. Preparation of bioactive glass ceramic nanoparticles by combination of sol–gel and coprecipitation method Journal of Non-Crystalline Solids 355 (2009) 368–372
65. Zhongkui Hong, Aixue Liu, Li Chen, Xuesi Chen, Xiabin Jing. Preparation of bioactive glass ceramic nanoparticles by combination of sol–gel and co-precipitation method. Journal of Non-Crystalline Solids 355 (2009) 368–372
66. Hui-suk Yun, Seung-eon Kim, Young-taek Hyun. Preparation of bioactive glass ceramic beads with hierarchical pore structure using polymer self-assembly technique. Materials Chemistry and Physics 115 (2009) 670–676
67. L. Borum, O.C. Wilson Jr. Surface modification of hydroxyapatite.Part II.Silica. Biomaterials 24 (2003) 3681–3688.
68. Anna M. Lipski a, Christopher J. Pino b, Frederick R. Haselton b, I.-Wei Chen a, V. Prasad Shastri. The effect of silica nanoparticle-modified surfaces on cell morphology, cytoskeletal organization and function. Biomaterials 29 (2008) 3836–3846.
69. Sneha Kulkarni, Asad Syed, Sanjay Singh, Anil Gaikwad, Kashinath Patil, K. Vijayamohanan, Absar Ahmad, Satishchandra Ogale. Silicate nanoparticles by bioleaching of glass and modification of the glass surface. Journal of Non-Crystalline Solids 354 (2008) 3433–3437.
70. Aneta J. Mieszawska, Nikolaos Fourligas, Irene Georgakoudi, Nadia M. Ouhib, David J. Belton , Carole C. Perry, David L. Kaplan. Osteoinductive silkesilica composite biomaterials for bone regeneration. Biomaterials 31 (2010) 8902-8910.
71. Alejandro Simón de Dios, Marta Elena Díaz-García. Multifunctional nanoparticles: Analytical prospects. Analytica Chimica Acta 666 (2010) 1–22.

72. Sheyda Labbaf , Olga Tsigkou , Karin H. Müller , Molly M. Stevens, Alexandra E. Porter, Julian R. Jones. Spherical bioactive glass particles and their interaction with human mesenchymal stem cells in vitro. Biomaterials 32 (2011) 1010-1018.
73. Werner Stöber, Arthur Fink and Ernst Bohn. Controlled growth of monodisperse silica spheres in the micron size range. J. Colloid Interface Sci. 26 (1968) 62-69.
74. C. Jeffrey Brinker and George W. Scherer. The sol-el science the physics and chemistry of sol-gel processing. Academic Press, Inc. (1990) ISBN 0-12-134970-5.
75. Masuo Hosokawa, Kiyoshi Nogi, Makio Naito and Toyokazu Yokoyama. Nanoparticle Technology Handbook. Elsevier (2007) ISBN 9780444531223.
76. G.H. Bogush, C.F. Zukoski. Studies of the kinetics of the precipitation of uniform silica particles through the hydrolysis and condensation of silicon alkoxides. J. Colloid Interface Sci. 142 (1991) 1:1-18.
77. G.H. Bogush, C.F. Zukoski, J. Uniform silica particle precipitation: An aggregative growth model. J. Colloid Interface Sci. 142 (1991) 1:19-34.
78. D.L. Green, J.S. Lin, Yui-Fai Lam, M.Z.-C. Hu, Dale W. Schaefer and M.T. Harris. Size, volume fraction, and nucleation of Stober silica nanoparticles. Journal of Colloid and Interface Science 266 (2003) 346–358.
79. Kota Sreenivasa Rao, Khalil El-Hami, Tsutomu Kodaki, Kazumi Matsushige. A novel method for synthesis of silica nanoparticles. Journal of Colloid and Interface Science 289 (2005) 125–131.
80. Joon Sang Park, Hoe Jin Hah, Sang Man Koo and Young Sik Leea. Effect of Alcohol Chain Length on Particle Growth in a Mixed Solvent System. Journal of Ceramic Processing Research 7 (2006) 1: 83-89
81. I.A. Rahmana, P. Vejayakumaran, C.S. Sipaut, J. Ismail, M. Abu Bakar, R. Adnana, C.K. Cheeb. An optimized sol–gel synthesis of stable primary equivalent silica particles. Colloids and Surfaces A: Physicochem. Eng. Aspects 294 (2007) 102–110.
82. Yao Xu, · Dong Wu, · Yuhan Sun, · Hongchang Gao, · Hanzhen Yuan · Feng Deng. A new study on the kinetics of Stöber synthesis by in-situ liquid ^{29}Si NMR. J Sol-Gel Sci Techn 42 (2007) 13–20 DOI 10.1007/s10971-006-1518-2.
83. Diego Adolfo Santamarıa Razo, Luca Pallavidino, Edoardo Garrone, Francesco Geobaldo, Emiliano Descrovi, Angelica Chiodoni, Fabrizio Giorgis. A version of Stöber synthesis enabling the facile prediction of silica nanospheres size for the fabrication of opal photonic Crystals. J Nanopart Res 10 (2008) 1225–12.
84. Xiao-Dong Wang, Zheng-Xiang Shen, Tian Sang, Xin-Bin Cheng, Ming-Fang Li, Ling-Yan Chen, Zhan-Shan Wanga. Preparation of spherical silica particles by Stöber process with high concentration of tetra-ethyl-orthosilicate. Journal of Colloid and Interface Science 341 (2010) 23–29.
85. Olivia Niitsoo, Alexander Couzis. Facile synthesis of silver core – silica shell composite nanoparticles. Journal of Colloid and Interface Science 354 (2011) 887–890.

86. Myung Han Lee, Frederick L. Beyer, Eric M. Furst. Synthesis of monodisperse fluorescent core-shell silica particles using a modified Stöber method for imaging individual particles in dense colloidal suspensions. Journal of Colloid and Interface Science 288 (2005) 114–123.
87. E.T. Vandenberg, L. Bertilsson, B. Liedberg, K. Uvdal, R. Erlandsson, H. Elwing, I. Lundstrom, Structure of 3-aminopropyltriethoxysilane on silicon oxides, J. Colloid Interface Sci. 147 (1991) 103–118.
88. F. Hoffmann, M. Cornelius, J. Morell, M. Froba, Silica-based mesoporous organic–inorganic hybrid materials, Angew. Chem. Int. Ed. 45 (2006) 3216–3251.
89. I.A. Rahman, M. Jafarzadeh, C.S. Sipaut. Synthesis of organo-functionalized nanosilica via a co-condensation modification using g-aminopropyltriethoxysilane (APTES). Ceramics International 35 (2009) 1883–1888.
90. F. Branda, B. Silvestri, G. Luciani, A. Costantini. The effect of mixing alkoxides on the Stöber particles size. Colloids and Surfaces A: Physicochem. Eng. Aspects 299 (2007) 252–255.
91. J.J. Razink, N.E. Schlotter. Correction to ‘‘Preparation of monodisperse silica particles: Control of size and mass fraction’’ by G.H. Bogush, M.A. Tracy and C.F. Zukoski IV, Journal of Non-Crystalline Solids 104 (1988) 95–106. Journal of Non-Crystalline Solids 353 (2007) 2932–2933.
92. Coleman NJ, Hench LL. A gel-derived mesoporous silica references materials for surface analysis by gas sorption, part 1—textural features. Ceram Int (2000) 26:171–8.
93. Barrett EP, Joyney LG, Halenda PP. The determination of pore volume and area distributions in porous substances I: computations from nitrogen isotherms. J Am Chem Soc (1951) 73:373–80.
94. Sing KSW, Everett DH, Haul RAW, Moscou L, Pierotti RA, Rouquerol J, et al. Reporting physisorption data for gas/solid systems. Pure Appl Chem (1985)57:603–19.
95. S Bau , O Witschger, F Gensdarmes, O Rastoix, D Thomas. A TEM-based method as an alternative to the BET method for measuring off-line the specific surface area of nanoaerosols. Powder Technology 200 (2010) 190–201.
96. RaH mila, M. Vallet-Regí. Static and dynamic in vitro study of a sol-gel glass bioactivity. Biomaterials 22 (2001) 2301-2306.
97. S. Padilla, J. Roman, S. Sanchéz-Salcedo, M. Vallet-Regí. Hydroxyapatite/SiO_2–CaO–P_2O_5 glass materials: In vitro bioactivity and biocompatibility. Acta Biomaterialia 2 (2006) 331–342.
98. Mohamed Mami, Anita Lucas-Girot, Hassane Oudadesse, Rachida Dorbez-Sridi, Fatima Mezahi, Elodie Dietrich. Investigation of the surface reactivity of a sol–gel derived glass in the ternary system SiO_2–CaO–P_2O_5. Applied Surface Science 254 (2008) 7386–7393.
99. Shan Zhao, Yanbao Li, Dongxu Li. Synthesis and in vitro bioactivity of SiO_2–CaO–P_2O_5 mesoporous microspheres. Microporous and Mesoporous Materials 135 (2010) 67–73.
100. Julian R. Jones, Lisa M. Ehrenfried, Larry L. Hench. Optimising bioactive glass scaffolds for bone tissue engineering. Biomaterials 27 (2006) 964–973
101. J. Ma, C.Z. Chen, D.G. Wang, X.G. Meng, J.Z. Shi. Influence of the sintering temperature on the structural feature and bioactivity of sol–gel derived SiO_2–CaO–P_2O_5 bioglass. Ceramics International 36 (2010) 1911–1916.

102. Masayuki Taira, Masayuki Okazaki and Junzo Takahashi. Characterization of 50wt% SiO_2- 20wt% P_2O_5- 30wt% CaO Glass-ceramic Powders Prepared by the Sol-gel Process. Dental Materials Journal 16 (1997) 2: 117-126,

4 Bioactivity evaluation of 60%SiO_2-36%CaO-4%P_2O_5 glasses micro and nano sized

Abstract. *Bioactive glasses (BG) bond to bone by forming a hydroxiapatite (HA) layer in vivo. In solution, the surface of BG undergoes a time-dependent modification. The formation of a HA layer in vitro on a material surface is believed to indicate its bioactive potential in vivo. Parameters such as surface charge, composition, structure, and morphology will be important in the formation of the Ca-P layer as well as in the interaction between the material surface and the surrounding medium, proteins and cells. The BG surface zeta potential variations in an electrolyte solution correspond to, and may directly influence Ca-P layer formation. In this study, the bioactivity of BG particles micro and nano sized was investigated by the time-dependent variations in zeta potential of BG immersed in SBF solution. FTIR, XRD and SEM analysis were used to confirm the formation of HA layer. The cell viability by MTT assay and alkaline phosphatase were used to evaluated the behavior of particles in direct contact with osteoblast cells. The zeta potential variations occurred faster and had higher variations for nanoparticles (NP). This result suggests that the kinetic of HA formation on BG particles is influenced by the particle size. The NP presented significant increase in cell viability when compared to microparticles (MP). These results support the hypothesis that BGNP are more bioactive than BGMP.*

4.1 Introduction

Hydroxiapatite (HA) is the predominant mineral phase of bone with smaller quantities of intermediate calcium phosphates and some calcium carbonate present. The *in vivo* HA layer formation occurs by the combination of calcium and phosphorus ionic forms, present in body fluid, to form calcium phosphate. First as dicalcium phosphate ($CaHPO_4$) and, through sequential reactions, becomes HA ($Ca_{10}(OH)_2(PO_4)_6$), or tricalcium phosphate ($Ca_3(PO_4)_2$). If cortical bone contained only mineral HA, a well-defined relationship between Ca and P should exist, Ca/P of 2.16. In general, for healthy mammals, the Ca/P ratio of cortical bones varies from different animals, sex, age and site, and the values range from 1.6 to 2.6 [1].

Bioactive glasses (BGs) bond to bone by forming a hydroxiapatite (HA) layer *in vivo*. In solution, the surface of BG undergoes a time-dependent modification. The formation of a HA layer *in vitro* on a material surface is believed to indicate its bioactive potential *in vivo*. Clearly, a bioactive behavior is an interface-driven phenomenon. Parameters such as surface charge, composition, structure, and morphology will be important in the formation of the Ca-P layer as well as in the interaction between the material surface and the surrounding medium, proteins and cells [2-9].

Several theories have been proposed to explain the formation of this layer. Kokubo et al [5] study the zeta potential of the surface of sodium titanate. The surface of the sodium titanate was highly negatively charged immediately after it was soaked in the SBF, attributed to Ti–OH groups. Then, the surface potential increased with increasing soaking time up to a maximum positive value, explained by the Ti–OH interaction with the positively charged Ca^{2+} ions in the fluid to form calcium titanate. Thereafter, it decreased with increasing soaking time, reached a negative value again, and finally converged to a constant negative value, attributed to the combination of the positive charged surface with negatively charged phosphate ions to form amorphous calcium phosphate, which spontaneously transforms into the apatite.

Lu et. al [6, 7] studied the quantification of BG (composition in mol.%: 46.1 SiO_2, 24.4 Na_2O, 26.9 CaO, 2.6 P_2O_5 (45S5)) surface zeta potential variations in a simulated body fluid (SBF) solution and hypothesize that time-dependent variations in BG zeta potential correspond to, and may directly influence, Ca-P layer formation. BG zeta potential varied continuously as a function of immersion time, surface and solution composition. They measured two sign reversals in the zeta potential of BG within 3 days of immersion. The first reversal from negative to positive after 1 day of immersion may be attributed to the adsorption of cations within the slip plane. These actions lead to the formation of an amorphous Ca-P layer. The second reversal was due to the precipitation of phosphate ions from the solution, which contributed to the growth and crystallization of the Ca-P layer. The surface was negatively charged after 3 days of immersion, and it remained negative after 7 days.

Yamashita and co-workers [8-10] have investigated the bone-like apatite growth on crystalline HA ($Ca_5(PO_4)_3OH$) and bioactive glass 45S5 surfaces after electrical polarization between blocking electrodes. Electrically polarizated HAs were made by the polarization of HA ceramics, in which ion dipole moments become aligned due to the external electrical field. The influence of the resulting surface charges on the bioactivity of HA was confirmed by the overgrowth of calcium phosphate layers on samples in contact with SBF, by the proliferation of certain cells in physiological fluids, and by an enhanced osteoconductivity during in vivo studies. When polarized HA samples were placed in SBF, calcium ions from the SBF were adsorbed readily on the negatively charged surface, followed by PO_4^{3-} deposition, resulting in an accelerated formation of bone-like apatite. Apatite crystal growth was accelerated on the negative surface, whereas no crystal growth was found on the positive surface after 3 days of immersion in SBF. The growth rate on the negative surface was about 10 μm/day, several times higher than that on non-polarized HA sample surfaces.

HA layer is spontaneously formed on the surface of glasses in the $CaO–SiO_2–P_2O_5$ system after exposure to SBF [2-4, 18-20]. The studies showed that apatite is formed preferentially on a glass surface mainly composed of CaO and SiO_2 because of the Ca^{2+} ions released from the glass increases the degree of supersaturation with respect to apatite of the surrounding fluid. Also, the *Si–OH* groups of the hydrated silica gel formed on the surface induce heterogeneous nucleation of apatite. These crystals grow by consuming calcium and phosphate ions from the body fluid and those that migrates from the bulk to the surface of the glass.

Recently, the concept of biological surface modification has opened new insights into biomaterial engineering. The biological response refers to the ability of the material to directly stimulate cell behaviour via proper biochemical signals. Bioactive glasses induce HA precipitation in physiological fluids and, thus, by anchoring to specific surface biomolecules, it is possible to improve tissue regeneration around implants, from both a chemical and biological point of view. Thereafter, cellular responses can be used to determine the role of the biomaterial in the tissue reaction and/or functional replacement as well as the fate of the biomaterial itself, such as biocompatibility, degradation and bioactivity [11].

Alkaline phosphatase (ALP) is an enzyme involved in bone formation and mineralization and is a well known and widely used as a marker of osteoblast differentiation *in vitro* tests and the assay is quite simple and relatively inexpensive. It has been suggested that ALP regulates phosphate metabolism and locally down-regulates inhibitors of apatite crystal growth [12].

Multiple studies have suggested that ALP activity is enhanced when cells are grown on bioactive glass in both animal-derived cells, human osteoblasts and rat mesenchymal stem cells [13-17]. Bioactive glasses had positive effects on bone apposition in both animal studies and clinical trials. A hypothesis for increased bone formation around bioactive glass implants is that either attachment to the bioactive glass or exposure to its dissolution products enhances osteoblastic differentiation from osteogenic precursors [14-17].

In this study, the bioactivity of BG particles is investigated by immersion of SiO_2-CaO-P_2O_5 glasses micro (38-150 μm) and nano (83-91 nm) sized in SBF. The time-dependent variations in BGs zeta potential and cell viability. FTIR, XRD, SEM and

EDS analysis are used to confirm the formation of HA layer. *In vitro* assays were used to determine osteoblast cells behavior in direct contact with BGs micro and nano sized particles.

4.2 Materials and methods

Samples preparation. Bioactive glasses with the nominal compositon wt %: 60% SiO_2, 36% CaO, and 4% P_2O_5 were used. These glass composition was extensively studied by the group [18-20] and showed an excellent potential to bone tissue engineering applications by presenting high level of bioactivity and development of a HA layer. The reagents used in the BGs synthesis were Tetraethyl Orthosilicate 98% (TEOS) and Triethyl Phosphate 99% (TEP) by *Sigma-Aldrich*, Methanol and Calcium Nitrate ($Ca(NO_3)_2.4H_2O$) by *Synth*, Nitric Acid (HNO_3) and 33% 33 % Ammonium Hydroxide solution (NH_4OH) by *Merck*.

For the BGNP synthesis, 200 ml of methanol was mixed with 0.46 ml of ammonium hydroxide 33% and 0.51 ml of water and stirred for 5 min. Then 5.57 ml TEOS and 0.56 ml TEP were added dropwise for 10 min. The sol was mechanic stirred for 48 h. The formed sol was placed in an oven at 50 °C until the complete ammonium evaporation (about 3 h). Then, the sol was filtered in a 0.22 μm *Milipore*. 3.46 g $Ca(NO_3)_2.4H_2O$ was dissolved in the sol and mixed for 24 h. The nanoparticles formed were separated by subsequently filtrations in a 0.22 and 0.11 μm *Milipore*. The sol filtered under 0.11 μm and submitted to freeze drying. The powders obtained were thermally treated at 200ºC for 40 min, with heating rate of 1ºC/min. At the end of the process, well dispersed bioactive glass nanoparticles, with average diameter of (87 ± 5) nm were obtained without grinding and sieving.

In order to compare the effect of particle size on the performance of bioactive glass, BGMP was prepared as described in previous works [19, 20]. 131.76 ml of water was mixed with 21.96 ml of nitric acid 1M and stirred for 5 min. Then 137.0 ml TEOS and 13.75 ml TEP were added dropwise for 10 min and the sol was mechanically stirred for

2 hours. 85.01 g $Ca(NO_3)_2.4H_2O$ was dissolved in the sol and mixed for more 1 hour. The gel obtained was aged for 72 hours and subsequently thermally treated at 700ºC for 360 min, with heating rate of 1ºC/min. The solids were ground and separated by sieving in the range of 38-150 μm.

In vitro bioactivity evaluation. Simulated body fluid (SBF) was prepared by dissolving NaCl 7.995 g, $NaHCO_3$ 0.353 g, KCl 0.224 g, $K_2HPO_4 \cdot 3H_2O$ 0.228 g, $MgCl_2 \cdot 6H_2O$ 0.305 g, $CaCl_2$ 0.227 g, and Na_2SO_4 0.071 g, all *Synth Brasil*, into distilled water. The solution was buffered at pH 7.4 by adjusting the volume amount of Tris (tris-hydroxymethylaminomethane) and HCl at 36.5 °C [4, 5].

The formation of a surface HA layer on the particles was evaluated upon immersion in SBF solution at time periods of 24, 48 and 72 hours. Surface structural observation was carried out after the immersed samples were removed from the SBF, washed three times with de-ionized water and dried in air circulation drying oven.

To examine the newly formed HA layer on the surface of the particles, the samples were analyzed by several techniques. The chemical structure of the BG particles was analyzed by Perkin Elmer 100 Spectrum Fourier transform infrared (FTIR), spectra in the mid-infrared range from 550 to 4000 cm^{-1} in μATR mode. Samples for FTIR analysis were diluted and ground in KBr with a sample to KBr dilution ratio of 1:100. X-ray Diffraction (XRD) spectra were collected on a Philips PW1700 series automated powder diffractometer using Cu Kα radiation at 40 KV/40 mA. Data was collected between 4.05 and 89.95° with a step of 0.06° and time of 1.5 second to identify any crystallization of the particles.

The morphologie and atomic composition of the BGNP, as well as the formation of the apatite layer on the surface of the particles, were observed by Scanning Electron Microscope (SEM) Tecnai G220 FEI and transmission electron microscope (TEM) Quanta 200v FEG FEI, both equipped with energy-dispersive X-ray (EDS).

Zeta potential data were measured using the Zetasizer 3000 HS Data Type 1256. BG particles were immersed in SBF at a weight-to-solution volume ratio of 0.1 mg/mL. Each sample was incubated at 37°C for 0, 6 and 24 hours, 3 and 7 days. Each data point for time-dependent changes in BG zeta potential in SBF represents the mean values calculated based on the average of nine histograms (n = 9).

Biological response. For the biological tests, neonatal Male Wistars rats, obtained from *Centro de Bioterismo da Universidade Federal de Minas Gerais* (CEBIO) were used for all studies. The investigation conforms to the Guide for the Care and Use of Laboratory Animals published by the US National Institutes of Health (*NIH publication No. 85-23, revised 1996*). Osteoblasts were isolated from calvaria of 1 - 5 days old neonatal Wistar rats. Then the calvaria were dissected and cut into small fragments and rinsed in Dulbecco's phosphate buffered saline without calcium and magnesium. The fragments were sequential digested, first with 1% trypsin/ EDTA for 5 minutes followed by four sequential digestions with 2% collagenase (180 unites/mL), *Sigma-Aldrich USA*, for 30 minutes each at 37°C. The first two digestions were discarded and the other three digestions produced a suspension of cells with osteoblasts. The three suspensions of cells were centrifuged for 5 minutes at 1000 G. The cells were cultured in DMEM with 10% fetal bovine serum (FBS), penicillin G sodium (10 unites/mL), streptomycin sulfate (10mg/ml) and 0,25 anfotericin-b, all *Gibco BRL USA*, in a humidified atmosphere of 5% CO_2 at 37°C. The cells were used for experiments on passage two.

The biological tests were performed according to ISO 10993 (*Part 5 - tests for in vitro cytotoxicity*). The BG particles were sterilized under UV radiation and mixed in the medium, with weight-to-solution volume ratio of 0.1 mg/mL, and soaked for 5 min. The mixed was placed directly over the osteoblast culture on the plates and maintained at 37°C under 5% CO_2 atmosfere. It was used phosphate-buffered saline (PBS), as positive control, and polyethylene (1 mg/ ml) sterilized under UV radiation, as negative control. Control cultures and seeded materials were characterised at 6, 24 and 72 hours for cell viability (Resazurine assay), and alkaline phosphatase (ALP) activity. The morphological changes indicating cytotoxicity and cell growth characteristics were recorded using a microscope. The experiments were performed in triplicate ($p < 0.05$

statistical analysis: One way/ ANOVA/ Bonferroni/ GraphPad Prism). To compare the results obtained, the absorbance values were expressed as a function of the control (without materials). The absorbance value obtained with the control was considered as indicating 100% viability. The relative percentages of viability were expressed in terms of the control.

Osteoblast viability was evaluated by Resazurine assay, based on a commercially available resazurin solution, *Sigma Aldrich USA*. Resazurine is a visible blue fluorogeneprobe, which is reduced to a red fluorescent compound (resorufin) by cellular redox enzymes [20]. Culture medium with BG particles were added to osteoblast cells (10^3 cell/ mm^3) cultured in 96-well plates in DMEM containing 10% FBS, penicillin G sodium (10 units/ml) and streptomycin sulfate (10 mg/ ml). After incubation times, the medium was removed and 180 μl of new culture medium supplemented with 10% of FBS was added to each well. 20μl of Resazurine (0.01 mg/ml) was added to each well and incubated for 24 hours at 37°C under 5% CO_2. After, the absorbance was measured with spectrophotometer ADAP 1.6 (Netherlands) at 570nm and 595 dual filter.

The quantitative ALP activity was assayed by reduction of p-nitophenol phosphate (BCIP/NBT), *Sigma-Aldrich USA*.The ALP production was evaluated by BCIP/NBT assay. This assay is based on achromagenic reaction initiated by the cleavage of the phosphate group of BCIP by alkaline phosphatase present in the cells. This reaction produces a proton which reduces NBT to an insoluble purple precipitate [12]. Cells were plated in 24-well culture plates (1×10^4 cells/well) and cultured in DMEM containing the BG powders, 10% FBS, penicillin G sodium (10 units/ml) and streptomycin sulfate (10 mg/ml). After incubation periods, the supernatant of each well was removed and the cell layer was rinsed twice with PBS. Then, 200 μl of BCIP-NBT solution was added to each well. Two hours later, the cells were observed by optical microscopy and the insoluble purple precipitates were solubilized with 210 ml of Sodium dodecylsulfate (SDS) 10% HCl, *American* Bioanalytical USA. The absorbance was measured with spectrophotometer ADAP 1.6 (Netherlands) at 595 nm filter.

4.3 Results and discussion

Zeta potential measurements. Zeta potential changes in BG immersed in SBF are shown in Figure 4.1. The data are indicative of a dynamic surface, as two sign reversals in the surface zeta potential were measured at different time period for BG particles micro and nano sized. The initial BG surface was negative in charge, with an average zeta potential of about -13 mV. The surface potential increased with increasing soaking time up to a maximum positive value. For the NP the surface became positive after 6 hours, reaching an average zeta potential of +21.0 mV. For the MP, the positive potential of +4.5 mV was only observed after 3 days in SBF. After, these potentials decreased with increasing soaking time and reached negative values again, remaining negative after 7 days immersion. The zeta potential values reached at this time were -6.9 and -2.1 mV to NP and MP, respectively.

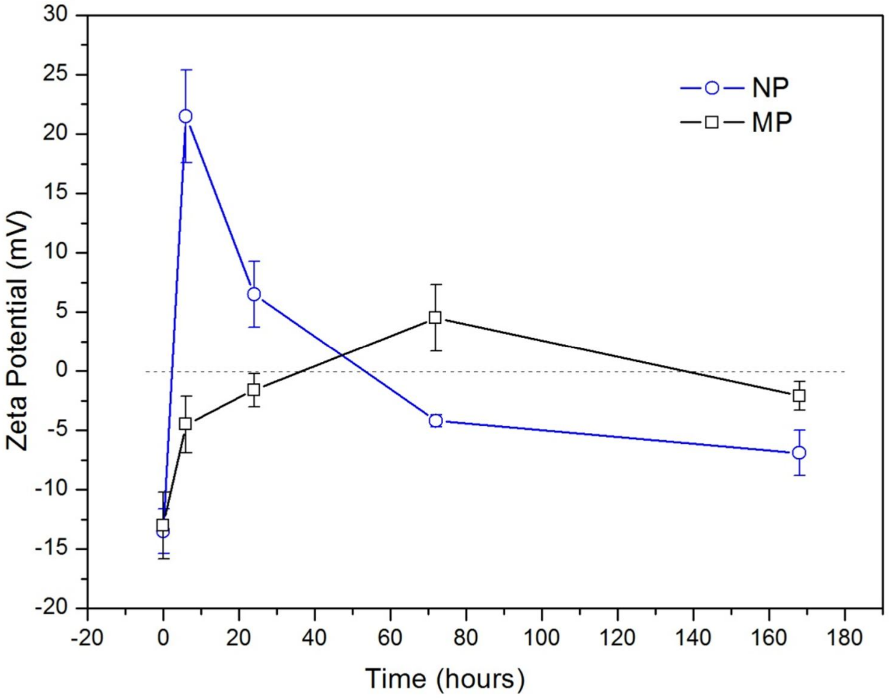

Figure 4.1: Zeta Potential of BG micro and nano sized particles immersed in SBF solution in different periods of time. Each data point represents the mean of values calculated based on the average of nine histograms (n = 9). The error bar represents the standard deviation of the mean.

The complex process of HA formation is extensively studied in the literature [2-11, 19]. A sequence of interfacial reactions, which begins immediately after BG is soaked in SBF, is interpreted in terms of the electrostatic interaction of the functional groups with the ions in the fluid. Fig. 4.2 represents how the zeta potential of the BG particle surfaces varies with SBF immersion times and shows a schematic representation of the chemical groups present on the surface as it changes with time. The reaction steps were divided in four different regions [4-6, 19]:

1) Initially, the surface became negative, attributed to the silanols (*Si-OH*) formed on BG particles upon soaking in SBF by two mechanisms: (i) The *-OH* formation occurred due to release the calcium ions (Ca^{2+}) from their surfaces via exchange with H_3O^+, Na^+ and K^+ ions in SBF, (ii) loss of soluble silica to solution, in $Si(OH)_4$ form, causing breaking of Si-O-Si bonds and silanols formation. As a result, a lot of *Si-OH* groups are formed on their surfaces and a local supersaturation of Ca^{2+} ions is established.

2) As time passes, it was occurred the selective combination of OH^- charged surface with the Ca^{2+} ions from the SBF solution. As the calcium ions accumulate on the surface, the surface gradually gains an overall positive charge (dark grey region).

3) The pH of SBF solution, at which the concentration of HPO_4^{2-} is much larger than that of PO_4^{3-}, favors the incorporation of HPO_4^{2-} ions into BG surface and migration of PO_4^{3-} ions from bulk to the surface of the glass. The result leads to calcium deficiency and the surface becomes negatively charged again (light grey region).

4) The calcium íons combined with the phosphate ions (PO_4^{3-} and HPO_4^{2-}) and formed amorphous calcium phosphates ($Ca_3(PO_4)_2$ and $CaHPO_4$). This calcium phosphates spontaneously transforms into the apatite by incorporation of OH^- and CO_3^{2-} anions from solution to form hydroxyl carbonate apatite (HCA) $Ca_5(PO_4CO_3)_3(OH)$ layer. Once apatite nuclei form, crystals grow by consuming calcium and phosphate ions from the SBF (white region).

The zeta potential variations occurred faster and with higher variations in BGNP, suggesting that the kinetic of HA formation on particles is influenced by the particle size, probably due to of the significant difference in surface area, when micro (80 cm^3/g) and nano (530 cm^3/g) are compared. It is consistent to suppose that the particles with higher surface area has a larger number of *-OH* groups and improves the catalytic effect of the *Si-OH* groups for the HA nucleation. With the progess of chemical reactions, the surface turns completely covered by the apatite formed and has no longer *Si-OH* avaliable to start new HA nodules precipitation so the kinetic of reaction tends to stabilize. These results indicate that NP increase the kinetic of HA nucleation at the early stage of SBF soaking, but this effect decreases over time and the differences in growth of HA on nano and microparticles surface tends to be minimized after prolonged soaking times.

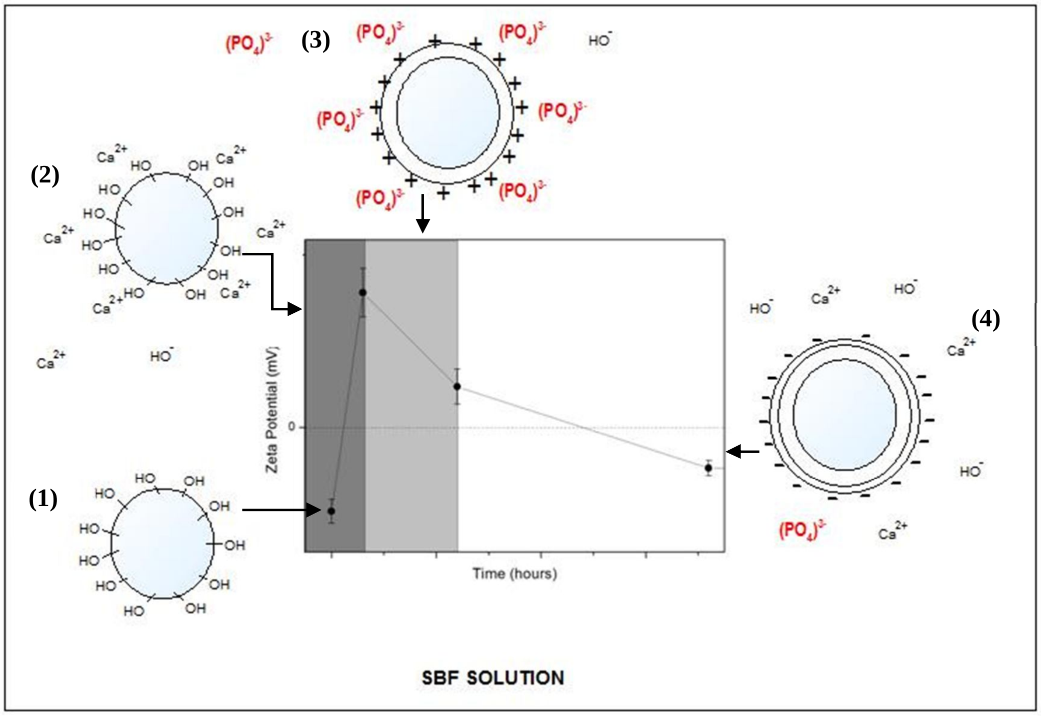

Figure 4.2: Schematic showing the relationship between the changes in surface structure of BG particles and the zeta potential during the HA formation process in SBF.

Structural characterization. After soaking in SBF for seven days, the BG particles were filtered and the obtained powders were analyzed by SEM. Particles soaked in water and filtered were also analyzed (Figs. 4.3 and 4.4). Figures 4.5 and 4.6 show the HA layer formed on BG micro and nano sized particles, respectively. In both particles, the surface was covered by HA layer nodules after immersion in SBF for 7 days. In the MP this nodules merged to form larger particles that populated the glass surface and can be easily identified in the SEM image (Figs 4.5 (c)). In the NP it is hard to say if these HA nodules were formed or if the HA layer only covered the surface of the glass, increasing significantly the particles size (Fig. 4.6 (c)).

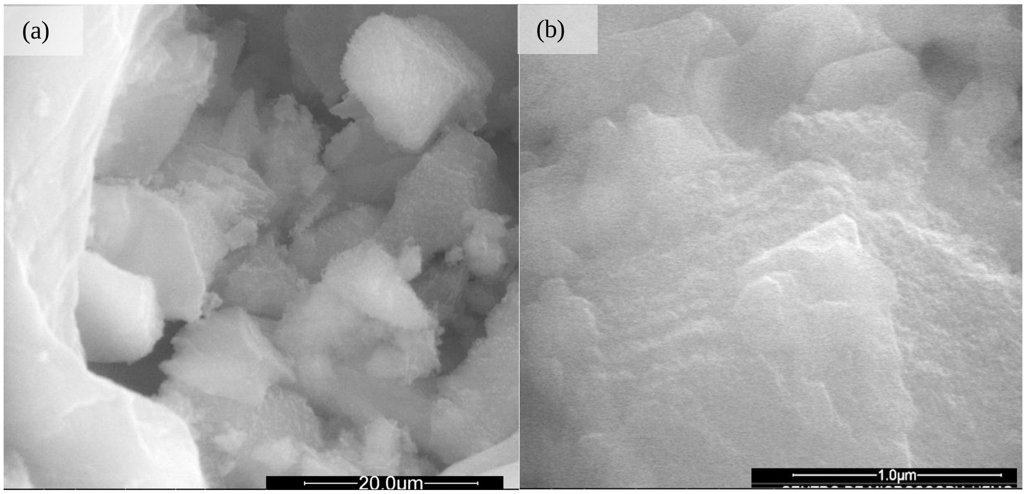

Figure 4.3: SEM images of BGMP after immersion in water. Image (b) is an magnification of image (a).

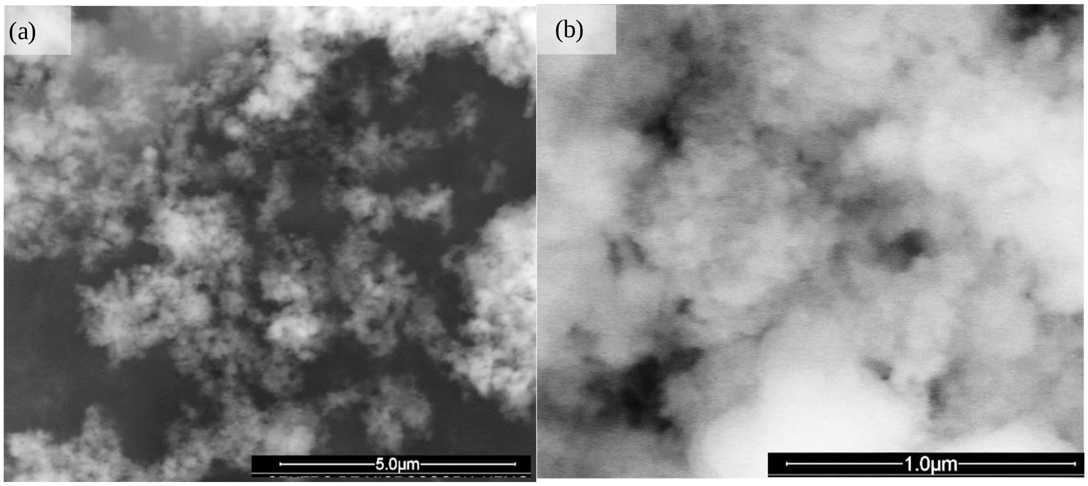

Figure 4.4: SEM images of BGNP after immersion in water. Image (b) is an magnification of image (a).

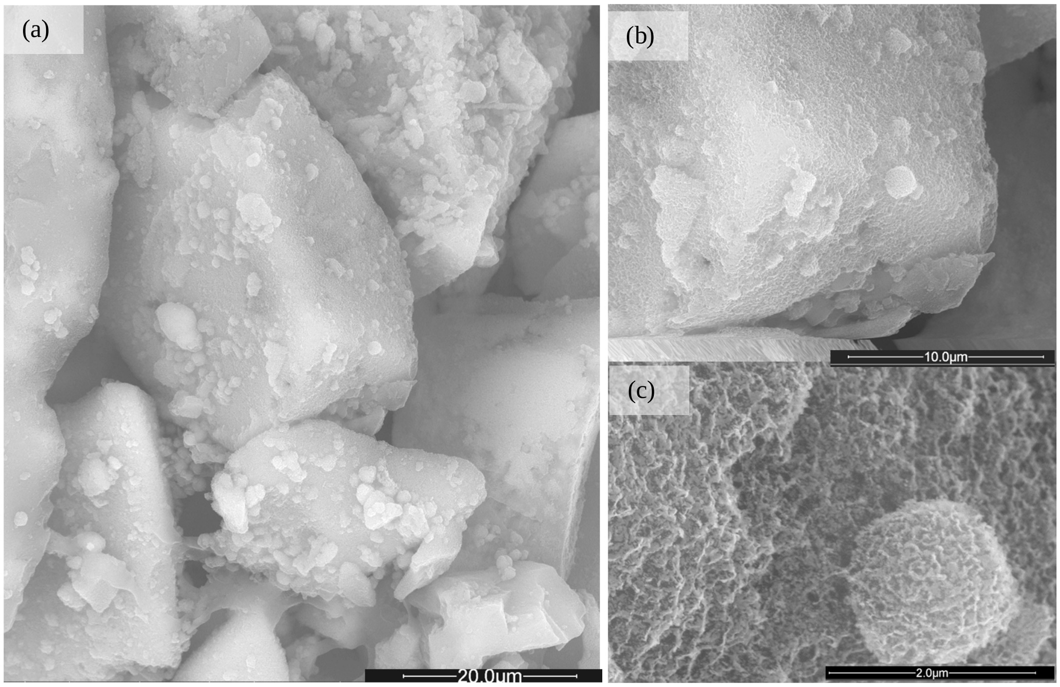

Figure 4.5: SEM images of BGMP after 7 days of immersion in SBF. Images (b) and (c) are magnifications of image (a).

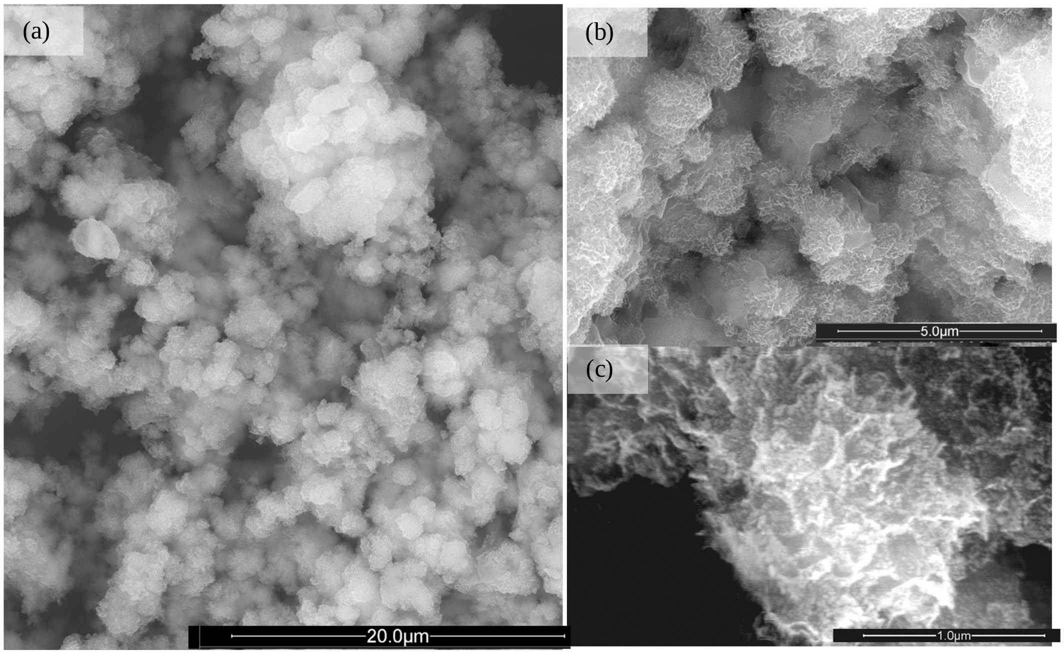

Figure 4.6: SEM images of BGNP after 7 days of immersion in SBF. Images (b) and (c) are magnifications of image (a).

In SBF, the concentration of silicon released into solution increases rapidly during the time of immersion [5, 6] and, consequently it is expected a silicon reduction on the material surface. Concurrent with the increase in silicon, the concentration of phosphorus decreases rapidly over the first few hours of dissolution. This behavior typically is attributed to the incorporation of phosphorus ions together with calcium ions from the dissolution medium within the Ca-P rich reaction layer forming on the glass surface [2-11].

The alterations of atomic composition that occurred on particle surfaces were monitored by EDS spectroscopy (Fig. 4.7). The spectra of MP and NP soaked in water show Si dissolution. The calcium and phosphorous contents increased, probably, driven by the different concentrations of Ca^{2+} and PO_4^{3-} ions between water and material, which led to the migration of these íons from solution to the surface of particles. When the micro and nano particles were soaked in SBF for 7 days, the peak intensities corresponding to Si decreases and the ones corresponding to Ca and P increase. The Si content decreased more in NP spectrum than in MP, which is attributed to higher Si dissolution in these particles. Estimated Ca/P ratio reached values compatible with Calcium Phosphate (CP) layer deposition, of 2.64 and 2.05, for micro and nanoparticles, respectively [1-6]. The Ca/P value of NPs is closer to the relationship between Ca and P in crystalline HA, which is 2.16. These results agree with the hypothesis that NP soaked in SBF had higher silanols density, and consequently, had a catalyzed CP deposition. These results agree with the hypothesis that NP soaked in SBF had higher silanols density, and consequently, had a catalyzed HA deposition.

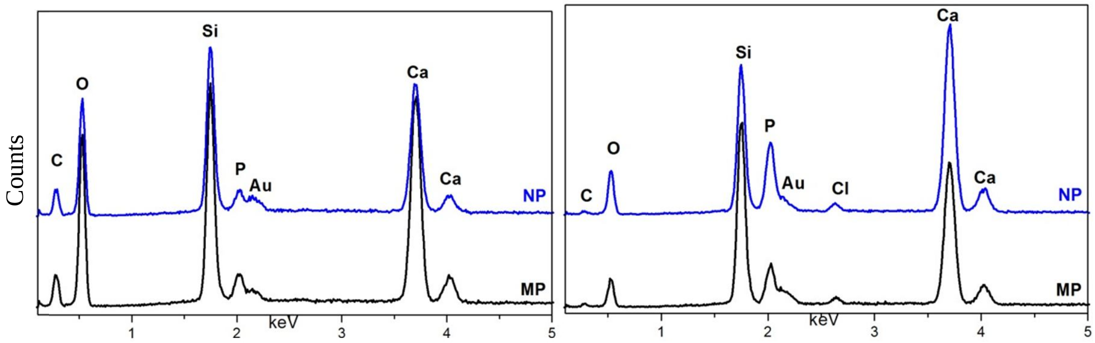

(a)   (b)

Figure 4.7: EDS of the areas showed on previous SEM images of BG micro and nanoparticles immersed in (a) water and (b) SBF.

FTIR was used to confirm the formation of the Ca-P layer on BG particles by detecting characteristic vibration modes of the P-O and P=O bonds after 7 days of immersion in SBF (Fig. 4.9) in comparison with the spectra obtained before SBF immersion (Fig. 4.8). The changes that occurred can be monitored by the appearance of several absorption bands in the spectra of samples immersed in SBF. The absorption band at 960 cm^{-1} is assigned to the P–O bond. The C-O stretching vibration appeared between 890 and 800 cm^{-1} suggesting the presence of carbonated Ca-P on the BG particles after SBF immersion. The divided P-O bending vibration peak between 600 and 500 cm^{-1}, an indicative of the development of a crystalline Ca-P layer, is cleary seen in both BGs spectra. In the NP spectrum, this band had already appeared, but after SBF immersion, its intensity was greatly increased. The band at 470 cm^{-1} is assigned to assimetric stretching of PO_4^{3-} groups [2-4, 18-20, 22-31].

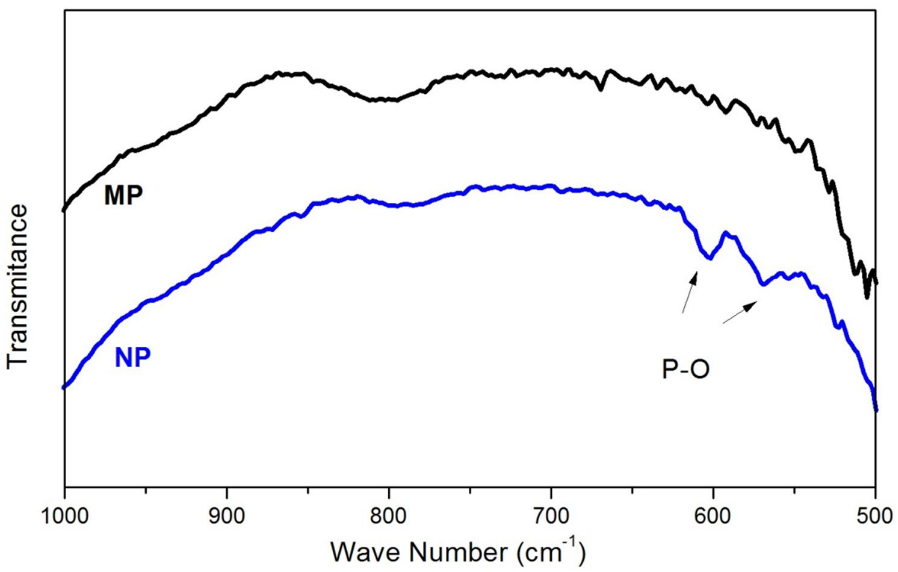

Figure 4.8: FTIR spectra of BG micro and nanoparticles before SBF immersion.

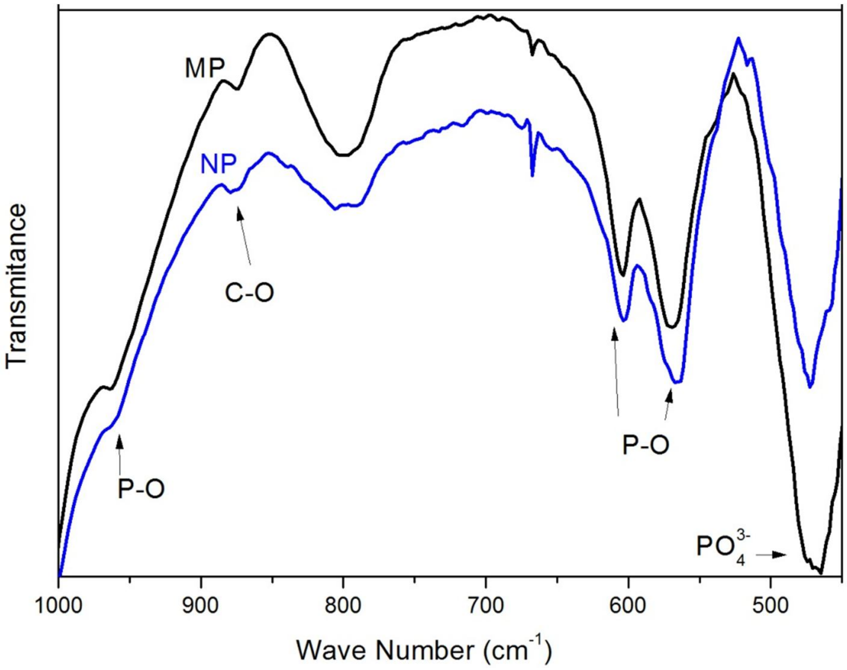

Figure 4.9: FTIR spectra of BG micro and nanoparticles after soaking in SBF for 7 days.

Figs. 4.10 and 4.11 show the XRD patterns obtained from the surfaces of the particles before and after soaking in SBF for 7 days. Crystalline peaks appear in the XRD patterns of BGs after 7 days in SBF. The peaks at 2θ value of 25.8 and 31.7 are assigned to (0 0 2) and (2 1 1) reflections of crystalline HA [2-4, 22-31]. Apatite formation on the surface of the glasse particles in the SBF is governed by chemical reaction of the surface of the matrix with the fluid. The intensity of two major reflections, (0 0 2) and (2 1 1), increase with an increase in the concentration of Ca^{2+} and PO_4^{3-} ions on the surface of the glass immersed in SBF for various days. The peaks assigned to these reflections are slightly better defined in nano sized particles, which suggests that NP has higher crystalline quality of HA crystals grown than microparticles.

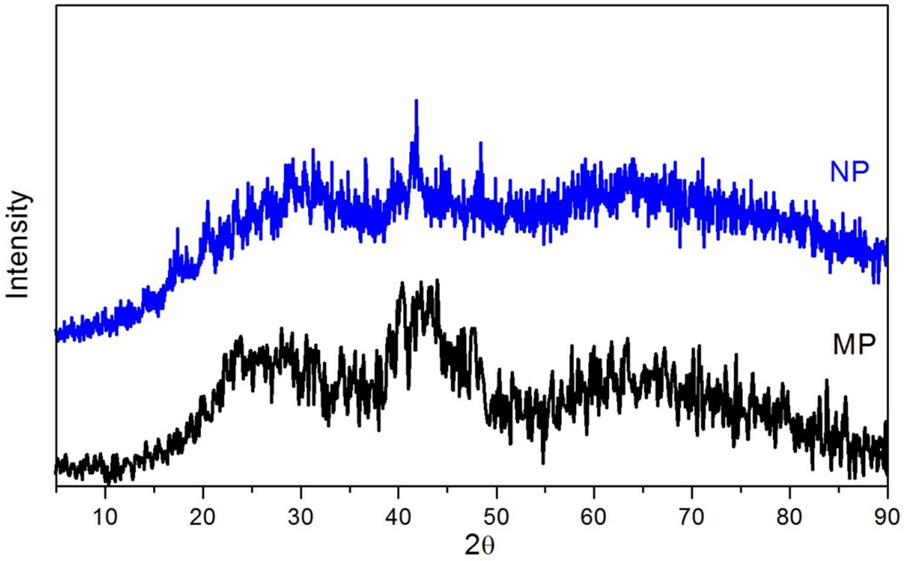

Figure 4.10: XRD patterns of BG micro and nano sized before SBF immersion.

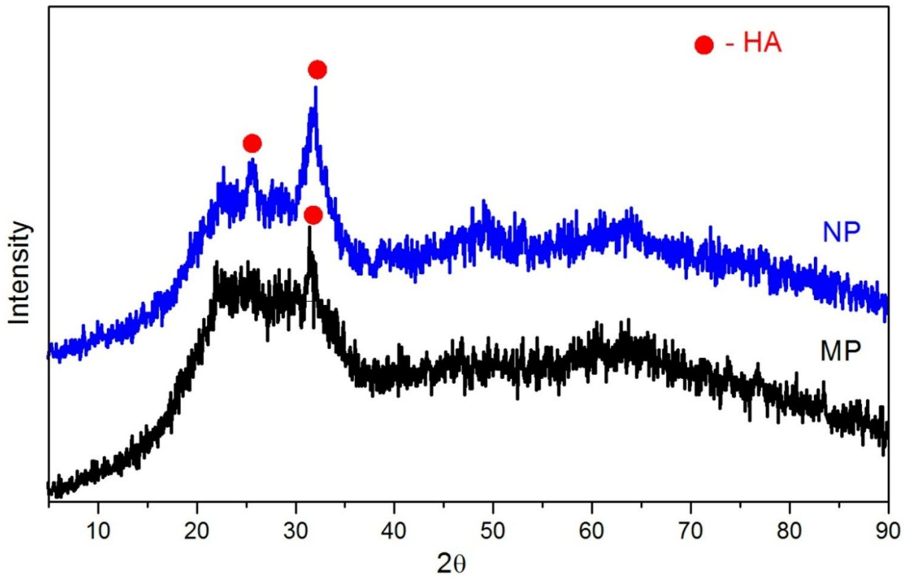

Figure 4.11: XRD patterns of BG micro and nano sized after soaking in SBF for 7 days.

Biological tests. The cell viability and ALP activity results after 6, 24 and 72 hours are presented in Fig. 4.12 and 4.13. In both assays, there are significant differences between NP and MP when compared to control. Also, there are signifficant differences when nano and micro particles are compared. Both cell viability and ALP activity of BG particles nano and micro sized showed an increase with duration of incubation. The results obtained with the different assays are summarized in Tab. 4.1. The Resazurine assay (Fig. 4.12) showed an osteoblast proliferation 27 and 16% higher in the presence of nanoparticles, when compared to microparticles, at periods of 6 and 24 hours, respectively. At 72 hours there was no significant difference between the particles. Results of ALP activity spectrophotometric measurements of osteoblast cells in direct contact with the BG nano and microparticles (Fig. 4.13) showed 58, 40 and 20% higher ALP activity of NP as compared to the MP, at periods of 6, 24 and 72 hours, respectively.

The biological studies support the hypothesis that BGNP are more bioactive than BGMP. It is consistent to assume that the increased HA nucleation on the nanoparticles surface is responsible for the higher stimulating effect on osteoblasts proliferation and ALP activity at the early stage of incubation. This effect decrease over time and the differences in osteoblasts proliferation in contact with nano and microparticles tends to be minimized after prolonged soaking, as oberserved in SBF bioactivity study.

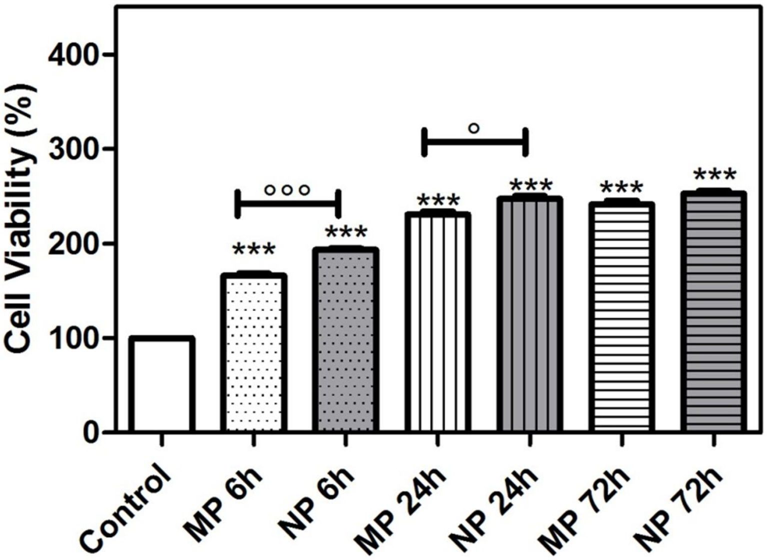

Figure 4.12: Cell viability of BG micro and nano particles after 6, 24 and 72 hours of culture measured by resazurine assay. * Represents significant difference compared to control and º represents significant difference between MP and NP at a significance level of 0.05 %.

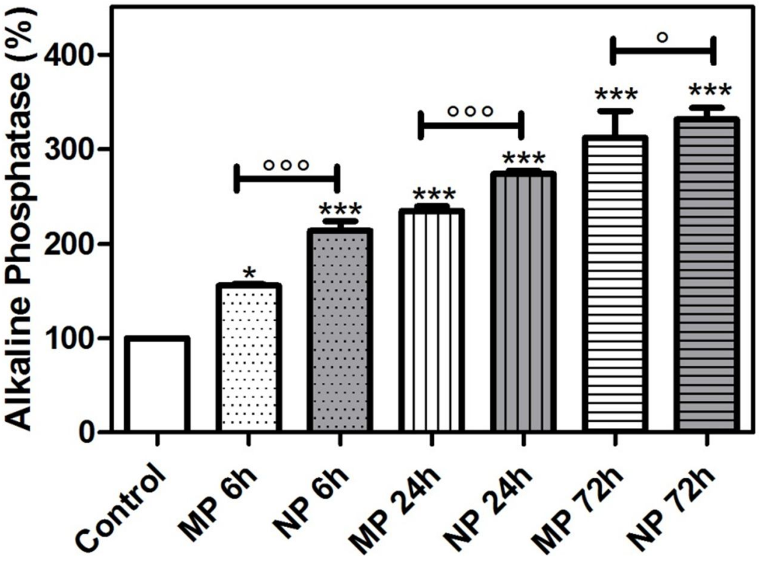

Figure 4.13: ALP activity of BG micro and nano particles after 6, 24 and 72 hours of culture. * Represents significant difference compared to control and ° represents significant difference between MP and NP at a significance level of 0.05 %.

Table 4.1: Summary of biological results obtained by Resazurine and ALP activity assays for BGs particles. The numbers represents the differences obtained as indicated.

Imersion times	***6h***	***24h***	***48h***
	Resazurine Cell Viability (%)		
MP compared to control	67	131	142
NP compared to control	94	147	153
NP compared to MP	27	16	ns
	ALP Activity (%)		
MP compared to control	55	135	212
NP compared to control	114	174	232
NP compared to MP	58	40	20

4.4 Conclusions

The relationship between time dependent variations in surface charge and the corresponding surface composition, structure, and morphology changes on BG micro and nano sized particles were examined in this study. BG zeta potential variations are related directly to surface Ca-P layer formation. Two sign reversals in the zeta potential of BG articles immersed on SBF were observed. The first reversal from negative to positive was attributed to the adsorption of cations within the slip plane. These actions lead to the formation of an amorphous Ca-P layer. The second reversal was due to the precipitation of phosphate ions from the solution, which contributed to the growth and crystallization of the Ca-P layer. The zeta potential variations occurred faster and had higher variations for BGNP, suggesting that the kinetic of HA formation in particles is influenced by the particle size, probably because of the significant difference in surface area, when micro and nano particles are compared. The increased HA nucleation on the nanoparticles surface is responsible for the higher stimulating effect on osteoblasts proliferation at the early stage of incubation. These results support the hypothesis that BGNP are more bioactive than BGMP.

References

1. Jeffrey O. Hollinger Thomas A. Einhorn, Bruce A. Doll and Charles Sfeir. Bone tissue engineering. CRC Press (2000) ISBN: 0-8493-1621-9.
2. Ducheyne P, Bianco P, Radin S, Schepers E. Bioactive materials: Mechanisms and bioengineering considerations. In: Bone bonding. Reed Healthcare Communications (1992) 1–12
3. Li P, Ohtsuki C, Kokubo T, Nakanishi K, Soga N, de Groot K. The role of hydrated silica, titania, and alumina in inducing apatite on implants. J Biomed Mater Res (1994) 28:7–15
4. Kokubo T, Kushitani H, Ohtsuki C, Sakka S. Chemical reaction of bioactive glass and glass–ceramics with a simulated body fluid. J Mater Sci: Mater Med (1992) 3:79–83
5. Kokubo T, Kim H-M, Kawashita M. Novel bioactive materials with different mechanical properties. Biomaterials 24 (2003) 2161–2175
6. Lu H, Pollack SR, Ducheyne P. Particle electrophoresis of 45S5 bioactive glass particles in simulated physiological electrolyte solutions. Proc Surf Biomater (1995) 24.
7. Helen H. Lu, Solomon R. Pollack, Paul Ducheyne. Temporal zeta potential variations of 45S5 bioactive glass immersed in an electrolyte solution. J Biomed Mater Res. (2000) Jul;51 (1):80-7.
8. Yamashita K, Oikawa N, Umegaki T. Acceleration and deceleration of bone-like crystal growth on ceramic hydroxyapatite by electric poling. Chem Mater 1996) 8:2697–700.
9. Ueshima M, Nakamura S, Yamashita K. Huge, Millicoulomb charge storage in ceramic hydroxyapatite by biomedical electric polarization. Adv Mater (2002)14:591–4.
10. Obata A, Nakamura S, Moriyoshi Y, Yamashita K. Electrical polarization of bioactive glass and assessment of their in vitro apatite deposition. J Biomed Mater Res (2003) 67A:413–20.
11. Tiejun Gao, Hannu T. Aro, Heimo YlaKnen, Eero Vuorio. Silica-based bioactive glasses modulate expression of bone morphogenetic protein-2 mRNA in Saos-2 osteoblasts in vitro. Biomaterials 22 (2001) 1475-1483
12. Enrica Verné, Sara Ferraris, Chiara Vitale-Brovarone, Silvia Spriano, Claudia L. Bianchi, Alberto Naldoni, Marco Morra, Clara Cassinelli. Alkaline phosphatase grafting on bioactive glasses and glass ceramics. Acta Biomaterialia 6 (2010) 229–240
13. Thomas J Webster, Celaletdin Ergun, Robert H Doremus, Richard W Siegel, Rena Bizios. Enhanced functions of osteoblasts on nanophase ceramics. Biomaterials 21 (2000) 1803-1810
14. ID. Xynos, MVJ Hukkanen, JJ Batten, LD Buttery, LL Hench, JM. Polak. Bioglass 45S5 Stimulates Osteoblast Turnover and Enhances Bone Formation In Vitro: Implications and Applications for Bone Tissue Engineering. Calcif Tissue Int (2000) 67:321–329
15. Patricia Valerio, Marivalda M. Pereira, Alfredo M. Goes, M. Fatima Leite. The effect of ionic products from bioactive glass dissolution on osteoblast proliferation and collagen production. Biomaterials 25 (2004) 2941–2948
16. Gwendolen C. Reillya, Shula Radinb, Andrew T. Chenc, Paul Ducheyneb. Differential alkaline phosphatase responses of rat and human bone marrow derived mesenchymal stem cells to 45S5 bioactive glass. Biomaterials 28 (2007) 4091–4097

17. V.G. Varanasi, E. Saiz, P.M. Loomer, B. Ancheta, N. Uritani, S.P. Hoa, A.P. Tomsia, S.J. Marshall, G.W. Marshall a. Enhanced osteocalcin expression by osteoblast-like cells (MC3T3-E1) exposed to bioactive coating glass (SiO_2–CaO–P_2O_5–MgO–K_2O–Na_2O system) ions. Acta Biomaterialia 5 (2009) 3536–3547
18. Marivalda M Pereira, Arthur E Clark and Larry L Hench. Homogeneity of bioactive sol-gel derived glasses in the system SiO_2-CaO-P_2O_5. Journal of Material synthesis and processing 2 (1994) 3:189-195
19. Marivalda M Pereira and Larry L Hench. Mechanisms of hydroxyapatite formation on porous gel-silica substrates. Journal of Sol-Gel Science and Technology 7 (1996) 59-68
20. Marlene B Coelho and Marivalda M Pereira. Sol-gel synthesis of bioactive glass scaffolds for tissue engineering: effect of surfactant type and concentration. Journal of Biomedical Materials Research Part B: Applied Biomaterials (2005) 75B (2) 451-456.
21. Thierry Pauloina, Mélody Dutot, Jean-Michel Warneta, Patrice Rat. In vitro modulation of preservative toxicity: High molecular weight hyaluronan decreases apoptosis and oxidative stress induced by benzalkonium chloride. European Journal of Pharmaceutical Sciences 34 (2008) 263–273
22. Tung MS. Calcium phosphate in biological and industrial system. Dordrecht, MA: Kluwer Academic Publishers (1998)
23. Hench LL. Bioceramics: From concept to clinic. J Am Ceram Soc (1991) 74(7):1487–1510
24. M. Vallet-Regí, A.M. Romero, C.V. Ragel, R.Z. LeGeros, J. Biomed. Mater. Res. 44 (1999) 416
25. Fujiu T, Ogino M. Difference of bone-bonding behavior among surface active glasses and sintered apatite. J Biomed Mater Res (1984) 18:845–859
26. Ducheyne P, Radin S, King L. The effect of calcium phosphate ceramic composition and structure on in vitro behavior. I. Dissolution. J Biomed Mater Res (1993) 27:25–34
27. Julian R. Jones, Lisa M. Ehrenfried, Larry L. Hench. Optimising bioactive glass scaffolds for bone tissue engineering. Biomaterials 27 (2006) 964–973
28. Qi-Zhi Chen, Kurosch Rezwan, Virginie Françon, David Armitage, Showan N. Nazhat, Francis H. Jones, Aldo R. Boccaccini. Surface functionalization of Bioglass-derived porous scaffolds. Acta Biomaterialia 3 (2007) 551–562
29. Zhongkui Hong, Aixue Liu, Li Chen, Xuesi Chen, Xiabin Jing. Preparation of bioactive glass ceramic nanoparticles by combination of sol–gel and coprecipitation method. Journal of Non-Crystalline Solids 355 (2009) 368–372
30. Mathew Peter, N.S. Binulal, S. Soumya, S.V. Nair, T. Furuike, H. Tamura, R. Jayakumar. Nanocomposite scaffolds of bioactive glass ceramic nanoparticles disseminated chitosan matrix for tissue engineering applications. Carbohydrate Polymers 79 (2010) 284–289
31. Xiaofeng Chen, Zhengmao Li, Cai Lin. The in vitro bioactive of sol–gel bioactive glass powders with three-dimensional lamellar structure. Advanced Powder Technology xxx (2010) xxx–xxx

5 Synthesis of biodegradable polyurethane aqueous dispersions containing alkoxide silane end groups

Abstract. *Polyurethanes (PU's) are used widely in biomedical applications because of their good physical and mechanical properties together with their biocompatibility characteristics. For some applications it would be necessary to use biodegradable polyurethanes, like scaffolds for tissue engineering. Their degradation products have to be biocompatible, non-toxic and metabolized or eliminated by the living organism. The chemistry involved in the synthesis of PU have three important components: macrodiol, diisocyanate and chain extender. In this work the PU synthesis was conducted by the prepolymer mixing process, the macrodiol components – polycaprolactone diol (PCL) 1000 and 2000 g/mol - 2,2-bis(hydroxymethyl) propionic acid (DMPA) and hexamethylene diisocyanate (HDI). The PU dispersion occurred by adding deionized water to the neutralized prepolymer which was stirred vigorously. Chain extenders (hydrazine and aminosilane) were added to finish the reaction. This chemical procedure was well succeeded in producing PU dispersions with solid content of about 20 wt%. Films were obtained by casting the dispersions in molds and allowing them to dry at room temperature. Porous scaffold were produced by dilution and freeze drying of the dispersion obtained. The films had 250% of deformation and the foams presented interconnected macroporous. The study of degradations products showed a moderate toxic effect and more studies have to be done to evaluate the release of these products at concentrations closer to the in vivo conditions.*

5.1 Introduction

Polyurethanes (PU’s) are used widely in biomedical applications such as heart valves, aortic grafts, and dialysis membranes, pacing leads insulation, catheters, intra-aortic balloons and mammary implants, because of their good physical and mechanical properties together with their biocompatibility characteristics [1, 3]. Most polyurethanes for biomedical uses are biostable materials, designed to stand in service for long periods of time and require materials resistant to degradation in the aggressive environment of the living tissues. However, for some applications it would be necessary to use biodegradable polyurethanes. Cardiovascular implants [4-7], artificial skin [8, 9], bone graft substitutes [10-12] and scaffolds for tissue engineering [13-17] are some examples of application in which biodegradability would be important.

Most of the biodegradable biomaterials have been stiff materials, useful for applications such as drug delivery systems or fracture fixation devices. In contrast, few biodegradable elastomeric polymers have been synthesized. Biodegradable elastomers are expected to be suitable for any application requiring the use of a flexible, elastic material such as in soft tissue engineering (e.g. skin, vasculature). The synthesis of highly variable synthetic segmented PU’s can be exploited to generate polymers having properties ranging from very soft elastomers to very rigid plastics. Their degradation products have to be biocompatible, non-toxic and metabolized or eliminated by the living organism [1-3, 13-21].

The chemistry involved in the PU synthesis is centered on the isocyanate reactions. The three important components of PUs are macrodiol, diisocyanate and chain extender. The synthesis of PU involves a reaction between a di- or polyisocyanate with a di- and/or polyol (Fig. 5.1). They react to form linear, segmented copolymers consisting of alternating hard segment (HS) and soft segment (SS), which originate a micro-phase separation caused by the incompatibility between these segments, determined by factors such as segmental lengths, hydrogen bonding (intraintermolecular interactions) and crystallization extent. SS is derived from polyols such as polyester. It is normally in the amorphous state and governs properties at low temperature. Crystallization of SS occurs only with low level of hard segment content or prolonged cooling. The HS is formed from the diisocyanate and chain extender and provides extra strength to the materials due to hydrogen bonding involving urethane linkages. They can act as thermo-reversible physical crosslinks for thermoplastic elastomers. Physicochemical properties may be modified by changing the ratio of SS to HS and their respective chemistries to suit the intended application [1-3].

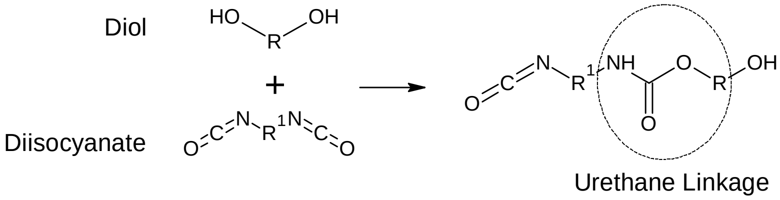

Figure 5.1: Polyurehane linkage

Biodegradable PU (BPU) can be obtained by the incorporation of groups susceptible to hydrolysis in the polymer chain, like the introduction of poly(ε-caprolactone) diols (PCL), poly(lactic acid) (PLA), polyglycolic acid (PGA), and poly(ethylene glycol) (PEG) polyols in the SS of the polymer skeleton [4-17]. Hexamethylene diisocyanate (HDI), 1,4-diisocyanatobutane (BDI) and l-lysine diisocyanate (LDI) are preferred over conventional aromatic diisocyanates [1].

Through the appropriate choice of SS chemistries, degradation can be tailored from weeks to years. The HS generally degrades slower than the SS predominantly due to urethane bonds being much less susceptible than ester bonds (of the SS) to hydrolytic degradation [1-3, 18-21]. The modification of HS by varying diisocyanate structures and chain extenders has been less explored than SS modifications to influence degradation and other properties. These investigations have mostly focused on understanding the effect of such structural changes on physical properties and cytocompatibility; however, the effect on PU in vitro degradation has seldom been investigated. The degradation rate of biodegradable PUs is governed by several factors. Most studies suggest that hydrolysis is the prevalent degradation pathway for *in vivo* degradation of PUs [1-3, 18-21].

Preparation of aqueous polyurethane dispersions have received increasing interest, owing to the continuous reduction in costs and the control of volatile organic compound emissions (environmental friendship) [22]. Biodegradable and aqueous dispersible PU's were developed by Ayres [23, 24] by the prepolymer mixing process (Fig. 6.2), using a 250 mL three-neck glass flask equipped with a heating bath, a mechanical stirrer and a thermometer, under nitrogen atmosphere. The macrodiol components-polycaprolactone-diol (PCL) 1250 and 2000 g/mol - 2,2-bis(hydroxymethyl) propionic acid (DMPA) and isophorone diisocyanate (IPDI), with NCO/OH ratio of 2:3, were added to the reactor in the presence of dibutyl tin dilaurate (DBDLT) and the reaction was carried out at 70 - 75°C under nitrogen atmosphere for 4 hours. The amount of free NCO groups on a percentage basis was determined by the standard di-butyl amine back titration method. After titration, the prepolymer temperature was allowed to drop to 40°C. The carboxylic acid groups were neutralized by the addition of triethylamine (TEA). The mixture was stirred for further 40 min to ensure the reaction was completed. The PU dispersion occurred by adding deionized water to the neutralized prepolymer which was stirred vigorously. After the dispersion, an amount of hydrazine enough to react with free NCO groups was added to the reactor with a small amount of water, and stirring was continued for further 30 min. This chemical procedure was successul in producing PU dispersions with solid content of about 25 wt%. Films were produced by casting the dispersions in a Teflon mold and allowing them to dry at room temperature for one week. Afterwards the films were placed in an oven at 60°C for 24 h for drying.

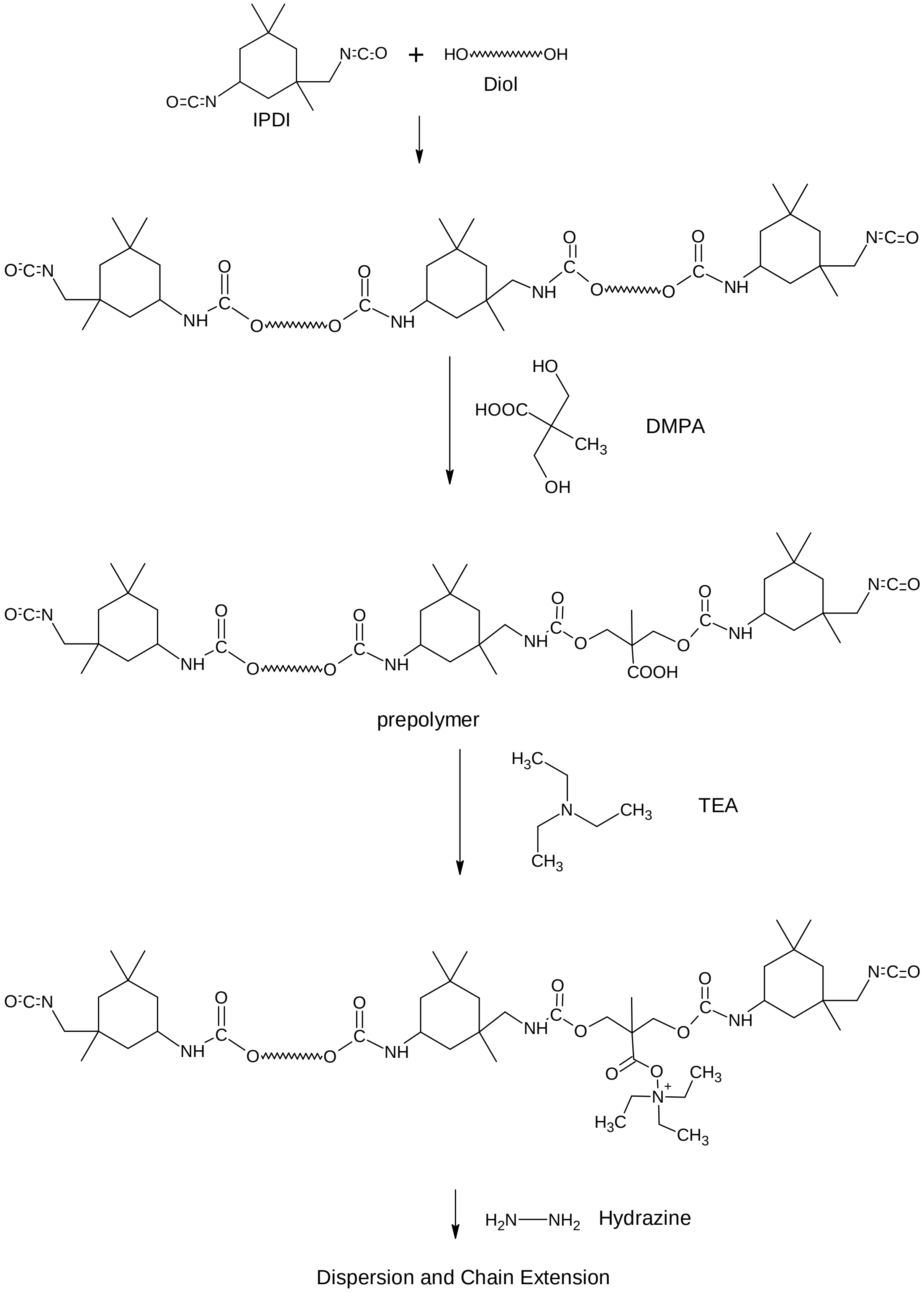

Figure 5.2: Schematic of polyurethane synthesis reactions.

The chains of the PU's can be extended by silane molecules, by the reaction of the prepolymer with amino silanes as APTES (3-aminopropyltriethoxysilane). Silanized polyurethane dispersions are generally composed of polyurethane backbones containing condensable end groups. During the water evaporation, these groups can undergo crosslinking reactions to form a stable siloxane linked network, which results in the improvement of the properties of the pure polyurethane. In addition, the incorporation of small inorganic domains in the nanoscale range gives rise to a synergetic combination of the properties of each of the constituents [22, 25-28]. Hydrolyzed silane species, derived from TMOS, TEOS and TEP, can be added to PU by condensed reactions with animo silanes groups to promote the production of the PU with inorganic particles [22]. This methodology can be used, for example, to developed bioactive composites, by the association of bioactive glasses and PUs.

In this work, it was proposed to use the Ayres route to obtain PU prepolymer, with some modifications in the synthesis, to obtain polymers with silane end groups. IPDI was replaced by HDI, which is less citotoxic than the aromatic diisocyanates commonly used in PU's chemistry [3, 29]. The chains were extended with APTES, besides TEA. The aim of this work is the development of membranes and scaffolds intending to associate biocompatibility, mechanical and physical properties in a material designed for tissue engineering applications.

5.2 Materials and Methods

Synthesis of biodegradable polyurethanes. Aqueous polyurethane dispersions were prepared by the prepolymer process, using a 250 mL three-neck glass flask equipped with a heating mantel and a mechanical stirrer. Then, this prepolymer was added to an aqueous premix to form the dispersion. The macrodiol components polycaprolactone-diol Mn 1250 g/mol (PCL 1250), polycaprolactone-diol Mn 2000 g/mol (PCL 2000), both by *Sigma-Aldrich*, and 2,2-bis(hydroxymethyl) propionic acid 98.3% (DMPA), by *Fluka*, were added to the reactor without any catalyst. The temperature was kept at 60°C. 30 minutes after melting of PCLs, hexamethylene diisocyanate (HDI), by *Sigma-Aldrich*, was added and the reaction was carried out at 80°C under nitrogen atmosphere for 2.5 h. The premix was prepared by the addition of triethylamine (TEA) and 24% hidrazine solution (HZ), both by *Miracema Nuodex Brazil*, and (3-aminopropyl) triethoxysilane (ATPES), by *Sigma-Aldrich*, were mixed in water for 30 min. The PU dispersion, with solid content about 20 wt%, occurred by the addition of prepolymer in the premix which was stirred vigorously until a milky dispersion was observed (Fig. 5.3 (a)). The dispersion remained stable up six months after the synthesis. The composition of the PU prepared is shown in Table 5.1. Films (Fig. 5.3 (b)) were produced by casting the dispersions in acrylic plates and allowing them to dry at room temperature for one week. Afterwards the films were placed in an oven at 60 °C for 72 h for heat treatment. For the foams produced (Fig 5.3 (c)), the PU dispersion was diluted, placed on cylindrical Teflon molds and freeze dried. Then, the foams had the same heat treatment as the films. The samples were sterilized by UV light. Unsterilized control specimens were included for comparative purposes showing the effects of sterilization. The nominal wt% Si content of the samples after drying is 1.5%.

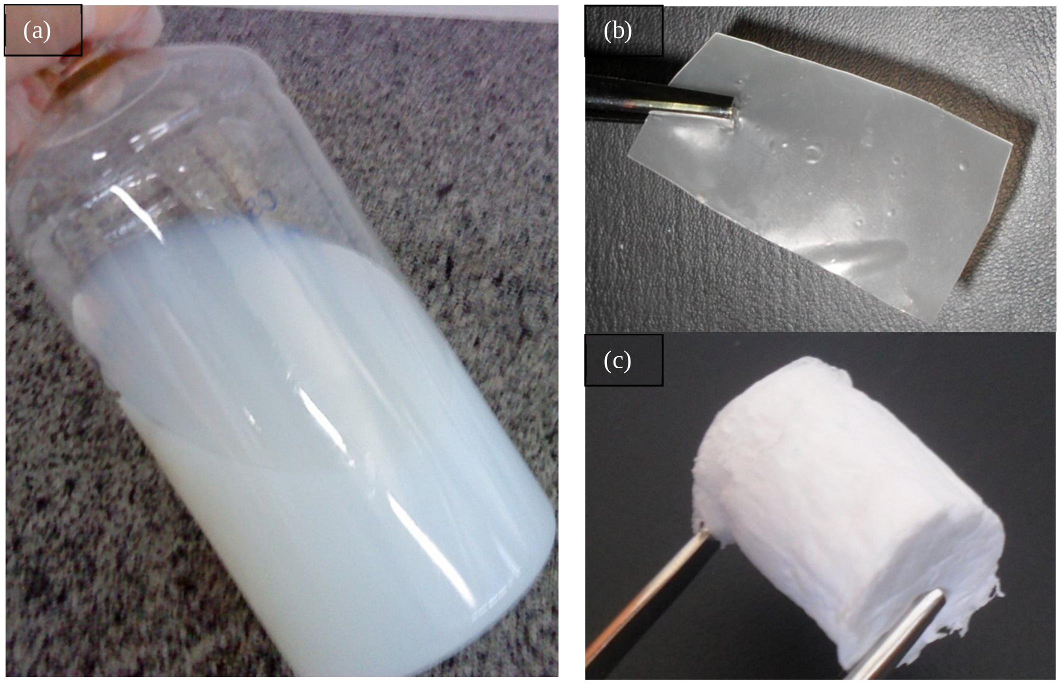

Figure 5.3: (a) Aqueous PU dispersion (b) films and (c) foams obtained.

Table 5.1: Amount of reagents employed for the preparation of polyurethane.

	Composition (wt %)				***Reaction Time (h)***
	PCL 1250	*PCL 2000*	*DMPA*	*HDI*	
Prepolymer	3.84	6.14	0.85	4.17	2.5
	H_2O	TEA	HZ	ATPES	
Premix	80.00	1.66	1.01	2.34	0.5

Materials characterization. The structure of the PU films was analyzed by Perkin Elmer 100 Spectrum Fourier transform infrared Spectrometer. Spectra were collected in the mid-infrared range from 550 to 4000 cm^{-1} in μATR mode. X-ray Diffraction (XRD) curves of the PU films were collected on a Philips PW1700 series automated powder diffractometer using Cu Kα radiation at 40 KV/40 mA. Data was collected between 4.05 and 89.95° with a step of 0.06° and a dwell time of 1.5 seconds. Morphologies of the PU films and foams were observed by Scanning Electron Microscope (SEM) Tecnai G220 FEI equipped with energy-dispersive X-ray (EDX).

The percentage porosity of the foams was calculated using eq. 5.1:

$$\%Porosity = 1 - \rho_r \qquad \text{Eq. 5.1}$$

where ρ_r is the relative density (Eq.5.2):

$$\rho_r = \frac{\rho_b}{\rho_s} \qquad \text{Eq. 5.2}$$

where ρ_b is the geometrical bulk density, calculated from the ratio of mass by volume of the cylindrical foams, and ρ_s is the skeletal density, which was estimated by the density of the films.

Mechanical tests on PUs were performed on an EMIC-DL3000 universal testing machine at ambient temperature. 50 N load cell and minimum of 5 test pieces were used in each test. The tensile testing of PU films were based on ASTM D 638-10 (*Standard Test Method for Tensile Properties of Plastics*) using a type IV die shape (thickness 0.15 mm) with a crosshead speed of 20 mm/min. Compressive testing of the PU foams was performed according to ASTM D 695 (*Standard Test Method for Compressive Properties of Rigid Plastics*) at speed of 5 mm/min in foams with cylindrical shape (diameter 10 mm and length 14 mm).

Degradation study. As the *in vivo* PU degradation mechanisms are not fully understood at the molecular level, the criteria for a successful in vitro predictive test are not well established. Many studies have proposed and used various tests and models, but as yet there is no consensus on the most meaningful test method for the predictive accelerated *in vitro* testing of candidate PU based biomaterials. As various degradation tests have been used to mimic the *in vivo* PU degradation, it is challenging to assess their utility and assess reported test outcomes. They indicate that most PU materials are stable towards simple hydrolysis (incubation in H_2O or buffer solution) at room temperature. But, PUs can be susceptible to hydrolysis upon exposure following incubation in water or buffer at 85°C. Hydrogen peroxide has been used to determine the stability of PUs towards hydrolysis and oxidation. Some studies reported substantial or total degradation with 5-30% hydrogen peroxide for 24 hours at temperatures between 70 and 100°C. The mechanism of peroxide attack is less clear; but these studies found that the polyether SS was susceptible to rapid degradation and the HS was being attacked in the degradation process. This medium is an interesting choice to mimic the *in vivo* PU degradation because hydrogen peroxide is a natural body metabolic product, secreted, for example, by some cells, as peroxidic molecular species, as part of the immune defense reactions [1].

The accelerated degradation test was used to mimic the *in vivo* PU degradation. PU foam samples were immersed in 30% hydrogen peroxide solution, with weight-to-solution volume ratio of 0.1 mg/mL, and incubated for 24 hours at temperature of 85 °C. The literature reports that under these conditions, at 1 hour of immersion, the most degradation products are from PU SS. The period of 24 hours is sufficient to degrade completely the PU, including the HS [1].

For the biological test, neonatal Male Wistars rats, obtained from *Centro de Bioterismo da Universidade Federal de Minas Gerais* (CEBIO) were used for all studies. The investigation conforms to the Guide for the Care and Use of Laboratory Animals published by the US National Institutes of Health (*NIH publication No. 85-23, revised 1996*). Osteoblasts were isolated from calvaria of 1 - 5 days old neonatal Wistar rats. Then the calvaria were dissected and cut into small fragments and rinsed in Dulbecco’s phosphate buffered saline without calcium and magnesium. The fragments were sequential digested, first with 1% trypsin/ EDTA for 5 minutes followed by four sequential digestions with 2% collagenase (180 unites/mL), *Sigma-Aldrich USA*, for 30 minutes each at 37°C. The first two digestions were discarded and the other three digestions produced a suspension of cells with osteoblasts. The three suspensions of cells were centrifuged for 5 minutes at 1000 G. The cells were cultured in DMEM with 10% fetal bovine serum (FBS), penicillin G sodium (10 unites/mL), streptomycin sulfate (10mg/ml) and 0,25 anfotericin-b, all *Gibco BRL USA*, in a humidified atmosphere of 5% CO_2 at 37°C. The cells were used for experiments on passage two.

The cytotoxicity test was performed according to ISO 10993 (*Part 5 - tests for in vitro cytotoxicity*). The cell viability was determined by MTT assay with 3-(4,5-dimethylthiazol-2-yl)-2,5-diphenyl-tetrazolium bromide, Sigma-Aldrich. Phosphate-buffered saline (PBS) was used as positive control and polyethylene as negative control. Osteoblasts were plated in 96 well culture plates at density of 1×10^3 cells/cm^3 per well. Cells were normalized with DMEM without FBS, and after this period the medium was aspirated and 200 µl of DMEM with PU degradation products (0.1 mg/ml) supplemented with 10% of FBS was added in each well. The degradation products were mixed in the medium without any filtration, to prevent the retention of products in the filter. The volume ratio of 0.1 mg/ml was used to reproduce the same conditions of the literature [1]. The mixture was placed directly over the culture and maintained under CO_2 atmosphere for 24 hours. After this period the medium was aspirated and 70 µl of new culture medium supplemented with 10% of FBS was added. 50 µL de MTT

(5mg/mL) was added to each well. Four hours later, formazan salts were dissolved with isopropanol 10%/HCl. The absorbance was measured at spectrophotometer ADAP 1.6 (Netherlands) with 595nm filter. The experiments were performed with n=8 ($p< 0.05$ statistical analysis: One way /ANOVA / Bonferroni / GraphPad Prism. Background signal (wells with no cells) was deducted from the absorbance values. To compare the results obtained, the absorbance values were expressed as a function of the control (without materials). The absorbance value obtained with the control was considered as indicating 100% viability. The relative percentages of viability were expressed in terms of the control.

5.3 Results and discussions

Structural characterization. The analysis of PU structures by infrared spectroscopy (FTIR) has been reported by several research groups in literature, which were used as reference [1-22]. In the Figures 5.4 and 5.5 are showed the FTIR spectra of polyurethane obtained and their respective magnification. The band between 3600 and 3100 cm^{-1} is the contribution of the stretching vibrations of several hydrogen–bonded *N–H* and *O–H* groups. The bands at 2940 and 2860 cm^{-1} are assigned, respectively, to C-H asymmetric and symmetric stretching in $–CH_2–$ groups. The bands between 1740 and 1560 cm-1 are composed by the overlap of the bands at 1730, 1670 and 1610 cm^{-1}, related to *C=O* stretching vibration in esther, urethane, urea, ester hydrogen bonded urethane structures; and 1640-1540 cm^{-1}, related to H bending vibration in secondary amide in the urethane bond. 1460 cm^{-1} is assigned to *C–H* scissors deformation in $–CH_2–$ groups. The band at 1240-1256 cm^{-1} is related to *C–N* stretching vibration mode in the *R-NH-COO-* group. 1160 cm^{-1} is assigned to *C–O–C* stretching vibration modes.

The incorporation of alkoxide silane in PU is manifested by the bands at 1200 and 1090 cm^{-1}, associated with LO and TO vibration modes, respectively, of *Si–O* bond. The band at 1040 cm^{-1} is assigned to *Si–O* stretching vibration modes. 570 cm^{-1} is referred to *Si-O-Si* bending mode. The band at 778 cm^{-1} is related to stretching vibration mode *C-O* in the *CO-O-C* groups in poly(ester urethanes) [31].

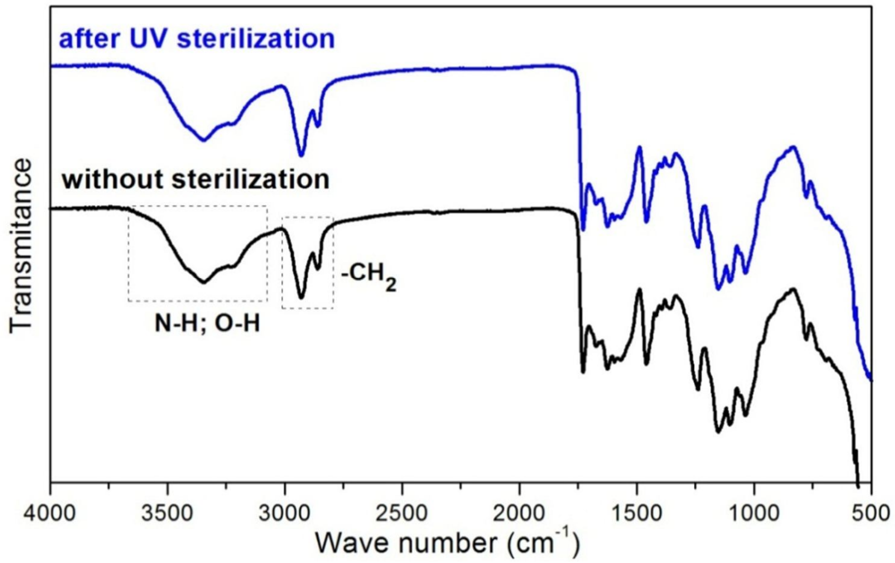

Figure 5.4: FTIR spectra of PU films before and after UV sterilization.

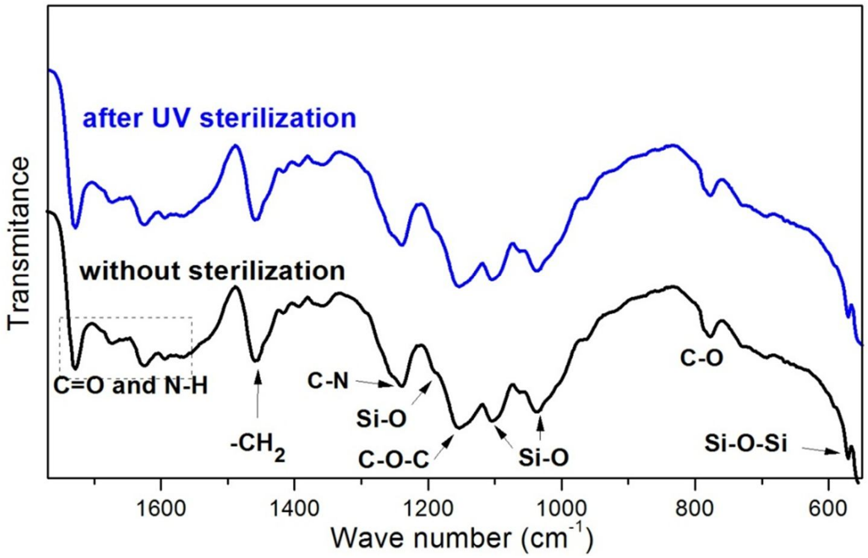

Figure 5.5: Magnification of FTIR spectra of PU films before and after UV sterilization.

The XRD patterns of PU films as produced and after sterilization are shown in Fig. 5.6. In general, films prepared from aqueous polyurethane dispersions do not exhibit the clear formation of crystalline segment domains that are found in many polyurethane elastomers or plastics. The chemistry of the film products and the need to coalesce into a continuous film precludes the high level of crystallinity that is found in typical melt or solvent processed polyurethanes [2]. Two distinct diffraction peaks are observed at 2θ at 21.3 and 23.8°, which were indexed as (110) and (200) planes, respectively, of an orthorhombic crystalline structure of PCL [31, 32]. The PCL crystallinity tends to increase with decreasing PCL molecular weight [32]. The PU produced presented high level of crystallinity as compared to others biodegradable PUs [1-3, 4-17, 23, 24]. Its crystallinity can be attributed to the low molar weight of PCL used.

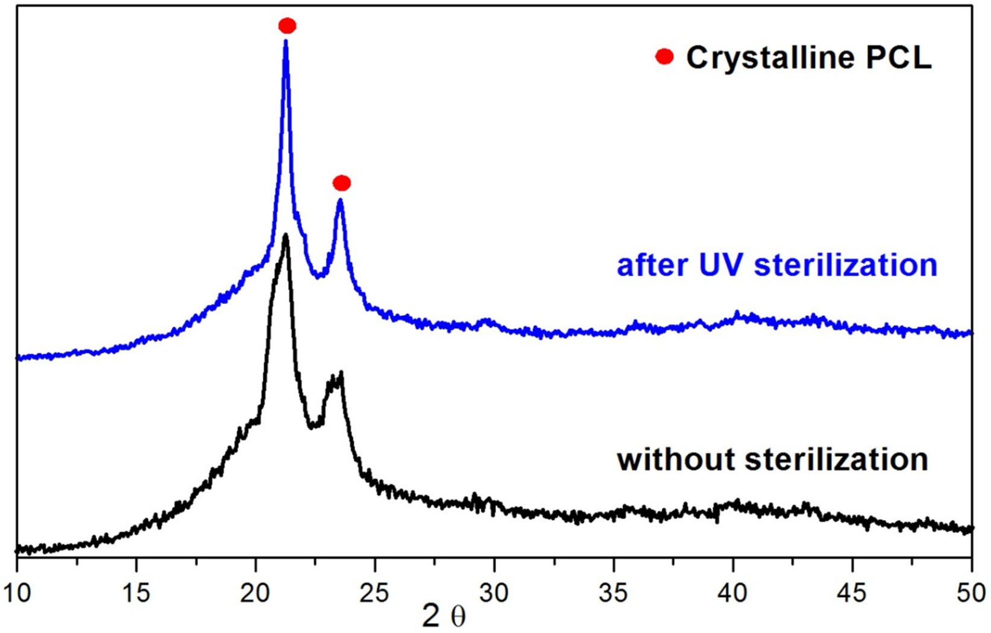

Figure 5.6: XDR pattern of PU films before and after UV sterilization.

The sterilization method is a constant concern about chemical modifications in PU chains. The analysis of FTIR and XRD suggest that the sterilization method adopted, the UV radiation, causes no significant changes in the chemical structure of the polymer.

The pore structure of the foams obtained by freeze drying the PU dispersion with solid content of 20, 10 and 2 wt% were observed by SEM (Fig. 5.7). In the foams produced from dispersions with 20 wt% of solid, it can be noted small, closed and lined pores, without interconnected structure. As the dispersions were diluted, they produced foams with open larger pores. The samples prepared from dispersions with 10 wt% solids presented pores still aligned and interconnections linking these pores can be observed. The foams produced from dispersions with 2 wt% solid showed no organized structure, with high level of interconnectivity between the pores.

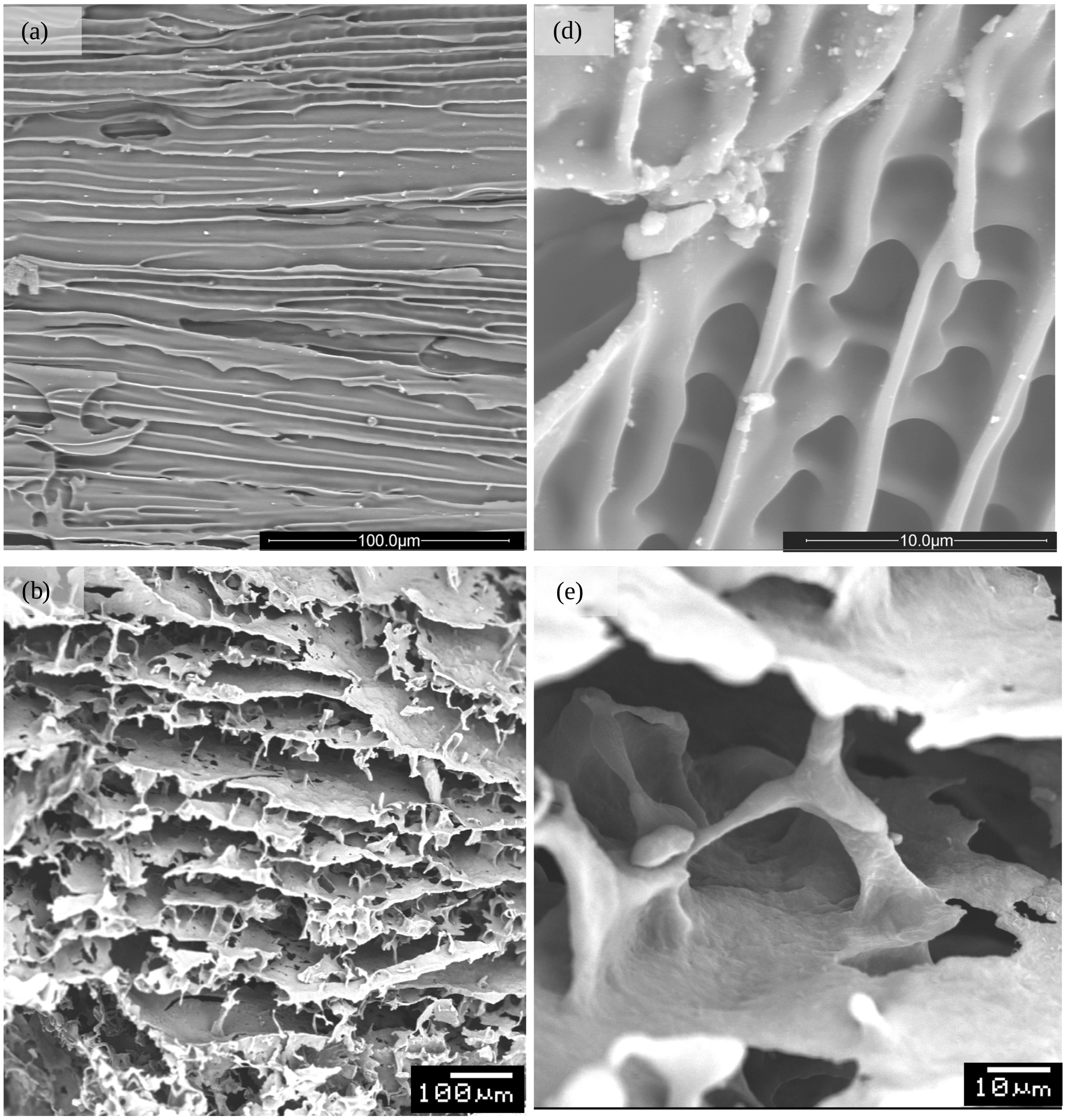

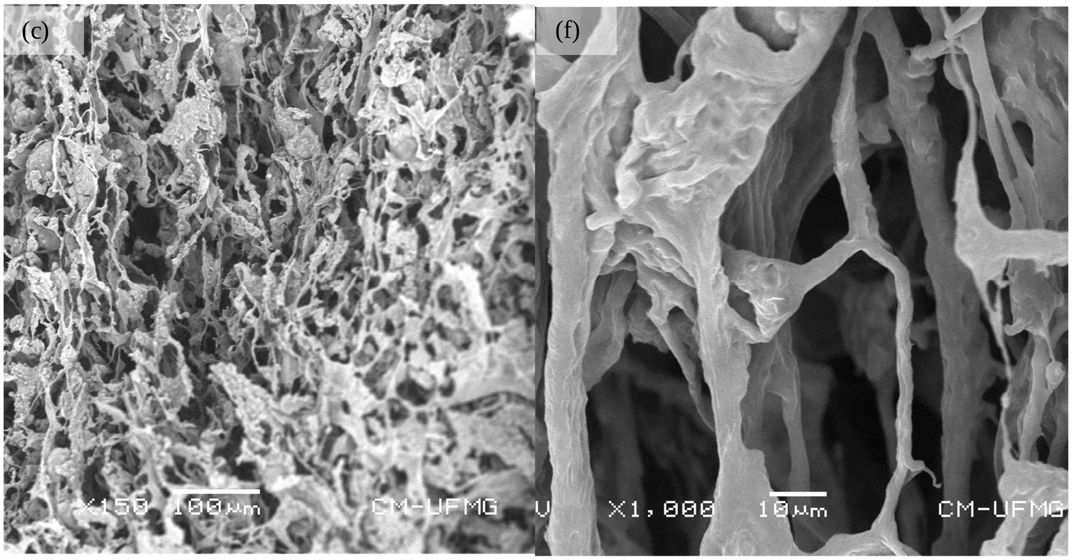

Figure 5.7: SEM images of freeze dried PU foams obtained from dispersions with (a) 20 (b) 10 and (c) 2 % solid content; (d), (e) and (f) are their respective magnifications.

The PU foams produced presented a theoretical density of 1.18 g/cm^3, the estimated bulk density and porosity are showed in Tab. 5.2. The foams produced from more diluted dispersion (2 wt% of solid content) showed an increased porosity so, they were choice as the material more adequate to application as scaffold to tissue engineering. In addition, these samples presented the higher pore size, between 50 to 300 µm (measured by SEM images), that was closer to the size needed to osteoblast adhesion and proliferation (>100 µm) and the mature trabecular bone, whose porosity ranges from 75 to 200 µm [33].

Table 5.2: Properties of PU foams relative to solid content of the dispersions.

Solid %	ρ_s *(g/cm^3)*	ρ_b *(g/cm^3)*	ρ_r	*%Porosity*
20	1.18	0.48	0.40	59
10		0.34	0.29	71
2		0.16	0.21	86

Mechanical tests. Fig. 5.8 shows the tensile and compressive stress–strain curves for the PU films and foams, respectively. The films were flexible and their stress–strain curves are typical non-linear for elastomers without the yield point.

The foams produced are flexible, which makes them easily shaped during surgical implantation and suitable for uses as flexible scaffolds in several tissue engineering applications. Also, the mechanical properties of the scaffolds can be improved when implantaded in the living body from HA layer deposition, resulting in calcification and osteoblast differentiation, colonization and proliferation. As the result, the foams gain strength strength as compared to the foams before implantation. Moreover, the mechanical properties of the scaffold can be improved by using bioactive glass-ceramics as filler to produce PU foams with a composite formulation, as were demonstrated previously [33, 34].

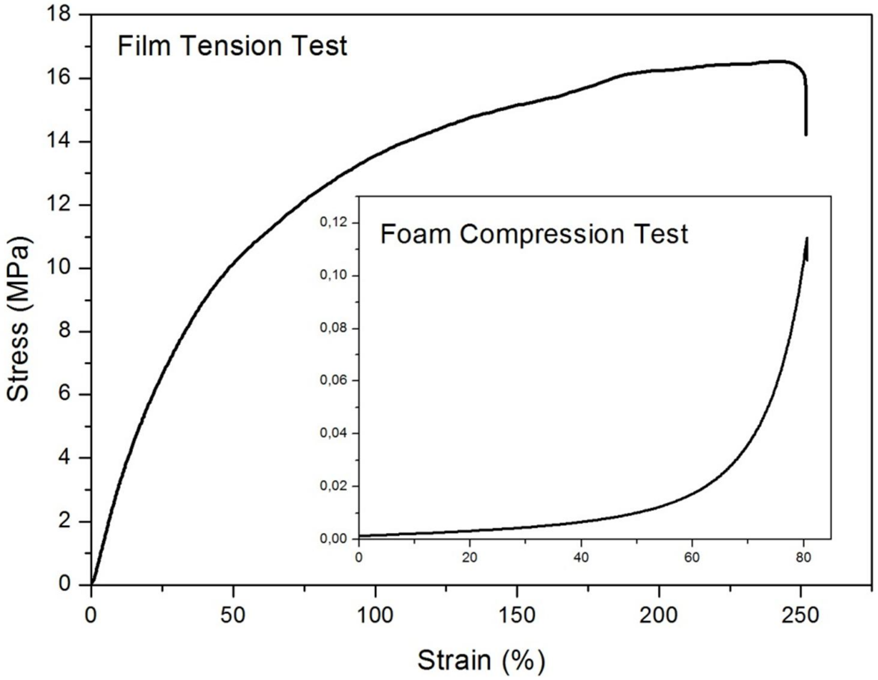

Figure 5.8: Stress–strain curves of PU films and foams.

Accelerated degradation test. Hydrogen peroxide was used to study the PU degradation towards hydrolysis and oxidation reactions. The possible PU degradation mechanisms are discussed below. The three bonds more susceptible to hydrolytic degradation are the ester, urea and urethane (figure 5.9). The ester reverts to the acid and alcohol (Fig. 5.9 (a)). This acid further catalyzes ester hydrolysis. This reaction then becomes autocatalytic. Because of the autocatalytic nature of ester hydrolysis it is the most prevalent. Since the ester bonds are from the PCL chains, the PU SS is degraded from hydrolysis reactions, which explain why PUs become more crystalline and brittle as degradation progress [2]. The urea bond hydrolyzes to a carbamic acid and an amine (Fig. 5.9 (b)). The carbamic acid normally is not stable and typically undergoes further reaction. The urethane, although somewhat less susceptible, undergoes hydrolysis to yield a carbamic acid and an alcohol (Fig. 5.9 (c)). The carbamic acid decomposes to give an amine and carbon dioxide. If the HS is completely degraded, this degradation product is 1,6-hexamethylenediamine, a toxic diamine [1, 22].

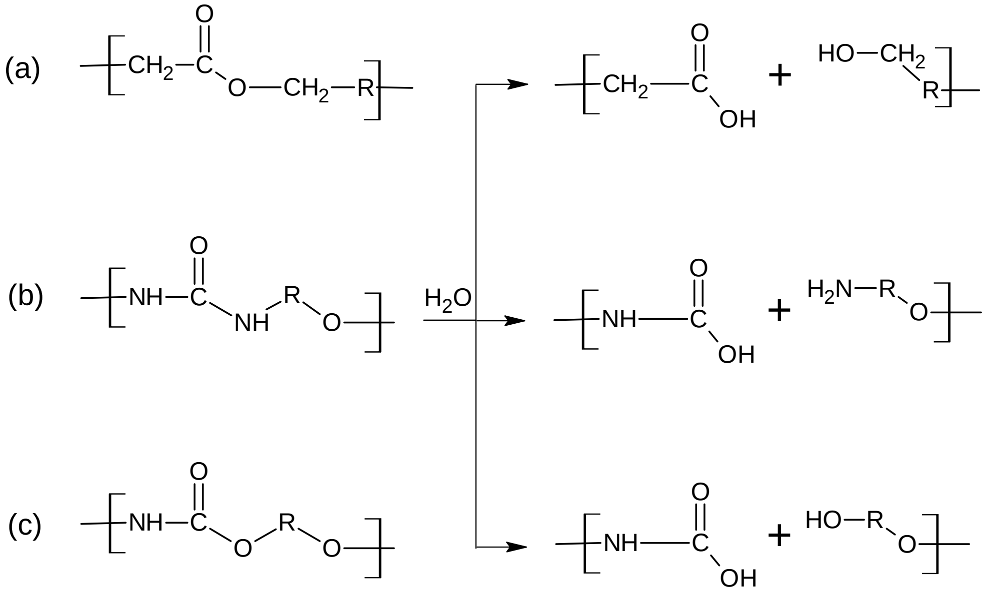

Figure 5.9: Hydrolytic degradation of PU bonds.

The mechanism of peroxide attack is less clear; but studies found that the polyether SS was susceptible to rapid degradation and the HS was attacked in the degradation process [1]. One hypothesis is that the ether is the weak link in oxidation (figure 5.10). Oxidation proceeds via a radical mechanism. The hydroxyl free radical extracts a hydrogen from ether along the PU backbone causing the chain scission (Fig. 5.10 (a)) or cross linking (Fig. 5.10 (b)) structures. The urethane bond can dissociate into the carbamic acid and the carbamic acid decomposes to give a diamine and the polyol (Fig. 5.10 (c)).

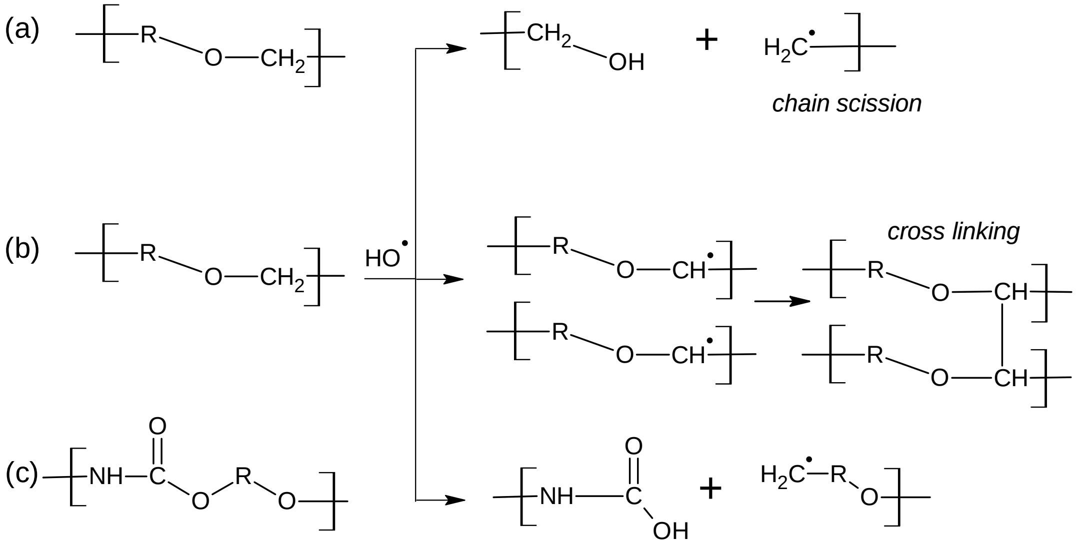

Figure 5.10: Oxidative degradation of PU bonds.

Fig. 5.11 shows the results of MTT assay test for accelerated degradation products of PU. The 30% hydrogen peroxide solution is a medium highly reactive that promotes the degradations of PU SS and HS by hydrolysis and oxidation mechanisms, catalyzed by the temperature of 85°C. After 1 hour of immersion, the PU foams presented mass reduction of (34 ± 6)%, an indicative that PU SS was degraded by hydrolytic reactions. For this incubation period, there was no significant difference in the cell viability of the PU foam and the control, indicating, as expected, that the SS degradation products has no toxic effect. After 24 hours, there were no remaining PU samples visible to the naked eye or caught by 0.45 μm *Milipore* filter, indicating a high level of PU degradation, including the PU HS by oxidation reactions. There was a reduction of 38% in the cell viability of PU foam as compared to control, which, according to the standard, is classified as a moderate toxic effect.

The biological result agrees with the hypothesis that the hard segments of PU were degraded and their degradation products have toxic effects on osteoblast cells. This moderate toxic effect alone is not conclusive as a factor to rule out the PU foams for biodegradable scaffold applications. As the literature has almost no information about degradation products of PU made from HDI, it was not possible to compare the results obtained in the accelerated degradation test with tests performed in conditions similar to *in vivo*. In further studies, it is necessary to determine the PU degradation products and make a study about the release of these products at concentrations closer to the *in vivo* conditions.

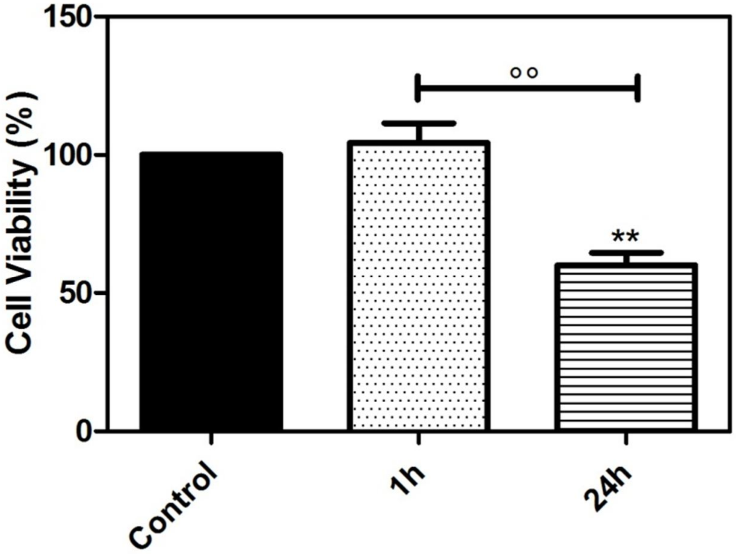

Figure 5.11: Cell viability of PU degradation products in 30% H_2O_2 medium at 85°C by MTT assay. (* Represents significant difference compared to control and ° represents significant difference between different incubation periods at a significance level of 0.05 %)

5.4 Conclusions

Biodegradable polyurethane aqueous dispersions based on PCL polyols, HDI diisocyanate and ATPES were synthesized and cured to form films with tensile strength of 17 MPa, maximum strain of 260% and elastic modulus of 521 MPa. The PU dispersions obtained were freeze dried to form foams with porosity about 80% and pore size range 50 to 300 μm, but low compressive mechanical properties (compressive strength 0.11 MPa, maximum strain 80% and elastic modulus 0.024 MPa). These materials presented mechanical properties can be good enough to support cell growth and proliferation in tissue engineering scaffold but further studies are necessary to evaluate the moderate cytotoxicity presented when the PU was completely degraded.

References

1. Patrick Vermette, Hans J. Griesser, Gaétan Laroche and Robert Guidoin. The tissue engineering intelligence unit 6: biomedical applications of polyurethanes. Landes Bioscience (2001) ISBN: 1-58706-023-X.
2. Tim Thomson. Polyurethanes as specialty chemicals: principles and applications. CRC Press (2005) ISBN: 0-8493-1857-2.
3. J Santerrea, K Woodhouse, G Laroche, RS Labow. Understanding the biodegradation of polyurethanes: From classical implants to tissue engineering materials. Biomaterials 26 (2005) 7457–7470.
4. Shadi Hassan Ajili, Nadereh Golshan Ebrahimi, Masoud Soleimani. Polyurethane/polycaprolactane blend with shape memory effect as a proposed material for cardiovascular implants. Acta Biomaterialia 5 (2009) 1519–1530.
5. Molamma P Prabhakaran1, J Venugopal1, Dan Kai, Seeram Ramakrishna1. Biomimetic material strategies for cardiac tissue engineering. Materials Science & Engineering (2010) Article in Press.
6. JH Ashton, JAM Mertz, JL Harper, MJ Slepian, JL Mills, DV McGrath, JP Vande Geest. Polymeric endoaortic paving: Mechanical, thermoforming, and degradation properties of polycaprolactone/polyurethane blends for cardiovascular applications. Acta Biomaterialia 7 (2011) 287–294.
7. Steven G Wise, Michael J Byrom, Anna Waterhouse, Paul G Bannon, Martin KCN, Anthony S Weiss. A multilayered synthetic human elastin/polycaprolactone hybrid vascular graft with tailored mechanical properties. Acta Biomaterialia 7 (2011) 295–303.
8. Sibylle Grada, Laszlo Kupcsika, Katarzyna Gornab, Sylwester Gogolewskib, Mauro Alinia. The use of biodegradable polyurethane scaffolds for cartilage tissue engineering: potential and limitations. Biomaterials 24 (2003) 5163–5171.
9. Joanne E McBane, Loren A Matheson, Soroor Sharifpoor, J Paul Santerre, Rosalind S Labow. Effect of polyurethane chemistry and protein coating on monocyte differentiation towards a wound healing phenotype macrophage. Biomaterials 30 (2009) 5497–5504.
10. Ian C Bonzani, Raju Adhikari, Shadi Houshyar, Roshan Mayadunne, Pathiraja Gunatillake, Molly M Stevensa. Synthesis of two-component injectable polyurethanes for bone tissue engineering Biomaterials 28 (2007) 423–433.
11. Monika Bil, Joanna Ryszkowska, Piotr Wozniak, Krzysztof J Kurzydłowski, Magorzata Lewandowska-Szumie. Optimization of the structure of polyurethanes for bone tissue engineering applications. Acta Biomaterialia 6 (2010) 2501–2510.
12. Piotr Wozniak, Monika Bil, Joanna Ryszkowska, Piotr Wychowanski, Edyta Wróbel, Anna Ratajska, Grazyna Hoser, Jacek Przybylski, Krzysztof J Kurzydłowski, Magorzata Lewandowska-Szumie. Candidate bone-tissue-engineered product based on human-bone-derived cells and polyurethane scaffold. Acta Biomaterialia 6 (2010) 2484–2493.

13. Scott A Guelcher, Katie M Gallagher, Jonathan E Didier, Derek B Klinedinst, John S Doctor, Aaron S Goldstein, Garth L Wilkes, Eric J Beckman, Jeffrey O Hollinger. Synthesis of biocompatible segmented polyurethanes from aliphatic diisocyanates and diurea diol chain extenders Acta Biomaterialia 1 (2005) 471–484.
14. Danielle N Rockwood, Robert E Akins Jr, Ian C Parrag, Kimberly A Woodhouse, John F Rabolt. Culture on electrospun polyurethane scaffolds decreases atrial natriuretic peptide expression by cardiomyocytes in vitro Biomaterials 29 (2008) 4783–4791.
15. M Zanetta, N Quirici, F Demarosi, MC Tanzi, L Rimondini, S Fare. Ability of polyurethane foams to support cell proliferation and the differentiation of MSCs into osteoblasts. Acta Biomaterialia 5 (2009) 1126–1136.
16. Rui Chena, Chen Huanga, Qinfei Kea, Chuanglong Heb, Hongsheng Wangb, Xiumei Mob. Preparation and characterization of coaxial electrospun thermoplastic polyurethane/collagen compound nanofibers for tissue engineering applications Colloids and Surfaces B: Biointerfaces 79 (2010) 315–325.
17. Milena Spírková, Jelena Pavlicević, Adam Strachota, Rafal Poreba, Oskar Bera, Ludmila Kaprálková, Josef Baldrian, Miroslav Slouf, Nada Lazić, Jaroslava Budinski-Simendić. Novel polycarbonate–based polyurethane elastomers: composition – property relationship European Polymer Journal (2010) Article in Press.
18. Ji Hye Hong, Hyun Jeong Jeon, Jae Heung Yoo, Woong-Ryeol Yu, Ji Ho Youk. Synthesis and characterization of biodegradable poly(3-caprolactone-co-b-butyrolactone)-based polyurethane. Polymer Degradation and Stability 92 (2007) 1186-1192.
19. Lisa Tatai, Tim G. Moore, Raju Adhikari, Franc-ois Malherbe, Ranjith Jayasekara, Ian Griffiths, Pathiraja A. Gunatillak. Thermoplastic biodegradable polyurethanes: The effect of chain extender structure on properties and in-vitro degradation. Biomaterials 28 (2007) 5407–5417.
20. Zhigang Xie, Changhai Lu, Xuesi Chen, Li Chen, Xiuli Hu, Quan Shi, Xiabin Jing. A facile approach to biodegradable poly(e-caprolactone)-poly(ethylene glycol)-based polyurethanes containing pendant amino groups. European Polymer Journal 43 (2007) 2080–2087.
21. C. Mauli Agrawal, Jack E. Parr, Steve T. Lin. Synthetic bioabsorbable polymers for implants. ASTM STP 1396 Library of Congress Catalogin in Publication Data (1999) 39-57.
22. T. Thomson. Design and Application of Hydrophilic Polyurethanes – Medical, Agriculture and Other Applications. CRC Press (2000) ISBN-10: 1566768950
23. Eliane Ayres, Rodrigo L. Oréfice, M. Irene Yoshida. Phase morphology of hydrolysable polyurethanes derived from aqueous dispersions. European Polymer Journal 43 (2007) 3510–3521.
24. Gisele Rodrigues da Silva, Armando da Silva-Cunha Jr., Francine Behar-Cohen, Eliane Ayres, Rodrigo L. Oréfice. Biodegradation of polyurethanes and nanocomposites to non-cytotoxic degradation products. Polymer Degradation and Stability 95 (2010) 491-499.

25. A. Anand Prabu, M. Alagar. Mechanical and thermal studies of intercross-linked networks based on siliconized polyurethane-epoxy/unsaturated polyester coatings. Progress in Organic Coatings 49 (2004) 236–243.
26. Qiu Gen Zhang, Qing Lin Liu , Zhong Ying Jiang, Li Yi Ye, Xiu Hua Zhang. Effects of annealing on the physico-chemical structure and permeation performance of novel hybrid membranes of poly(vinyl alcohol)/c-aminopropyl-triethoxysilane. Microporous and Mesoporous Materials 110 (2008) 379–391.
27. D.K. Chattopadhyay, K.V.S.N. Raju. Structural engineering of polyurethane coatings for high performance applications. Prog. Polym. Sci. 32 (2007) 352–418.
28. H. Sardon, L. Irusta, M.J. Fernández-Berridi, M. Lansalot, E. Bourgeat-Lami. Synthesis of room temperature self-curable waterborne hybrid polyurethanes functionalized with (3-aminopropyl)triethoxysilane (APTES). Polymer 51 (2010) 5051-5057.
29. Linda G. T. Gaines, Kenneth W. Fent, Sheila L. Flack, Jennifer M. Thomasen, Louise M. Ball, David B. Richardson, Kai Ding, Stephen G. Whittaker and Leena A. Nylander-French. Urine 1,6-hexamethylene diamine (HDA) levels among workers exposed to 1,6-hexamethylene diisocyanate (HDI). Ann. Occup. Hyg. (2010) 54 (6): 678–691.
30. Roger Brown. Handbook of polymer testing: short-term mechanical tests. Rapra Technology (2002) ISBN: 1-85957-324-X.
31. Seema Agarwal, Christian Speyerer. Degradable blends of semi-crystalline and amorphous branched poly(caprolactone): Effect of microstructure on blend properties. Polymer 51 (2010) 1024–1032
32. Hongdan Peng, Yu Han, Tianxi Liu, Wuiwui Chauhari Tjiu, Chaobin He. Morphology and thermal degradation behavior of highly exfoliated CoAl-layered double hydroxide/polycaprolactone nanocomposites prepared by simple solution intercalation Thermochimica Acta 502 (2010) 1–7
33. Jeffrey O. Hollinger Thomas A. Einhorn, Bruce A. Doll and Charles Sfeir. Bone tissue engineering. CRC Press (2000) ISBN: 0-8493-1621-9.
34. M. Zanetta, N. Quirici, F. Demarosi, M.C. Tanzi, L. Rimondini, S. Fare. Ability of polyurethane foams to support cell proliferation and the differentiation of MSCs into osteoblastos. Acta Biomaterialia 5 (2009) 1126–1136.

6 Film and foam composites of biodegradable polyurethane and bioactive glass nanoparticles

Abstract. *The development of polymer/bioactive glass has been recognized as a strategy to improve the mechanical behavior of bioactive glass-based materials. Several studies have reported systems based on bioactive glass/ biopolymer composites. In this work we developed a composite system based on bioactive glass nanoparticles (BGNP), obtained by a modified Stober method. The BGNP presented significant increase in cell viability when compared to microparticles. The polymeric phase is extremely important to design the final properties of the composites. The highly variable synthesis chemistry of segmented PU's may be exploited to generate polymers having properties ranging from very soft elastomers to very rigid plastics. In addition to the physical properties, a great care has to be taken in the choice of the building blocks. Their degradation products have to be biocompatible, non-toxic and metabolized or eliminated by the living organism. We developed a new chemical route to obtain aqueous dispersive biodegradable polyurethane. This chemical procedure was well succeeded in producing PU dispersions with solid content about 20%. We then associated the newly developed components (BGNP and PU aqueous dispersions) to produce membranes and scaffolds, intending to associate biocompatibility, mechanical and physical properties in a material designed for tissue engineering applications. The composites were obtained by the dispersion of BGNP in a PVA solution, with contents of 0, 10 and 25 wt% BGNP, and subsequently mixing to the PU dispersion. Films were obtained by casting the dispersions in molds. Porous scaffolds were produced by dilution and freeze drying of the dispersion prepared. The composites obtained were characterized by FTIR, XRD, MEV, EDS and biological and mechanical tests. The films presented 350% of deformation and the foams presented mechanical properties adequate for tissue engineering applications. The materials presented good cell viability and hydroxyapatite layer formation upon immersion in simulated body fluid.*

6.1 Introduction

Bioactive glasses (BGs) have good biological characteristics that indicate it as a promising material for bone tissue engineering. When implanted in the body, they induce an interfacial bioactive answer [1-10]. Furthermore, the dissolution products of bioactive glass exert control over genetic factors of bone growth [1, 2, 6-8]. Various investigations regarding sol–gel derived BG have been published including bulk and powder bioactive glasses [11– 18] and porous bioactive glass scaffolds [19-30]. However, compared with natural bone tissue, bioactive glasses especially processed as foams, exhibit lower mechanical properties. In particular, the low fracture toughness limits the application of bioactive glasses as scaffold structures in load-bearing situations. General values of mechanical properties for bulk bioactive glass materials were summarized by Rezwan et al. [31].

The development of polymer/bioactive glass has been recognized as a strategy to improve the mechanical behavior of bioactive glass-based materials [32]. Compared with microsized bioactive ceramic particles, nanosized particles have a large surface area and can form a tighter interface with polymer matrix in composites, and hence, a high performance in mechanical properties can be expected [33]. Furthermore, studies reported that nanoscaled biomaterials exhibited an enhanced biocompatibility [34, 35] and have also revealed that reducing particles size to nanoscale could stimulate their bioactivity [36]. In this context, several studies have been reporting systems based on nanoestructured bioceramics/ biopolymer composites [37-52]. Studies showed that increasing specific surface area and pore volume of bioactive glass may greatly accelerate the deposition process of hydroxyapatite (HA) [36].

BG nanopowders were prepared by controlling the concentration of the reagents, catalyst, alcohol medium and pH, mediated sol–gel process used in W/O emulsions and coprecipitation method [53-60]. To maintain the stability of the particles, because of the spherical shape, various studies focused on the surface modification of Stober SiO_2 nanoparticles to create a bioactive material with dispersion capability [61-67]. The synthesis consists in the hydrolysis under aqueous alcohol solutions of silicon alkoxides in the presence of ammonia as a catalyst. Silicic acid is produced during hydrolysis and when its concentration is above its solubility in alcohol, it nucleates homogeneously and forms particles of submicron size [61-67].

As described in chapter 4, the ternary SiO_2-CaO-P_2O_5 BGNP system, with spherical shape and controlled particle size of (87 ± 5) nm, was successfully obtained by modified Stöber method. The nanoparticles presented high specific surface area (534 m^2/g) and pore volume (1.11 cm^2/g). Besides they presented good dispersability on polar solvents, which enable their use in composites. Also, as presented in chapter 5, the NPs show a considerable increase in cell viability as compared to microparticles (50% higher). These results suggest that BGNP could offer superior performance for developing bioactive material composites in comparison to the bioactive glass microparticles.

Polyurethanes (PU's) and their nanomposites have been designed for biomedical applications such as: soft tissue engineering [68], cardiac tissues [69], materials for use in contact with the blood [70], implants for the meniscus knee [71] and controlled release of drugs [72]. Biodegradable PU's developed by Ayres [73, 74] can be modified to produce composites based on PU matrix and bioactive glass nanoparticles, that are both bioactive and with mechanical behavior more adequate for bone tissue engineering applications. The synthesis consists in the prepolymer mixing process, where the macrodiol components - polycaprolactone-diol (PCL) 1250 and 2000 g/mol - 2,2-bis(hydroxymethyl) propionic acid (DMPA) and isophorone diisocyanate (IPDI), with NCO/OH ratio of 2.3, were added to the reactor in the presence of dibutyl tin dilaurate (DBDLT) and the reaction was carried out at 70 - 75°C under nitrogen atmosphere for 4 hours. The amount of free NCO groups on a percentage basis was determined by the standard di-butyl amine back titration method. After titration, the prepolymer temperature was allowed to drop to 40°C. The carboxylic acid groups were neutralized by the addition of triethylamine (TEA). The mixture was stirred for further 40 min to ensure the reaction was completed. The PU dispersion occurred by adding deionized water to the neutralized prepolymer which was stirred vigorously. After the dispersion, an amount of hydrazine enough to react with free NCO groups was added to the reactor with a small amount of water, and stirring was continued for further 30 min. This chemical procedure was well succeeded in producing PU dispersions with solid content about 25%. Films were produced by casting the dispersions in a Teflon mold and allowing them to dry at room temperature for one week. Afterwards the films were placed in an oven at 60°C for 24 h for drying [73].

The chains of the PU's can be extended by silane groups by the reaction of the prepolymer with amino silanes as APTES (3-aminopropyltriethoxysilane). Silanized polyurethane dispersions are generally composed of polyurethane backbones containing condensable terminal groups. During the water evaporation, these groups can undergo crosslinking reactions to form a stable siloxane linked network, which results in the improvement of the properties of the pure polyurethane. In addition, the incorporation of small inorganic domains in the nanoscale range gives rise to a synergetic combination of the properties of each of the constituents [75-79]. Hydrolyzed silane groups, like TMOS, TEOS and TEP, can be added to the PU by condensed reactions with animo silanes groups to promote the adhesion of the PU with inorganic particles [75].

In chapter 6, it was proposed to use the Ayres route [73, 74] to obtain PU prepolymer, with some modifications in the synthesis. Biodegradable polyurethane aqueous dispersions based on PCL polyols, HDI diisocyanate and ATPES were successfully synthesized and cured to form films with tensile strength of 17 MPa, maximum strain of 260 % and elastic modulus of 521 MPa. PU dispersions obtained were freeze dried to form foams with porosity about 80% and pore size range 50 to 300 μm, with mechanical properties adequate to support cell growth and proliferation in tissue engineering scaffold.

In this work, it was proposed to use the polyurethane in association with the bioactive glass nanoparticles to obtain PU/BGNP composites with 10 and 25 wt% of BGNP, as film and foams. The aim of the study is the development of materials intending to associate biocompatibility, mechanical and physical properties in a material designed for tissue engineering applications.

6.2 Materials and Methods

Synthesis of Bioactive Glass Nanoparticles (BGNP). 200 ml of methanol was mixed with 0.46 ml of ammonium hydroxide 33% and 0.51 ml of water and stirred for 5 min. Then 5.57 ml TEOS and 0.56 ml TEP were added dropwise for 10 min. The sol was mechanic stirred for 48 h. The formed sol was placed in an oven at 50 °C until the complete ammonium evaporation (about 3 h). Then, it was filtered in a 0.22 μm *Milipore*. 3.46 g $Ca(NO_3)_2.4H_2O$ was dissolved in the sol and mixed for 24 h. The nanoparticles formed were separated under 0.11 μm by subsequently filtrations in a 0.22 and 0.11 μm *Milipore*. Freeze drying was used to prevent the secondary aggregation of gel particle via the linkage of water molecules during the drying process [80]. The powder obtained was submitted to thermal treatment at 200ºC for 40 min, with heating rate of 1ºC/min. At the end of the process, a well dispersed bioactive glass nanoparticle powder with average diameter of 87 nm was obtained without grinding and sieving.

Synthesis of biodegradable polyurethanes. Aqueous polyurethane dispersions were prepared by the prepolymer process, using a 250 mL three-neck glass flask equipped with a heating mantel and a mechanical stirrer. Then, this prepolymer was added to an aqueous premix to form the dispersion. The macrodiol components polycaprolactone-diol Mn 1250 g/ mol (PCL 1250), polycaprolactone-diol Mn 2000 g/ mol (PCL 2000), both by *Sigma-Aldrich*, and 2,2-bis(hydroxymethyl) propionic acid 98.3% (BMPA), by *Fluka*, were added to the reactor without any catalyst. The temperature was kept at 60°C. 30 minutes after PCLs melting, hexamethylene diisocyanate (HDI), by *Sigma-Aldrich*, was added and the reaction was carried out at 80 °C under nitrogen atmosphere for 2.5 h. The premix was prepared by the addition of triethylamine (TEA) by and 24% hidrazine solution (HZ), both by *Miracema Nuodex Brazil*, and (3-aminopropyl) triethoxysilane (ATPES), by *Sigma-Aldrich*, were mixed in water for 30 min. The PU dispersion, with solid content about 20 %, occurred by the addition of prepolymer in the premix which was stirred vigorously until a milk dispersion was observed. The composition of the PU prepared is shown in chapter 6.

Composites production. The composites were obtained by the dispersion of BGNP in a 20 wt% PVA solution. Then, this mixture was added to the PU dispersion, previously prepared, with final BGNP composition of 0, 10 and 25 wt%. The composition of the polymer blend was maintained at 70% PU and 30% PVA, in weight. PVA solution was used because BGNP dispersed very well in this medium while in aqueous PU, less than 1 wt% could be dispersed without phase separation. The composition 70 PU/ 30 PVA wt% resulted in more flexible films than others fractions tested (1, 5, 15, 30 and 50% of PVA). Films were produced by casting the dispersions in acrylic plates and allowing them to dry at room temperature for one week. Afterwards the films were placed in an oven at 60 °C for 72 h for heat treatment. In chapter 6, it was showed that the PU porous scaffolds obtained from more diluted dispersion (2% solid content) showed an increased porosity and presented macroporous in the renge size adequaded to osteoblast adhesion and proliferation so, they were choice as the material more adequate to application as scaffold to tissue engineering. For the composite foams, the dispersions were also diluted at 2 wt% and placed in cylindrical Teflon molds and freeze dried. Then, the produced foams were submitted to the same heat treatment as the films.

The insertion of BGNP in the polymer matrix can result in a strong interaction between the PU and PVA phases. As the PU (Fig. 6.1 (a)) is terminated by silane groups, the *–OH* groups of BGNP (Fig. 6.1 (b)) can react with these terminations resulting covalent bones *Si-O-Si*. There is the same possibility with the PVA chains (Fig. 6.1 (c)), which have *–OH* groups avaliable for condensation reactions. There is also the possibility of the formation of hydrogen bonds between these structures.

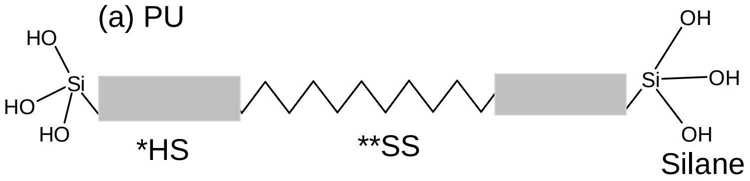

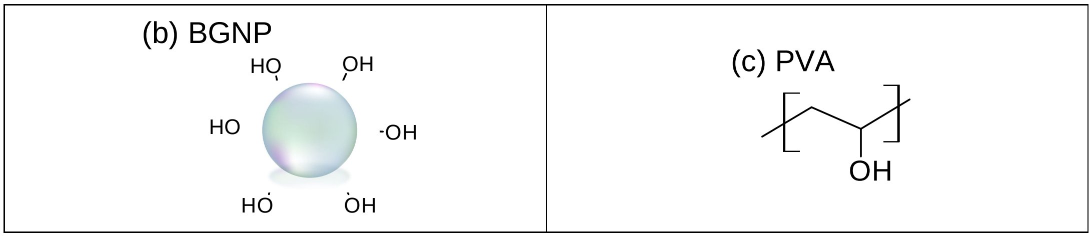

Figure 6.1: Schematic structure of the composite phases. *Hard segment and **Soft segment of PU.

Materials characterization. The structure of the composite films was analyzed by Perkin Elmer 100 Spectrum Fourier transform infrared (FTIR). Spectra were collected in the mid-infrared range from 550 to 4000 cm^{-1} in μATR mode. X-ray Diffraction (XRD) spectra of the films were collected on a Philips PW1700 series automated powder diffractometer using Cu Kα radiation at 40 KV/40 mA. Data was collected between 4.05 and 89.95° with a step of 0.06° and a dwell time of 1.5 second. Morphologies and chemical composition of the composite films and foams were observed by Scanning Electron Microscope (SEM) Tecnai G220 FEI equipped with energy-dispersive x-ray spectroscopy (EDS).

The percentage porosity was calculated using eq. 6.1:

$$\% Porosity = 1 - \rho_r \qquad \text{Eq. 6.1}$$

where ρ_r is the relative density (Eq.6.2):

$$\rho_r = \frac{\rho_b}{\rho_s} \qquad \text{Eq.6.2}$$

where ρ_b is the geometrical bulk density, calculated from the ratio of mass by volume of the cylindrical foams, and ρ_s is the skeletal density, which was estimated by the density of the films.

Mechanical tests of the materials were performed on an EMIC-DL300 universal testing machine at ambient temperature. 50 N load cell and minimum of 5 test pieces were used in each test. The tensile tests of the films were based on ASTM D 638-10 (*Standard Test Method for Tensile Properties of Plastics*) using type IV for the die shape (thickness 0.15 mm) and a crosshead speed of 20 mm/min. Compressive tests of the foams were performed according to ASTM D 695 (*Standard Test Method for Compressive Properties of Rigid Plastics*). Foams with cylindrical shape (diameter 10 mm and length 14 mm), were tested at speed of 5 mm/min.

***In vitro* bioactivity test.** The formation of a HA layer *in vitro* on a material surface is believed to indicate its bioactive potential *in vivo* [1-10]. Simulated body fluid (SBF) was prepared by dissolving NaCl 7.995 g, $NaHCO_3$ 0.353 g, KCl 0.224 g, $K_2HPO_4 \cdot 3H_2O$ 0.228 g, $MgCl_2 \cdot 6H_2O$ 0.305 g, $CaCl_2$ 0.227 g, and Na_2SO_4 0.071 g, all *Synth Brasil*, into distilled water. The solution was buffered at pH 7.4 by adjusting the volume amount of Tris (tris-hydroxymethylaminomethane) and HCl at 36.5 °C. The formation of HA layer on the surface of obtained films was evaluated after soaking the samples in SBF solution for 7 days. Surface structural observation was carried out by SEM and EDS after the immersed samples were removed from the SBF, washed three times with de-ionized water and dried at air circulation drying oven.

Degradation study. An accelerated degradation test was used to evaluate the composites degradation. Foam samples were immersed in 30 % hydrogen peroxide solution, with weight-to-solution volume ratio of 0.1 mg/ml, and incubated for 1 and 24 hours at temperature of 85 °C [82]. After 24 hours, the foam could not be seen with the naked eye, indicating high level of degradation. The cytotoxicity of the degradation products was evaluated by the direct contact test, performed according to ISO 10993 (*Part 5 - tests for in vitro cytotoxicity*).

Primary osteoblasts cells were pre-cultured for 24 h in Dulbecco’s Modified Essential Medium (DMEM) supplemented with bovine serum (10%) in 24-well plates. The degradation product was mixed in the medium without any filtration, with volume ratio of 0.1 ml/ml, and soaked for 5 min. The mixture was placed directly over the culture on the plates and maintained under CO_2 atmosphere for 24 h. It was used phosphate-buffered saline (PBS) as positive control and polyethylene as negative control. After 24 h of incubation in the presence of the degradation product, osteoblast viability was evaluated based on the reduction of tetrazolium salt to formazan crystals by living cells. About 60 ml of MTT (5 mg/ml) was added to each well. Two hours later, the cell morphology was analyzed by inverted optical microscopy and formazan salts were dissolved with Sodium dodecyl sulfate (SDS) 10% HCl and propidium iodide (*American Bioanalytical, Natik, USA*). After incubation for 18 h the optical density measurement was done at 595 nm. The morphological changes indicating cytotoxicity and cell growth characteristics were recorded using a microscope. The experiments were performed with n=8 ($p< 0.05$ statistical analysis: One way /ANOVA / Bonferroni / GraphPad Prism.

6.3 Results and discussions

Structural characterization. The analysis of PU [82-103] and BG [104-115] structures by infrared spectroscopy (FTIR) has been reported by several research groups in literature, which were used as reference.

Fig. 6.2 shows the FTIR spectra of composites obtained. Fig. 6.3 shows a magnification of the FTIR spectra. The band between 3600 and 3100 cm^{-1} is the contribution of the stretching vibrations of several hydrogen–bonded *N–H* and *O–H* groups of PU, PVA and BGNP materials. The bands at 2940 and 2860 cm^{-1} are assigned, respectively, to *C-H* asymmetric and symmetric stretching in $–CH_2–$ groups of the polymer materials. The bands between 1740 and 1560 cm^{-1} are composed by the overlap of the bands at 1730, 1670 and 1610 cm^{-1}, related to *C=O* stretching vibration in urethane, urea and hydrogen bonded urethane structures; and 1640-1540 cm^{-1}, related to H bending vibration in secondary amide in the urethane bond. 1460 and 1456 and 1370 cm^{-1} bands are assigned to *C–H* bending and wagging, respectively, deformations in $–CH_2–$ groups. The band at 1240-1256 cm^{-1} is related to *C–N* stretching vibration mode in the *R-NH-COO-* group. 1160 cm^{-1} band is assigned to *C–O–C* stretching vibration modes. The band at 778 cm^{-1}

is related to stretching vibration mode *C-O* in the *CO-O-C* groups in poly(ester urethanes).

The incorporation of alkoxide silane in PU is manifested by the bands at 1200 and 1090 cm^{-1}, associated with LO and TO vibration modes, respectively, of *Si–O* bond. The bands at 1100 and 1040 cm^{-1} are assigned to *Si–O* stretching vibration modes. The bands at 1300-1340 and 820 cm^{-1} are assigned, respectively, to asymmetric and symmetric stretching vibrations of Si–O–Si groups. It is hard to evidence the presence of BGNP on the structure of the composites by FTIR analysis because the PU prepared in this work also have Si-O groups in its structure, due to the addition of amino silane during synthesis. However, there is a little increase of intensity in the bands at 1100 and 820 cm^{-1} with the increase of BG in the polymer blend, which can be attributed to the nanoparticles incorporation.

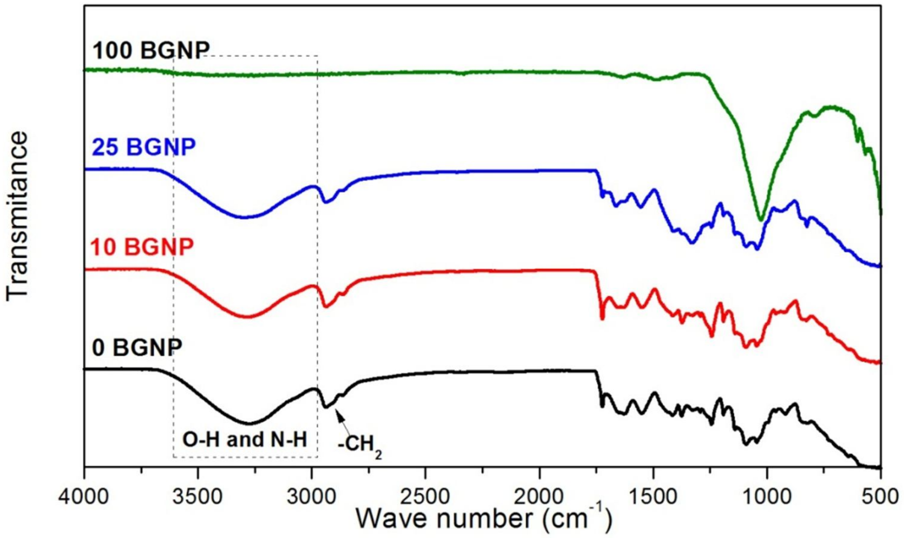

Figure 6.2: FTIR spectra of film materials obtained. 0 BGNP represents the PU/PVA blend, 10 and 25 BGNP are the composites with 10 and 25 wt% of BGNP, respectively, and 100 BGNP is the spectrum of the nanoparticles obtained

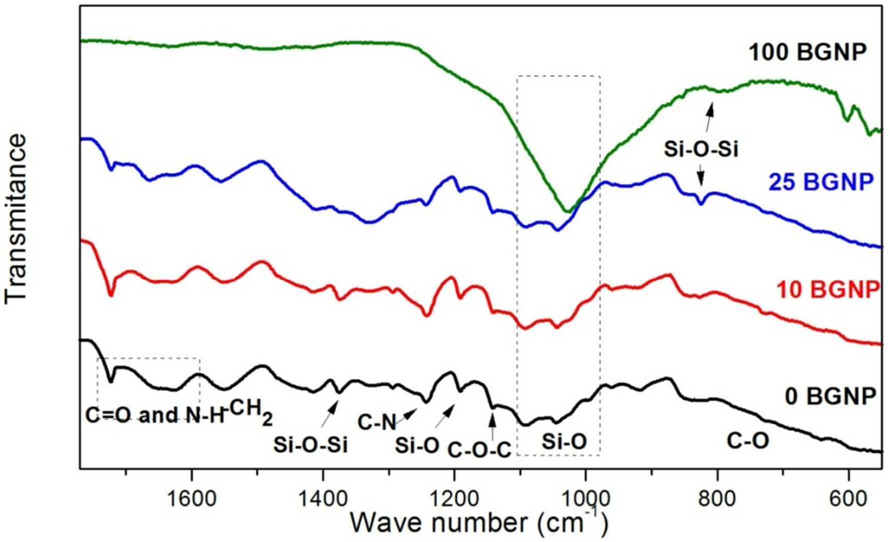

Figure 6.3: Magnification of FTIR spectra. 0 BGNP represents the PU/PVA blend, 10 and 25 BGNP are the composites with 10 and 25 wt% of BGNP, respectively, and 100 BGNP is the spectrum of the nanoparticles obtained.

The XRD patterns of composite films are shown in Fig. 6.4. PVA is well known as a crystalline polymer, and the diffraction peaks at 2θ 11.4, 19.4 and 40.4° correspond to the PVA crystalline phase [110-112]. The diffraction of PVA crystal results from the strong intermolecular interaction between PVA chains through the intermolecular hydrogen bonding. The intensity of the diffraction peaks and also the size of the crystals are determined by the number of PVA chains packing together. Two distinct diffraction peaks are observed at 2θ at 21.3◦ and 23.8°, which were indexed as (110) and (200) planes, respectively, of an orthorhombic crystalline structure of PCL in PU chains [31, 32].

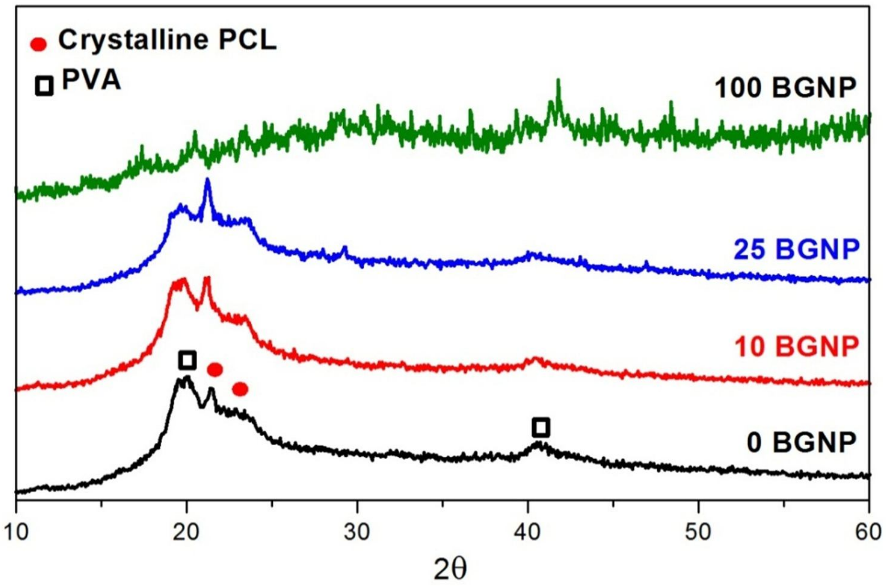

Figure 6.4: XDR pattern of film materials obtained. 0 BGNP represents the PU/PVA blend, 10 and 25 BGNP are the composites with 10 and 25 wt% of BGNP, respectively, and 100 BGNP is the spectrum of the nanoparticles obtained

Fig. 6.5 shows a schematic representation of the interactions between PU/PVA blend and bioactive glass nanoparticles. The intensity of PVA diffraction peaks decreased with the increase of BGNP fraction in the composites. This can be attributed to the fact that the interactions of PVA with nanoparticles and PU chains lead to a decrease in the intermolecular interaction between the PVA chains and thus decrease the degree of crystallinity. It is believed that the organization of PVA chains is restructured to a more amorphous configuration due to the interaction with the other phases present. The same behavior was not seen when the PU crystallinity in composites was analyzed in the XDR patterns. The intensity of crystalline PCL diffraction peak do not decrease with increase of BGNP content in the composite, which suggests a smaller interaction between the PU crystalline phase and the nanoparticles. This may occur because the PU chains do not interact significantly with the nanoparticles, which means that NPs are dispersed mostly in PVA chains. Another hypothesis is that the nanoparticles interacted preferentially with the amorphous phase of PU and are dispersed in both amorphous PU and PVA phases. As it was observed visually that the BGNPs are more dispersible in

PVA solution than PU dispersion, it is reasonable to assume that the first hypothesis occurred predominantly when the polymer blend is mixed with nanoparticles.

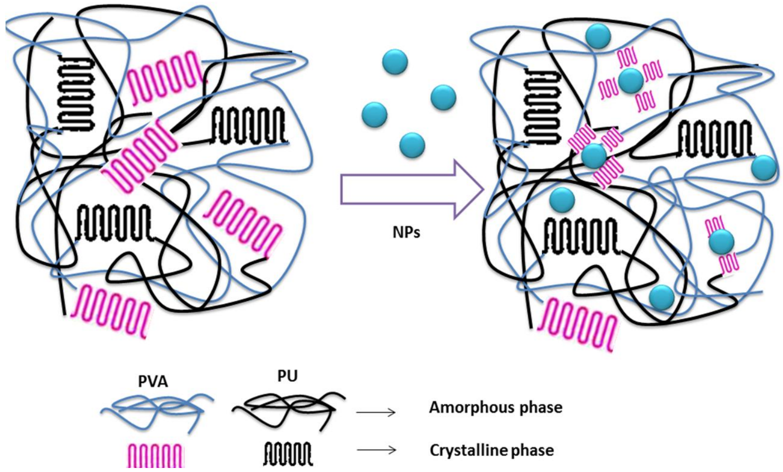

Figure 6.5: Schematic representation of the interactions occurred between PU/PVA blend and BGNP in composites obtained.

The decrease in composite crystallinity also explains the macroscopic changes observed in transparency of the films. Amorphous polymers provide transparency while crystalline polymers cause refraction of light ray and results in opaque materials, particularly in thicker products. Crystalline polymers become transparent as the size of crystals becomes smaller, because smaller crystals do not cause refraction of light [111-113]. The films, obtained with the same thickness, become more translucid with the increase of BGNP fraction, as shown in Fig.6.6.

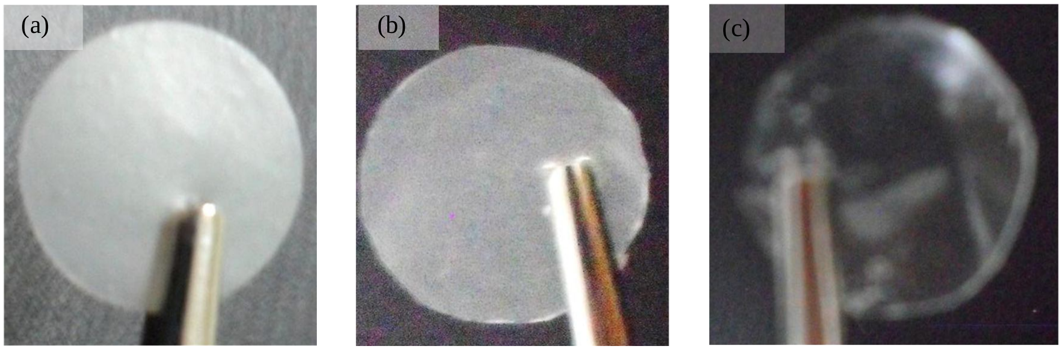

Figure 6.6: Digital image of films obtained with the same thickness. (a) PU/PVA blend, composites PU/PVA with (b) 10 and (c) 25% of BGNP.

The pore structure of the foams obtained by freeze drying the composite dispersions with solid content of 2 wt % was evaluated by SEM (Fig. 6.7). The pore size range of the foams showed a little difference between the composites with 10% of BGNP (30 to 200 μm) and the polymer blend (50 to 250 μm), but composites with 25% of BGNP presented pore size range significantly lower (5 to 50 μm). The composites with 10% of BGNP presented pore size range closer to the size needed for osteoblast adhesion and proliferation (>100 μm) [115], and also have bioactive potential because of the high fraction of BGNP.

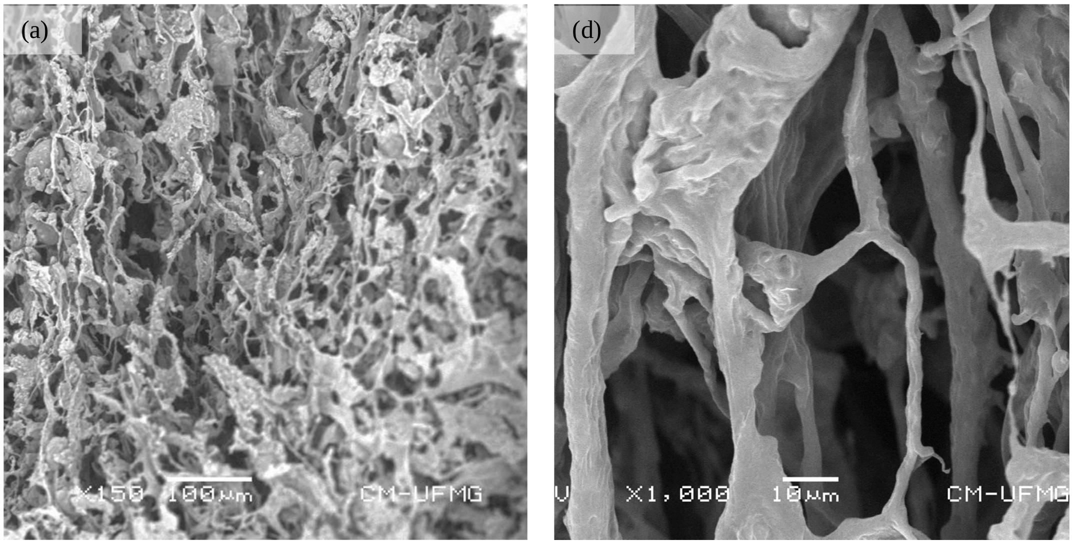

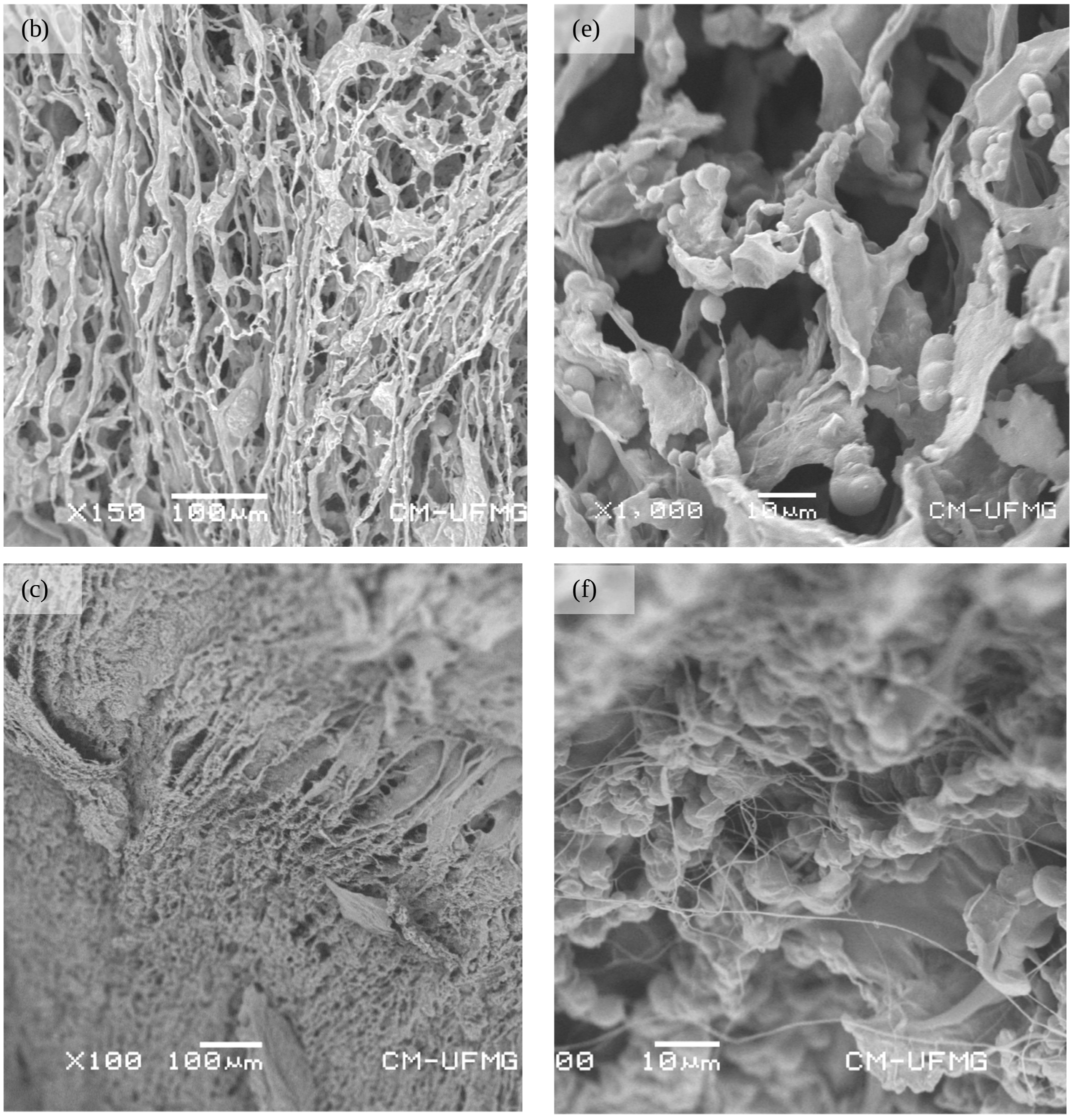

Figure 6.7: SEM images of freeze dried foams obtained from dispersions of PU/ PVA blends with (a) 0 (b) 10 and (c) 25 % of BGNP; (d), (e) and (f) are their respective magnifications.

The EDS obtained for general SEM areas of the foam samples (Fig. 6.7) are shown in Fig. 6.8. The Si inorganic part of the polymer blend, incorporated by the alkoxide silane, is evidenced in Fig. 6.8 (a). Si peaks are also observed in the composite spectra. The incorporation of BGNP in the composites can be seen by the presence of calcium in the spectrum of the composites with 10 (Fig. 6.8 (b)) and 25% (Fig. 6.8 (c)) of BGNP.

The phosphorous present in the BGNP do not appear in EDS spectra, probably due to their low concentration in the composite.

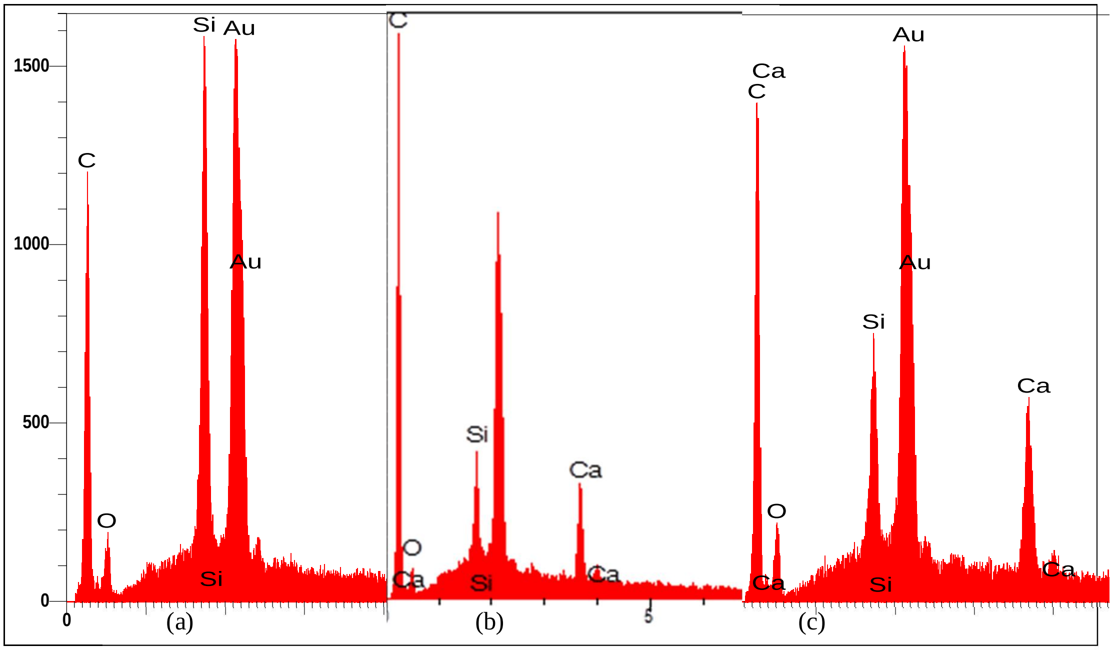

Figure 6.8: EDS of composites (a) 0, (b) 10 and (c) 25 wt% of BGNP.

The estimated densities and porosity of the foam composites are shown in Tab. 6.1. The foams obtained from PU/PVA blend and their composite with 10% BGNP presented significantly higher porosity than foams produced with 25% of BGNP. This result indicates that the incorporation of 10% BGNP in polymer chains do not decrease significantly the foam porosity, which means that this composite has the high porosity and macropore size adequate for tissue engineering applications [115].

Table 6.1: Skeletal and bulk densities and porosity of composite foams obtained.

% BGNP	*ρ_s (g/cm^3)*	*ρ_b (g/cm^3)*	*ρ_r*	*% Porosity*
0	1.18 ± 0.03	0.23± 0.06	0.20	81
10	1.23± 0.05	0.29± 0.05	0.24	76
25	1.38± 0.05	0.86 ± 0.08	0.62	38

Mechanical tests. Figures 6.9 and 6.10 show the tensile and compressive stress–strain curves for the composite films and foams, respectively. The films showed flexible behavior (Fig. 6.9).

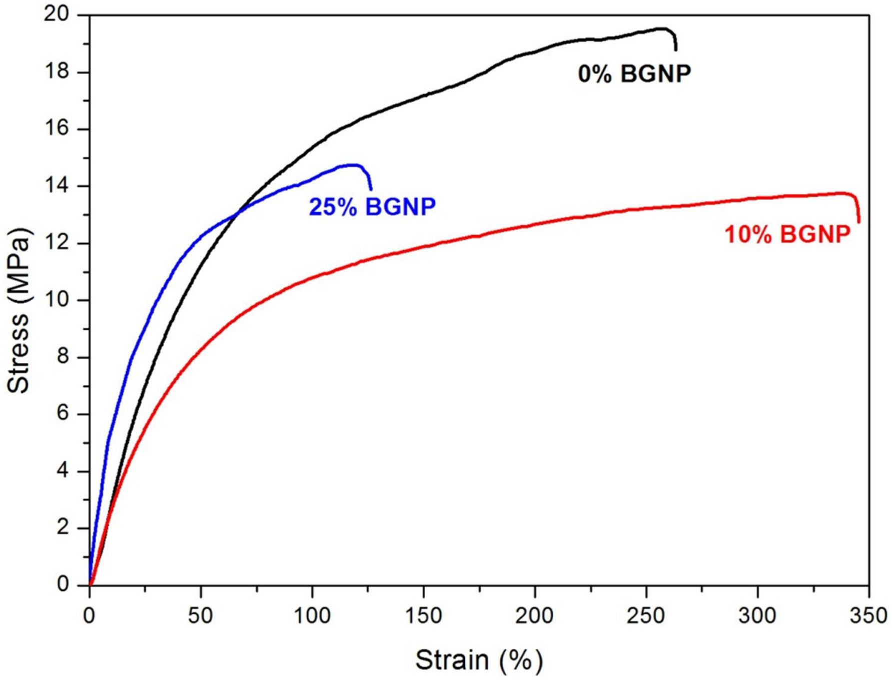

Figure 6.9: Tensile stress–strain curves of films PU/PVA blend, composites PU/PVA with 10 and 25% of BGNP.

For the compression tests, it was not possible to test the composites with 25% of BGNP because they presented very large contraction during the freeze drying process. The samples obtained were very thin, which made the compression test impracticable for these foams (Fig.6.11). The composite foams with 0 and 10 % of BGNP recovered after successive deformations (Fig. 6.10), the second and third deformations occurred 40 minutes after the previous deformation and the recovery of the foams was superior to 95% of the initial length. The composites with 10% of BGNP presented compressive strength higher than the foams without nanoparticles.

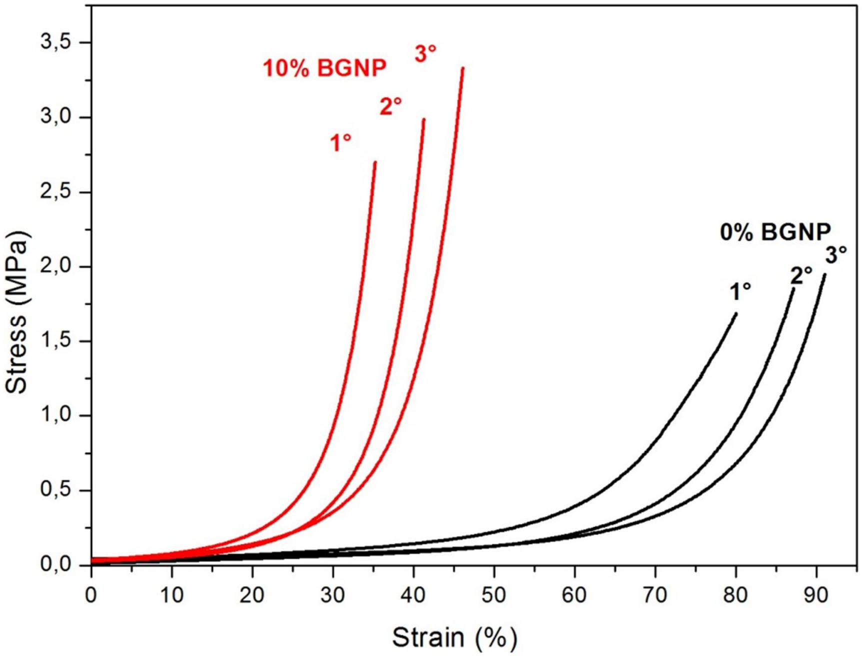

Figure 6.10: Compressive stress–strain curves of composite foams produced PU/PVA blend, composites PU/PVA with 10 and 25% of BGNP.

Figure 6.11: Digital images of foam obtained from composite PU/PVA with 25% of BGNP.

When fillers are added to polymers it is expected an increase in the elastic modulus and strength of the composite obtained. In traditional composites, the modulus can be predicted, within bounds, and the mechanism that leads to a change in modulus is load transfer. If a high modulus filler, as a ceramic, is added to a lower-modulus polymer, then load transfers from the matrix to the filler, leading to an increase in modulus. One important question for nanocomposites is how load is transferred from the matrix to the filler, because in some nanocomposites the polymer chain and filler are almost the same size, and in others, the fillers are atomically smooth, with few functional groups to which the polymer can bond. To fully understand the modulus of nanocomposites, a second mechanism in addition to load transfer must be considered. The filler can constrain the mobility of the polymer chains as well as their relaxation spectra, which can change the glass transition temperature (Tg) and modulus of the matrix. Nano-fillers can also change the degree or type of crystallinity in a polymer, which also changes the modulus [120-122].

The addition of rigid micrometer-scale fillers to a polymer often increases its strength, but decreases the toughness. The reason for the decrease in ductility, is that the fillers or agglomerates act as stress concentrators, and the defects initiated at the filler quickly become larger than the critical crack size that causes failure. Well-dispersed nanoparticles are much smaller than the critical crack size for polymers and need not initiate failure. Thus, they provide an avenue for simultaneously toughening and strengthening polymers. Proper dispersion is critical for achieving this. Many authors report an optimum volume percent of filler and claim that the decrease in strain-to-failure ratio above the optimum is due to agglomeration. Although the small size of nanoparticles should not decrease the strain-to-failure, it also should not cause the observed increase in the strain-to-failure. Clearly, there is a second mechanism operating. First, the toughness of a material can be defined as the energy to cause failure. This is related to the deformation in the material, but also to the volume of material undergoing deformation. Even brittle amorphous polymers such as polystyrene and polymethylmethacrylate have the potential for large deformation, but the volume of material undergoing deformation is small. Material must first strain-soften after yielding and eventually strain-harden. If the material does not strain-soften, then defects in the material lead to stress concentrations that cause catastrophic brittle failure. If strain softening occurs prior to strain hardening, then the strain-hardened region draws a larger volume of material into the deformation zone and a large strain-to-failure results. If strain softening occurs, but not strain hardening, the initially strain-softened material propagates the crack [121].

Plastic deformation and strain hardening can occur via two different mechanisms: crazing and shear yielding. Crazing is the result of dilatational strains that cause an increase in volume and subsequent drawing of the material between the voids (fibrils).Thus, strain softening occurs due to dilatational strains in front of a craze tip and at the craze/matrix boundary, and strain hardening occurs, which allows drawing and strain hardening of the material in the craze. In principle, this allows the crazes to thicken and the volume of deformed material to increase significantly. In many brittle amorphous polymers, failure initiates at the craze/bulk polymer interface and the volume of deformed material is small [120, 122].

For the film composite with 10% of BGNP, the tensile behavior can be explained in terms of the crystallinity change in the material. The nanoparticles interacted with the polymer blend, decreasing this crystallinity, as discussed previously. The reduction in crystallinity increased the polymer mobility and, consequently, decreased this elastic modulus. The composite become more flexible and had a decrease in strength as compared to polymer blend.

For film composite with 25% of BGNP it was observed a brittle behavior. The high fraction of BGNP used could reduce the stability of emulsion, which may have caused the high aggregation of NPs, resulting in weak interactions between the polar groups (siloxane, silanol) on the surface of NPs aggregates with groups of the polymer blend. The decrease in ductility can be attributed to stress concentrators caused by the excess of NPs, which causes failure of the structure. So, the NP filler added to act as reinforcement, in fact acted as an impurity, which may explain the behavior observed.

The compressive stress-strain properties of the foams obtained showed a behavior completely different as compared to the films. The foams presented an elastic behavior, without plastic deformations after three successive deformations and, in this case, the NPs filler acts as reinforcement, increasing the elastic modulus and strength of the composite obtained, without reduction of the elasticity. This behavior can be attributed to the foam shape of the sample analyzed and also to the production process of the foams. The process of film production, allows the mobility of polymer chains. The foam structures were freeze dried, which reduced the mobility of polymer chains and maintainned the border between the composite structures, which led to a change in mechanism to load transfer, and increased the elastic modulus.

The mechanical properties of the scaffolds obtained were improved by using BGNP as filler to produce composite foams. These properties can be good enough to support cell growth and proliferation in tissue engineering scaffold. The foams can be easily shaped during surgical implantation and suitable for uses as flexible scaffolds in several tissue engineering applications.

Evaluation HA layer deposition. The ability of the composite films to form an HA layer was evaluated but only the composite with 10% BGNP remained intact enough to allow the analysis, the composite with 25% of BGNP disappeared after 3 days of immersion in SBF. After soaking in SBF for seven days, the films were washed 3 times with deionized water, dried and analyzed. FTIR confirmed the formation of the Ca-P layer on composites with 10% of BGNP by detecting characteristic vibration modes of the HA bonds after SBF immersion (Figure 6.12). There was a significant reduction of the bonds referred to PVA and soft segments of PU, indicating that after 7 days in SBF the degradation and dissolution of the polymer fraction in the composite occurred.

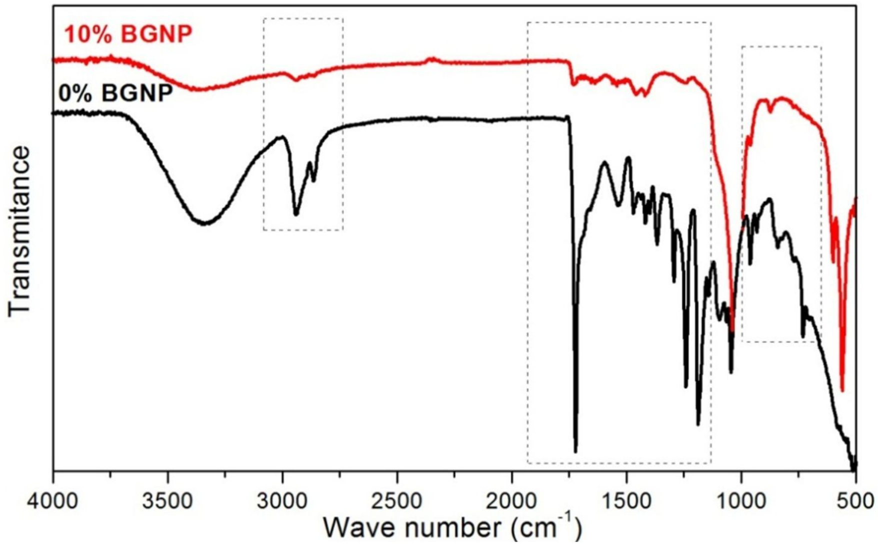

Figure 6.12: FTIR spectra of composite films after soaking in SBF for 7 days. PU/PVA blend (0% BGNP) and composite PU/PVA with 10% of BGNP.

The FTIR spectra presented were enlarged to show the HA characteristic vibrations (Fig. 7.13). The divided P-O peak between 600 and 500 cm^{-1} is assigned to bending vibration of PO_4^{3-} groups and is an indicative of the development of a crystalline Ca-P layer. The C-O stretching vibration of CO_3^{2-} appeared between 890 and 800 cm^{-1} and are suggesting the presence of carbonated Ca-P on the surface of the films [116-119]. The FTIR of PU/PVA blend had almost no change when compared to samples not immersed in SBF, showing that the polymer blend is not able to form an HA layer in this period. This result shows that composite with 10 % BGNP is able to form HA layer in SBF solution. The formation of a HA layer *in vitro* on a material surface is believed to indicate its bioactive potential *in vivo*, which enables to improve tissue regeneration around implants, from both a chemical and biological activity [1-10].

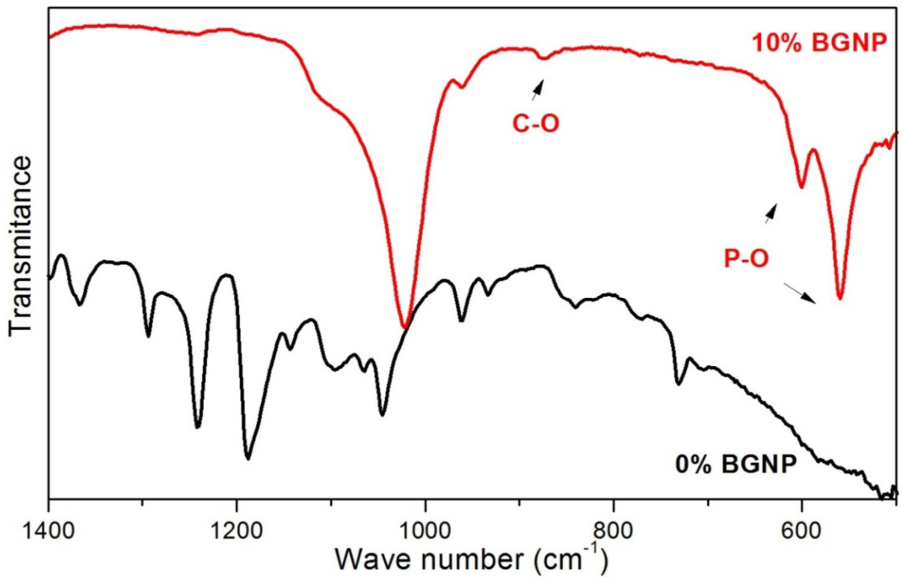

Figure 6.13: Magnification of FTIR composite films after soaking in SBF for 7 days.

The calcium phosphate (CP) layer formed in composite with 10% BGNP surface was also analyzed by SEM (Figure 6.14) and EDS (Fig. 6.15). It can be seen that the surface was completely covered by CP layer nodules after the immersion period. The Ca/P ratio estimated by EDS was 2.0, which confirms a CP layer deposition, as explained in chapter 5.

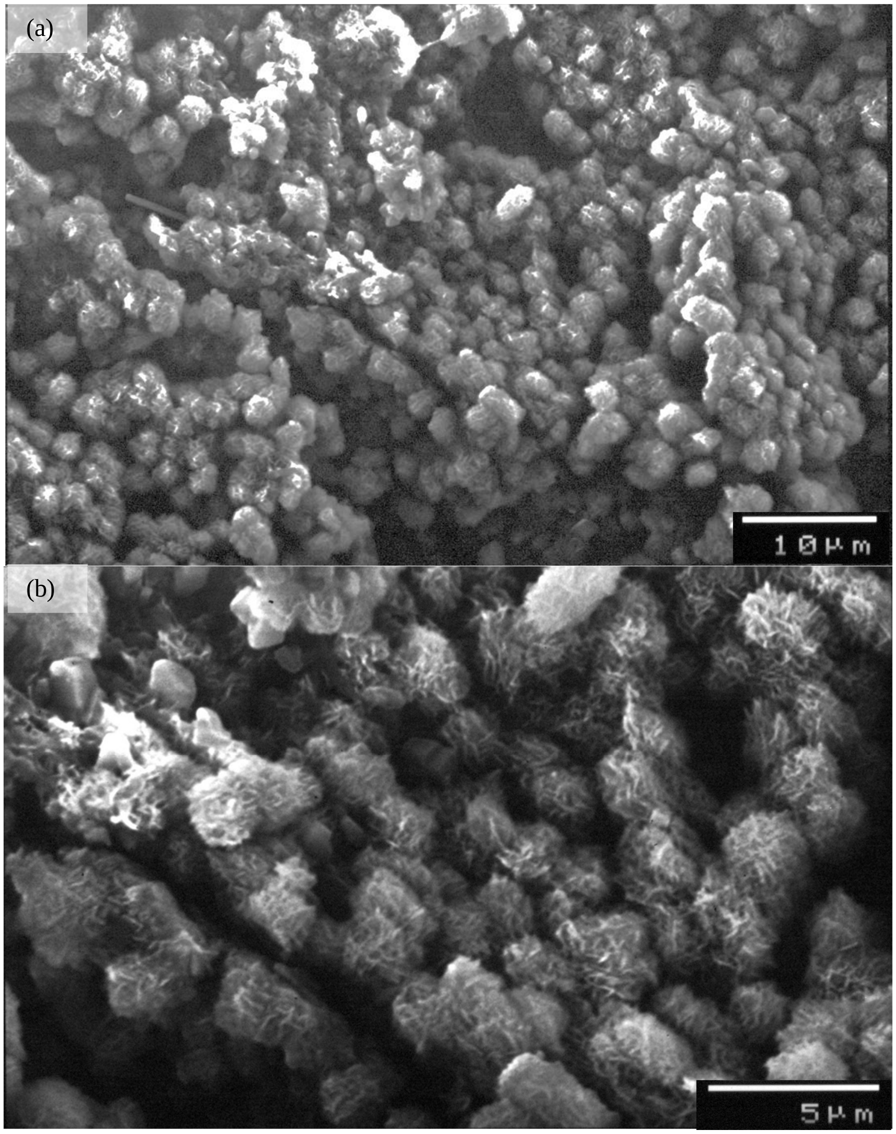

Figure 6.14: (a) SEM image of composite PU/PVA with 10% BGNP after soaking in SBF for 7 days. (b) Magnification of image (a).

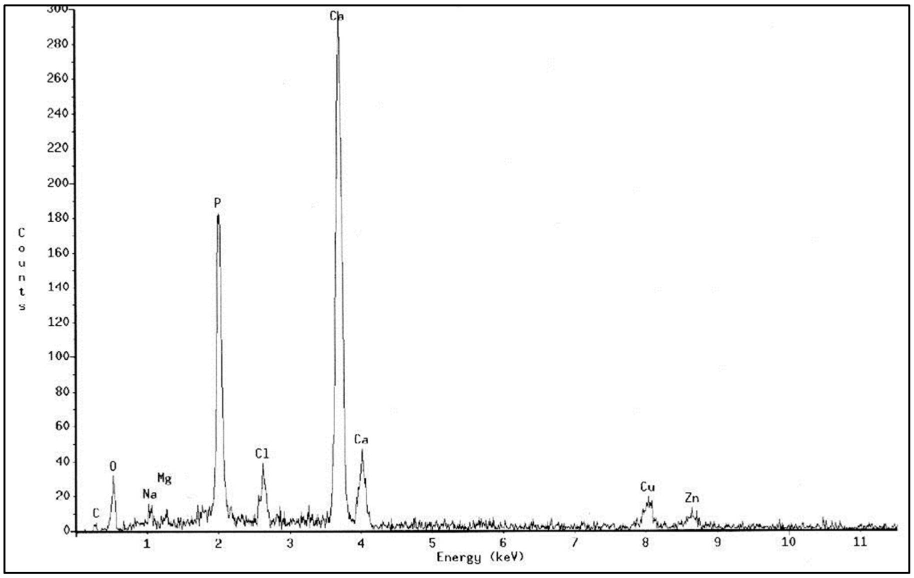

Figure 6.15: EDS of the general area show.

Accelerated degradation test. Figs. 6.16 and 6.17 show the results of MTT assay test for accelerated degradation products of composites at 1 and 24 hours, respectively. The 30% hydrogen peroxide solution is a medium highly reactive that promotes the degradation of PVA and PU soft and hard segments by hydrolysis and oxidation mechanisms, catalyzed by the temperature of 85°C. After 1 hour of immersion, the foams of PU/PVA blend presented mass reduction of (42 ± 4)%, composite with 10% of BGNP presented (53 ± 5)% of reduction and the composite with 25% reduction of (77 ± 3)%.

The composites degradation can be explained following the same hypothesis for PU degradation formulated in chapter 6. These mass reductions can be attributed to the degradation of the soft segment of PU and the PVA chains. For this incubation period, there was no significant difference in the cell viability of the materials and the control, indicating, that degradation products of the polymers have no toxic effect. After 24 hours, there was no solid sample residue visible to the naked eye or caught by 0.45 μm *Millipore* filter, indicating a high level of polymer degradation, including the PU hard segment, by oxidation reactions. There was a reduction of 43% in the cell viability of PU/PVA blend foam as compared to control. This result agrees with the hypothesis that the hard segments of PU were degraded and the degradation products have toxic effects on osteoblast cells. The toxic effect was lower for the composites, 24% of reduction in the cell viability as compared to control, and can be due to the bioactivity of BGNP fraction in the materials [123]. This toxic effect is low, according to the standard, and enables the composite foams for biodegradable scaffold applications.

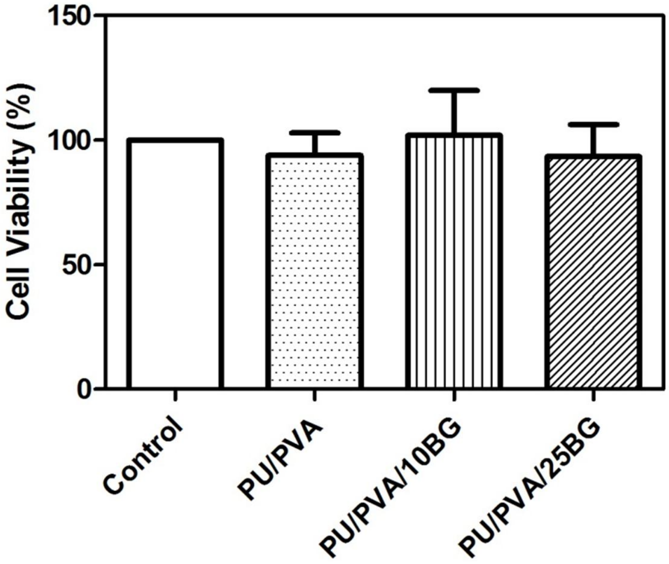

Figure 6.16: Cell viability of materials degradation products in 30% H_2O_2 medium for 1 hour at 85°C by MTT assay. There is no significant difference when compared the samples to control and when different materials are compared together, at a significance level of 0.05)

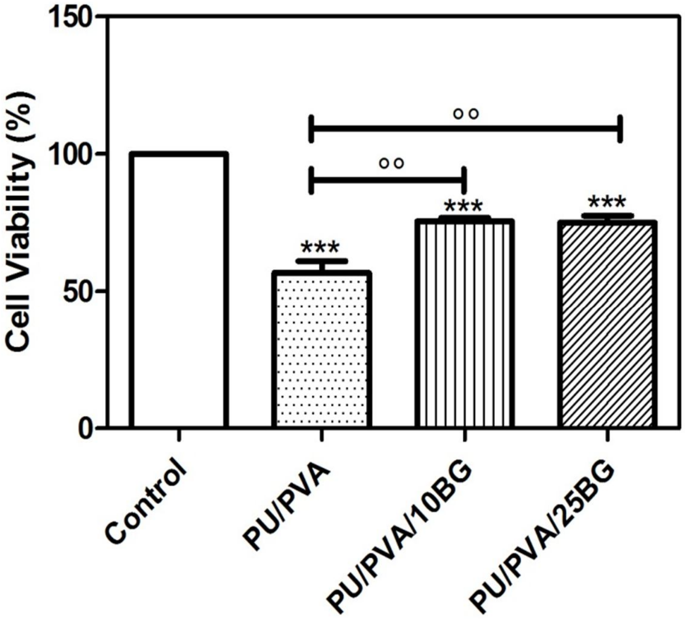

Figure 6.17: Cell viability of materials degradation products in 30% H_2O_2 medium for 24 hours at 85°C by MTT assay. (* Represents significant difference compared to control and ^{o} represents significant difference between different materials at a significance level of 0.05)

6.4 Conclusions

Biodegradable and bioactive composites were produced by the insertion of bioactive glass nanoparticles in the structure of PU/PVA blends. The composite produced with 10% BGNP presented porous structure appropriated for tissue engineering applications and had no significant toxic effect. Also, it was able to form HA layer in SBF solution, an indicative of bioactive potential *in vivo*. The insertion of 10% BGNP in the PU/PVA foam structure worked as reinforcement and improved compressive strength and elastic modulus of the materials. These materials presented mechanical properties still low for applications that require the reproduction of morphology and mechanical properties of mature trabecular bone, but these properties are adequate to support cell growth and proliferation in tissue engineering scaffold.

References

1. Larry L. Hench. The story of Bioglass. J Mater Sci: Mater Med (2006) 17:967–978
2. Tadashi Kokubo, Design of bioactive bone substitutes based on biomineralization process Materials Science and Engineering C 25 (2005) 97–104
3. C. Pritsos, E. Kontonasaki, X. Chatzistavrou, L. Papadopoulou, F. Pappas, P. Koidis, K.M. Paraskevopoulos. Studying morphological characteristics of thermally treated bioactive glass ceramic using image analysis J. Eur, Ceram. Soc 25 (2005) 891
4. Daniel C. Cluppera, John J. Mecholsky Jra, Guy P. LaTorreb, David C. Greenspan. Bioactivity of tape cast and sintered bioactive glass-ceramic in simulated body fluid. Biomaterials 23 (2002) 2599–2606
5. Xiaofeng Chen, Yongchun Meng, Yuli Li, Naru Zha. Investigation on bio-mineralization of melt and sol–gel derived bioactive glasses. Applied Surface Science 255 (2008) 562–564
6. Delia S. Brauer, Natalia Karpukhina, Matthew D. O’Donnell, Robert V. Law, Robert G. Hill. Fluoride-containing bioactive glasses: Effect of glass design and structure on degradation, pH and apatite formation in simulated body fluid. Acta Biomaterialia xxx (2010) xxx–xxx (article in press)
7. Akiko Obata, Satoshi Nakamura, Kimihiro Yamashita. Interpretation of electrical polarization and depolarization mechanisms of bioactive glasses in relation to ionic migration Biomaterials 25 (2004) 5163–5169
8. Julian R. Jones, Olga Tsigkoua, Emily E. Coatesa, Molly M. Stevensa, Julia M. Polakb, Larry L. Hench. Extracellular matrix formation and mineralization on a phosphate-free porous bioactive glass scaffold using primary human osteoblast (HOB) cells Biomaterials 28 (2007) 1653–1663
9. Ian A. Silver, Judith Deas, Maria Erecinska. Interactions of bioactive glasses with osteoblasts in vitro: effects of 45S5 Bioglass, and 58S and 77S bioactive glasses on metabolism, intracellular ion concentrations and cell viability Biomaterials 22 (2001) 175-185
10. E. Hatzistavrou, X. Chatzistavrou, L. Papadopoulou, N. Kantiranis, E. Kontonasaki, A.R. Boccaccini, K.M. Paraskevopoulos. Characterisation of the bioactive behaviour of sol–gel hydroxyapatite–CaO and hydroxyapatite–CaO–bioactive glass composites Materials Science and Engineering C 30 (2010) 497–502
11. A. Balamurugan, G. Sockalingum, J. Michel, J. Fauré, V. Banchet, L. Wortham, S. Bouthors, D. Laurent-Maquin, G. Balossier. Synthesis and characterisation of sol gel derived bioactive glass for biomedical applications Materials Letters 60 (2006) 3752–3757
12. J.P. BorrajoT, P. Gonzalez, S. Liste, J. Serra, S. Chiussi, B. Leon, M. Perez-Amor The role of the thickness and the substrate on the in vitro bioactivity of silica-based glass coatings Materials Science and Engineering C 25 (2005) 187–193

13. Angela L. Andrade, Patrıcia Valerio, Alfredo M. Goes, Maria de Fatima Leite, Rosana Z. Domingues. Influence of morphology on in vitro compatibility of bioactive glasses Journal of Non-Crystalline Solids 352 (2006) 3508–3511
14. Chim H, Hutmacher DW, Chou AM, Oliveira AL, Reis RL, Lim TC, Schantz J-T. A comparative analysis of scaffold material modifications for load-bearing applications in bone tissue engineering. Int J Oral Max Surg (2006) 35 928–934.
15. Xiaohong Wanga, Hongchen Suna, Jiang Chang. Characterization of $Ca_3SiO_5/CaCl_2$ composite cement for dental application dental materials 24 (2008) 74–82
16. Mohammad Ahmad, Julian R Jones and Larry L Hench. Fabricating sol–gel glass monoliths with controlled nanoporosity. Biomed. Mater. 2 (2007) 6–10
17. Jung Sang Cho, Yun Chan Kang. Synthesis of spherical shape borate-based bioactive glass powders prepared by ultrasonic spray pyrolysis Ceramics International 35 (2009) 2103–2109
18. Oana Bretcanu, Xanthippi Chatzistavrou, Konstantinos Paraskevopoulos, Reinhard Conradt, Ian Thompsond, Aldo R. Boccaccini, Sintering and crystallisation of 45S5 Bioglass powder. Journal of the European Ceramic Society 29 (2009) 3299–3306
19. Shuyi Li, Lynsa Nguyen, Hairong Xiong, Meiyao Wang, Tom C Hu, Jin-Xiong She, Steven M. Serkiz, George G. Wicks, William S. Dynan. Porous-wall hollow glass microspheres as novel potential nanocarriers for biomedical applications. Nanomedicine: Nanotechnology, Biology, and Medicine 6 (2010) 127–136
20. Julie Elizabeth Gougha, Julian R. Jones, Larry L. Hench. Nodule formation and mineralisation of human primary osteoblasts cultured on a porous bioactive glass scaffold Biomaterials 25 (2004) 2039–2046
21. Coelho MB, Pereira MM. Sol-gel synthesis of bioactive glass scaffolds for tissue engineering: effect of surfactant type and concentration. Journal of Biomedical Materials Research Part B: Applied Biomaterials (2005) 75B (2) 451-456.
22. Valério P, Guimarães MHR, Pereira MM, Leite MF, Goes AM. Primary osteoblast cell response to sol-gel derived bioactive glass foams. J M S: Materials in Medicine. 2005; 16(9) 851-856.
23. Wei Xia, Jiang Chang. Well-ordered mesoporous bioactive glasses (MBG): A promising bioactive drug delivery system. Journal of Controlled Release 110 (2006) 522 – 530
24. Qiang Fu, Mohamed N. Rahaman, B. Sonny Bal, Roger F. Brown, Delbert E. Day. Mechanical and in vitro performance of 13–93 bioactive glass scaffolds prepared by a polymer foam replication technique Acta Biomaterialia 4 (2008) 1854–1864
25. Yufang Zhu, Chengtie Wu, Yogambha Ramaswamy, Emanuel Kockrick, Paul Simon, Stefan Kaskel, Hala Zreiqat. Preparation, characterization and in vitro bioactivity of mesoporous bioactive glasses (MBGs) scaffolds for bone tissue engineering. Microporous and Mesoporous Materials 112 (2008) 494–503

26. Bo Lei, Xiaofeng Chen , Yingjun Wang, Naru Zhao, Chang Du, Liming Fang. Synthesis and bioactive properties of macroporous nanoscale SiO_2–CaO–P_2O_5 bioactive glass Journal of Non-Crystalline Solids 355 (2009) 2678–2681
27. R. Ravarian, F. Moztarzadeh, M. Solati Hashjin, S.M. Rabiee, P. Khoshakhlagh, M. Tahriri Synthesis, characterization and bioactivity investigation of bioglass/hydroxyapatite composites Ceramics International 36 (2010) 291–297
28. Devis Bellucci, Valeria Cannillo, Antonella Sola. Shell Scaffolds: A new approach towards high strength bioceramic scaffolds for bone regeneration. Materials Letters 64 (2010) 203–206
29. C.J. Shih, W.C. Chen, Y.T. Wang, Synthesis and in vitro bioactivity of mesoporous bioactive glass scaffolds, Materials Science & Engineering C (2010), doi: 10.1016/j.msec.2010.02.006
30. Juan Peña, Jesús Román, M. Victoria Cabañas, María Vallet-Regí, An alternative technique to shape scaffolds with hierarchical porosity at physiological temperature. Acta Biomaterialia 6 (2010) 1288–1296
31. Daniel Arcos, María Vallet-Regí. Sol–gel silica-based biomaterials and bone tissue regeneration. Acta Biomaterialia xxx (2010) xxx–xxx (article in press)
32. K. Rezwan, Q.Z. Chena, J.J. Blakera, Aldo Roberto Boccaccinia. Biodegradable and bioactive porous polymer/inorganic composite scaffolds for bone tissue engineering. Biomaterials 27 (2006) 3413–3431
33. Pereira MM, Jones J, Hench LL: Bioactive glass and hybrid scaffolds prepared by sol–gel method for bone tissue engineering Adv in Appl Ceram (2005) 104:35-42.
34. K.A. Padmanabhan. Mechanical properties of nanostructured materials. Materials Science and Engineering A304–306 (2001) 200–205
35. T.J. Webster, R.W. Siegel, R. Bizios. Osteoblast Adhesion on Nanophase Ceramics. Biomaterials 20 (1999) 1221.
36. T.J. Webster, C. Ergun, R.H. Doremus, R.W. Siegel, R. Bizios. Nanoceramic surface roughness enhances osteoblast and osteoclast functions for improved orthopaedic/dental implant efficacy j. Biomed. Mater. Res. 51 (2000) 475.1261.
37. Ostomel TA, Shi Q, Tsung CK, Liang H, Stucky GD., Spherical bioactive glass with enhanced rates of hydroxyapatite deposition and hemostatic activity. Small. (2006) 11 1261-5.
38. D.Z. Chen, C.Y. Tang, K.C. Chan, C.P. Tsui, Peter H.F. Yu, Mason C.P. Leung, P.S. Uskokovic. Dynamic mechanical properties and in vitro bioactivity of PHBHV/HA nanocomposite. Composites Science and Technology 67 (2007) 1617–1626
39. Oliveira AAR, Oréfice, RL, Mansur HS, Pereira MM. Effect of Increasing Polyvinyl Alcohol Content on the Porous Structure and Mechanical Properties of Sol-Gel Derived Hybrid Foams Key Engineering Materials. 361-363 (2008) 555-558

40. Costa H, Oliveira AAR, Oréfice, RL, Mansur HS, Pereira MM. Tailoring Mechanical Behavior of PVA-Bioactive Glass Hybrid Foams Key Engineering Materials. 361-363 (2008) 289-292
41. Herman S. Mansur, Hermes S. Costa. Nanostructured poly(vinyl alcohol)/bioactive glass and poly(vinyl alcohol)/chitosan/bioactive glass hybrid scaffolds for biomedical applications. Chemical Engineering Journal 137 (2008) 72–83
42. Tiiu Niemela, Henna Niiranen, Minna Kellomaki. Self-reinforced composites of bioabsorbable polymer and bioactive glass with different bioactive glass contents. Part II: In vitro degradation. Acta Biomaterialia 4 (2008) 156–164
43. V. Cannillo, F. Chiellini, P. Fabbri, A. Sola. Production of Bioglass 45S5 – Polycaprolactone composite scaffolds via salt-leaching. Composite Structures 92 (2010) 1823–1832
44. Chengtie Wu, Yufeng Zhang, Yufang Zhu, Thor Friis, Yin Xiao. Structure–property relationships of silk-modified mesoporous bioglass scaffolds. Biomaterials 31 (2010) 3429–3438
45. Xuejun Wang, Guojun Song, Tao Lou. Fabrication and characterization of nano-composite scaffold of PLLA/silane modified hydroxyapatite Medical Engineering & Physics 32 (2010) 391–397
46. Kyung-Tae Noh, Hye-Young Lee, Ueon-Sang Shin, Hae-Won Kim. Composite nanofiber of bioactive glass nanofiller incorporated poly(lactic acid) for bone regeneration Materials Letters 64 (2010) 802–805
47. Abeer M. El-Kady, Ebtsam A. Saad, Bothaina M. Abd El-Hady, Mohmmad M. Farag aSynthesis of silicate glass/poly(L-lactide) composite scaffolds by freeze-extraction technique: Characterization and in vitro bioactivity evaluation Ceramics International 36 (2010) 995–1009
48. Superb K. Misra, F. Ohashi, Sabeel P. Valappil, Jonathan C. Knowles, I. Roy f, S. Ravi P. Silva, Vehid Salih, Aldo R. Boccaccini. Characterization of carbon nanotube (MWCNT) containing P(3HB)/bioactive glass composites for tissue engineering applications Acta Biomaterialia 6 (2010) 735–742
49. Mathew Petera, N.S. Binulala, S.V. Naira, N. Selvamurugana,b, H. Tamurac, R. Jayakumara, Novel biodegradable chitosan–gelatin/nano-bioactive glass ceramic composite scaffolds for alveolar bone tissue engineering Chemical Engineering Journal 158 (2010) 353–361
50. Aixue Liu, Zhongkui Hong, Xiuli Zhuang, Xuesi Chen, Yang Cui, Yi Liu, Xiabin Jing. Surface modification of bioactive glass nanoparticles and the mechanical and biological properties of poly(L-lactide) composites Acta Biomaterialia 4 (2008) 1005–1015
51. Daniela S. Couto, Zhongkui Hong, João F. Mano. Development of bioactive and biodegradable chitosan-based injectable systems containing bioactive glass nanoparticles. Acta Biomaterialia 5 (2009) 115–123

52. Wadcharawadee Noohom, Kevin S Jack, Darren Martin and Matt Trau. Understanding the roles of nanoparticle dispersion and polymer crystallinity in controlling the mechanical properties of HA/PHBV nanocomposites Biomed. Mater. 4 (2009) 015003 (13pp)
53. Sen Lin, Claudia Ionescu, Kevin J. Pike, Mark E. Smithb and Julian R. Jones. Nanostructure evolution and calcium distribution in sol–gel derived bioactive glass J. Mater. Chem. (2009) 19
54. Wei Xia, Jiang Chang. Preparation and characterization of nano-bioactive-glasses (NBG) by a quick alkali-mediated sol–gel method Materials Letters 61 (2007) 3251–3253
55. Wei Xia a,b, Jiang Chang. Preparation and characterization of nano-bioactive-glasses (NBG) by a quick alkali-mediated sol–gel method. Materials Letters 61 (2007) 3251–3253
56. G.S. Pappas, P. Liatsi, I.A. Kartsonakis, I. Danilidis, G. Kordas. Synthesis and characterization of new SiO2–CaO hollow nanospheres by sol–gel method: Bioactivity of the new system. Journal of Non-Crystalline Solids 354 (2008) 755–760
57. Zhongkui Hong, Esther G. Merino, Rui L. Reis and Joao F. Mano. Novel Rice-shaped Bioactive Ceramic Nanoparticles. Advanced Engineering Materials (2009) 11 (5) 25-29
58. Zhongkui Hong, Aixue Liu, Li Chen, Xuesi Chen. Xiabin Jing. Preparation of bioactive glass ceramic nanoparticles by combination of sol–gel and coprecipitation method. Journal of Non-Crystalline Solids 355 (2009) 368–372
59. Hong Z, Reis RL, Mano JF. Preparation and in vitro characterization of novel bioactive glass ceramic nanoparticles. J Biomed Mater Res A, in press. Preparation of bioactive glass ceramic nanoparticles by combination of sol–gel and coprecipitation method Journal of Non-Crystalline Solids 355 (2009) 368–372
60. Zhongkui Hong, Aixue Liu, Li Chen, Xuesi Chen, Xiabin Jing. Preparation of bioactive glass ceramic nanoparticles by combination of sol–gel and co-precipitation method. Journal of Non-Crystalline Solids 355 (2009) 368–372
61. Hui-suk Yun, Seung-eon Kim, Young-taek Hyun. Preparation of bioactive glass ceramic beads with hierarchical pore structure using polymer self-assembly technique. Materials Chemistry and Physics 115 (2009) 670–676
62. L. Borum, O.C. Wilson Jr. Surface modification of hydroxyapatite.Part II.Silica. Biomaterials 24 (2003) 3681–3688
63. Anna M. Lipski a, Christopher J. Pino b, Frederick R. Haselton b, I.-Wei Chen a, V. Prasad Shastri. The effect of silica nanoparticle-modified surfaces on cell morphology, cytoskeletal organization and function. Biomaterials 29 (2008) 3836–3846
64. Sneha Kulkarni, Asad Syed, Sanjay Singh, Anil Gaikwad, Kashinath Patil, K. Vijayamohanan, Absar Ahmad, Satishchandra Ogale. Silicate nanoparticles by bioleaching of glass and modification of the glass surface. Journal of Non-Crystalline Solids 354 (2008) 3433–3437

65. Aneta J. Mieszawska, Nikolaos Fourligas, Irene Georgakoudi, Nadia M. Ouhib, David J. Belton , Carole C. Perry, David L. Kaplan. Osteoinductive silkesilica composite biomaterials for bone regeneration. Biomaterials 31 (2010) 8902-8910
66. Alejandro Simón de Dios, Marta Elena Díaz-García. Multifunctional nanoparticles: Analytical prospects. Analytica Chimica Acta 666 (2010) 1–22
67. Sheyda Labbaf , Olga Tsigkou , Karin H. Müller , Molly M. Stevens, Alexandra E. Porter, Julian R. Jones. Spherical bioactive glass particles and their interaction with human mesenchymal stem cells in vitro. Biomaterials 32 (2011) 1010-1018
68. Guan JJ, Sacks MS, Beckman EJ, Wagner WR Synthesis, characterization and cytocompatibility of elastomeric, biodegradable poly(ester-urethane)ureas based on poly(caprolactone) and putrescine. J Biomed Mater Res 61 (2002) 3: 493.
69. Alperin C, Zandstra PW, Woodhouse KA. Polyurethane films seeded with embryonic stem cell-derived cardiomyocytes for use in cardiac tissue engineering applications. Biomaterials 26 (2005) 7377.
70. Poussard L, Burel F, Couvercelle JP, Merhi Y, Tabrizian M, Bunel C. Haemocompatibility of new ionic polyurethanes. influence of carboxylic group insertion modes. Biomaterials 25 (2004) 3473-83.
71. Spaans C J, Belgraver VW, Rienstra O, Groot JH, Veth RP. Solvent-free fabrication of micro-porous polyurethane amide and polyurethane-urea scaffolds for repair and replacement of the knee-joint meniscus. Biomaterials 21 (2000) 2453.
72. Mehrdad Mahkama, Nasser Sharifi-Sanjani. Preparation of new biodegradable polyurethanes as a therapeutic agent. Polymer Degradation and Stability 80 (2003) 199–202
73. Eliane Ayres, Rodrigo L. Oréfice, M. Irene Yoshida. Phase morphology of hydrolysable polyurethanes derived from aqueous dispersions. European Polymer Journal 43 (2007) 3510–3521
74. Gisele Rodrigues da Silva, Armando da Silva-Cunha Jr., Francine Behar-Cohen, Eliane Ayres, Rodrigo L. Oréfice. Biodegradation of polyurethanes and nanocomposites to non-cytotoxic degradation products. Polymer Degradation and Stability 95 (2010) 491-499
75. T. Thomson. Design and Application of Hydrophilic Polyurethanes – Medical, Agriculture and Other Applications. CRC Press (2000) ISBN-10: 1566768950
76. A. Anand Prabu, M. Alagar. Mechanical and thermal studies of intercross-linked networks based on siliconized polyurethane-epoxy/unsaturated polyester coatings. Progress in Organic Coatings 49 (2004) 236–243
77. Qiu Gen Zhang, Qing Lin Liu , Zhong Ying Jiang, Li Yi Ye, Xiu Hua Zhang. Effects of annealing on the physico-chemical structure and permeation performance of novel hybrid membranes of poly(vinyl alcohol)/c-aminopropyl-triethoxysilane. Microporous and Mesoporous Materials 110 (2008) 379–391
78. D.K. Chattopadhyay, K.V.S.N. Raju. Structural engineering of polyurethane coatings for high performance applications. Prog. Polym. Sci. 32 (2007) 352–418

79. H. Sardon, L. Irusta, M.J. Fernández-Berridi, M. Lansalot, E. Bourgeat-Lami. Synthesis of room temperature self-curable waterborne hybrid polyurethanes functionalized with (3-aminopropyl)triethoxysilane (APTES). Polymer 51 (2010) 5051-5057
80. C. Jeffrey Brinker and George W. Scherer. The sol-el science the physics and chemistry of sol-gel processing. Academic Press, Inc. (1990) ISBN 0-12-134970-5
81. Roger Brown. Handbook of polymer testing: short-term mechanical tests. Rapra Technology (2002) ISBN: 1-85957-324-X
82. Patrick Vermette, Hans J. Griesser, Gaétan Laroche and Robert Guidoin. The tissue engineering intelligence unit 6: biomedical applications of polyurethanes. Landes Bioscience (2001) ISBN: 1-58706-023-X.
83. Tim Thomson. Polyurethanes as specialty chemicals: principles and applications. CRC Press (2005) ISBN: 0-8493-1857-2.
84. J Santerrea, K Woodhouse, G Laroche, RS Labow. Understanding the biodegradation of polyurethanes: From classical implants to tissue engineering materials. Biomaterials 26 (2005) 7457–7470.
85. Shadi Hassan Ajili, Nadereh Golshan Ebrahimi, Masoud Soleimani. Polyurethane/polycaprolactane blend with shape memory effect as a proposed material for cardiovascular implants. Acta Biomaterialia 5 (2009) 1519–1530.
86. Molamma P Prabhakaran1, J Venugopal1, Dan Kai, Seeram Ramakrishna1. Biomimetic material strategies for cardiac tissue engineering. Materials Science & Engineering (2010) Article in Press.
87. JH Ashton, JAM Mertz, JL Harper, MJ Slepian, JL Mills, DV McGrath, JP Vande Geest. Polymeric endoaortic paving: Mechanical, thermoforming, and degradation properties of polycaprolactone/polyurethane blends for cardiovascular applications. Acta Biomaterialia 7 (2011) 287–294.
88. Steven G Wise, Michael J Byrom, Anna Waterhouse, Paul G Bannon, Martin KCN, Anthony S Weiss. A multilayered synthetic human elastin/polycaprolactone hybrid vascular graft with tailored mechanical properties. Acta Biomaterialia 7 (2011) 295–303.
89. Sibylle Grada, Laszlo Kupcsika, Katarzyna Gornab, Sylwester Gogolewskib, Mauro Alinia. The use of biodegradable polyurethane scaffolds for cartilage tissue engineering: potential and limitations. Biomaterials 24 (2003) 5163–5171.
90. Joanne E McBane, Loren A Matheson, Soroor Sharifpoor, J Paul Santerre, Rosalind S Labow. Effect of polyurethane chemistry and protein coating on monocyte differentiation towards a wound healing phenotype macrophage. Biomaterials 30 (2009) 5497–5504.
91. Ian C Bonzani, Raju Adhikari, Shadi Houshyar, Roshan Mayadunne, Pathiraja Gunatillake, Molly M Stevensa. Synthesis of two-component injectable polyurethanes for bone tissue engineering Biomaterials 28 (2007) 423–433.

92. Monika Bil, Joanna Ryszkowska, Piotr Wozniak, Krzysztof J Kurzydłowski, Magorzata Lewandowska-Szumie. Optimization of the structure of polyurethanes for bone tissue engineering applications. Acta Biomaterialia 6 (2010) 2501–2510.
93. Piotr Wozniak, Monika Bil, Joanna Ryszkowska, Piotr Wychowanski, Edyta Wróbel, Anna Ratajska, Grazyna Hoser, Jacek Przybylski, Krzysztof J Kurzydłowski, Magorzata Lewandowska-Szumie. Candidate bone-tissue-engineered product based on human-bone-derived cells and polyurethane scaffold. Acta Biomaterialia 6 (2010) 2484–2493.
94. Scott A Guelcher, Katie M Gallagher, Jonathan E Didier, Derek B Klinedinst, John S Doctor, Aaron S Goldstein, Garth L Wilkes, Eric J Beckman, Jeffrey O Hollinger. Synthesis of biocompatible segmented polyurethanes from aliphatic diisocyanates and diurea diol chain extenders Acta Biomaterialia 1 (2005) 471–484.
95. Danielle N Rockwood, Robert E Akins Jr, Ian C Parrag, Kimberly A Woodhouse, John F Rabolt. Culture on electrospun polyurethane scaffolds decreases atrial natriuretic peptide expression by cardiomyocytes in vitro Biomaterials 29 (2008) 4783–4791
96. M Zanetta, N Quirici, F Demarosi, MC Tanzi, L Rimondini, S Fare. Ability of polyurethane foams to support cell proliferation and the differentiation of MSCs into osteoblasts. Acta Biomaterialia 5 (2009) 1126–1136
97. Rui Chena, Chen Huanga, Qinfei Kea, Chuanglong Heb, Hongsheng Wangb, Xiumei Mob. Preparation and characterization of coaxial electrospun thermoplastic polyurethane/collagen compound nanofibers for tissue engineering applications Colloids and Surfaces B: Biointerfaces 79 (2010) 315–325
98. Milena Spírková, Jelena Pavlicević, Adam Strachota, Rafal Poreba, Oskar Bera, Ludmila Kaprálková, Josef Baldrian, Miroslav Slouf, Nada Lazić, Jaroslava Budinski-Simendić. Novel polycarbonate–based polyurethane elastomers: composition – property relationship European Polymer Journal (2010) Article in Press
99. Ji Hye Hong, Hyun Jeong Jeon, Jae Heung Yoo, Woong-Ryeol Yu, Ji Ho Youk. Synthesis and characterization of biodegradable poly(3-caprolactone-co-b-butyrolactone)-based polyurethane. Polymer Degradation and Stability 92 (2007) 1186-1192
100. Lisa Tatai, Tim G. Moore, Raju Adhikari, Franc-ois Malherbe, Ranjith Jayasekara, Ian Griffiths, Pathiraja A. Gunatillak. Thermoplastic biodegradable polyurethanes: The effect of chain extender structure on properties and in-vitro degradation. Biomaterials 28 (2007) 5407–5417.
101. Zhigang Xie, Changhai Lu, Xuesi Chen, Li Chen, Xiuli Hu, Quan Shi, Xiabin Jing. A facile approach to biodegradable poly(e-caprolactone)-poly(ethylene glycol)-based polyurethanes containing pendant amino groups. European Polymer Journal 43 (2007) 2080–2087
102. C. Mauli Agrawal, Jack E. Parr, Steve T. Lin. Synthetic bioabsorbable polymers for implants. ASTM STP 1396 Library of Congress Catalogin in Publication Data (1999) 39-57
103. T. Thomson. Design and Application of Hydrophilic Polyurethanes – Medical, Agriculture and Other Applications. CRC Press (2000) ISBN-10: 1566768950

104. RaH mila, M. Vallet-Regí. Static and dynamic in vitro study of a sol-gel glass bioactivity. Biomaterials 22 (2001) 2301-2306
105. S. Padilla, J. Roman, S. Sanchéz-Salcedo, M. Vallet-Regí. Hydroxyapatite/SiO2–CaO–P2O5 glass materials: In vitro bioactivity and biocompatibility. Acta Biomaterialia 2 (2006) 331–342.
106. Mohamed Mami, Anita Lucas-Girot, Hassane Oudadesse, Rachida Dorbez-Sridi, Fatima Mezahi, Elodie Dietrich. Investigation of the surface reactivity of a sol–gel derived glass in the ternary system SiO2–CaO–P2O5. Applied Surface Science 254 (2008) 7386–7393.
107. Shan Zhao, Yanbao Li, Dongxu Li. Synthesis and in vitro bioactivity of CaO–SiO2–P2O5 mesoporous microspheres. Microporous and Mesoporous Materials 135 (2010) 67–73.
108. Julian R. Jones, Lisa M. Ehrenfried, Larry L. Hench. Optimising bioactive glass scaffolds for bone tissue engineering. Biomaterials 27 (2006) 964–973
109. J Ma, C Z Chen, D G Wang, X G Meng, J Z Shi. Influence of the sintering temperature on the structural feature and bioactivity of sol–gel derived SiO2–CaO–P2O5 bioglass. Ceramics International 36 (2010) 1911–1916
110. X F Gian, J Yin, X X Guo, Y F Yang, Z K Zhu, J Lu. Polymer-inorganic nanocomposites prepared by hydrothermal method: PVA/ZnS, PVA/CdS, preparation and characterization. Journal of Materials Science Letters 19 (2000) 2235 – 2237
111. Chun-Chen Yang. Chemical composition and XRD analyses for alkaline composite PVA polymer electrolyte. Materials Letters 58 (2003) 33– 38
112. R Seoudi, S Abd El Mongy, A A Shabaka. Effect of polyvinyl alcohol matrices on the structural and spectroscopic studies of CdSe nanoparticles. Physica B 403 (2008) 1781–1786
113. Tim Thomson. Polyurethanes as specialty chemicals: principles and applications. CRC Press (2005) ISBN: 0-8493-1857-2
114. D K Chattopadhyay, K V S N Raju. Structural engineering of polyurethane coatings for high performance applications. Prog. Polym. Sci. 32 (2007) 352–418
115. Jeffrey O. Hollinger Thomas A. Einhorn, Bruce A. Doll and Charles Sfeir. Bone tissue engineering. CRC Press (2000) ISBN: 0-8493-1621-9
116. Hench LL. Bioceramics: From concept to clinic. J Am Ceram Soc (1991) 74(7):1487–1510
117. M Vallet-Regí, A.M. Romero, C.V. Ragel, R.Z. LeGeros, J. Biomed. Mater. Res. 44 (1999) 416
118. Fujiu T, Ogino M. Difference of bone-bonding behavior among surface active glasses and sintered apatite. J Biomed Mater Res (1984) 18:845–859
119. Ducheyne P, Radin S, King L. The effect of calcium phosphate ceramic composition and structure on in vitro behavior. I. Dissolution. J Biomed Mater Res (1993) 27:25–34
120. TA Vilgis, G Heinrich, M Klüppel. Reinforcement of polymer nano-composites. Cambridge University Press (2009) e-ISBN 978-0-511-60501-7

121. K.T. Ramesh. Nanomaterials: mechanics and mechanisms. The Johns Hopkins University (2009) e-ISBN 978-0-387-09783-1

122. P. M. Ajayan, L. S. Schadler, P. V. Braun. Nanocomposite Science and Technology Wiley-VCH (2003) ISBN 3-527-30359-6

123. Patrick Vermette, Hans J. Griesser, Gaétan Laroche and Robert Guidoin. The tissue engineering intelligence unit 6: biomedical applications of polyurethanes. Landes Bioscience (2001) ISBN: 1-58706-023-X.

7 Considerações Finais

7.1 Conclusões

Nanopartículas de vidro bioativo com composição nominal 60% SiO_2-36% CaO-4% P_2O_5 foram obtidas com sucesso pelo método de Stöber modificado. As partículas obtidas possuem forma esférica, diâmetro médio de (87 ± 5) nm, elevada de área superficial (534 m^2/g) e volume de poros (1,11 cm^2/g) em comparação com as micropartículas (76,4 m^2/g) e (0,38 cm^2/g), respectivamente. Além disso, as NPs exibiram um aumento considerável, de 50%, na viabilidade de osteoblastos em comparação às MPs, em ensaios de MTT. Esses resultados sugerem que as BGNP podem oferecer desempenho superior no desenvolvimento de materiais bioativos em comparação com as micropartículas.

Variações no potencial zeta, em função de diferentes períodos de imersão das partículas em SBF, podem ser diretamente relacionadas à formação de uma camada de HAC na superfície dos materiais. As variações de potencial zeta ocorreram mais rapidamente e tiveram variações maiores nas nanopartículas, sugerindo que a cinética de formação da camada de HAC na superfície das partículas é influenciada pelo tamanho das mesmas. Provavelmente essa diferença observada entre nano e micropartículas se deve à área superficial das NPs significativamente maior, que aumenta a nucleação de HA na superfície das nanopartículas e é responsável pelo efeito estimulante sobre a proliferação de osteoblastos observada na fase inicial de incubação, em ensaios de viabilidade celular por Resazurina e atividade de fosfatase alcalina. Estes resultados estão de acordo com a hipótese de que as nanopartículas são mais bioativas que as micropartículas.

Dispersões aquosas de poliuretanas biodegradáveis foram produzidas com sucesso a partir de poliois PCL, diisocianato HDI e terminadas com grupos silano. Os filmes obtidos apresentaram resistência à tração de 17 MPa, deformação máxima de 260% e módulo de elasticidade de 521 MPa. Espumas flexíveis foram produzidas com tamanho de poros na faixa de 50 to 300 μm, e propriedades mecânicas adequadas para suportar adesão e crescimento celular. Foi feita a degradação acelerada das espumas de PU em ambiente altamente oxidativo, a fim de causar a degradação completa do polímero. Os resultados mostram que os produtos de degradação dessas matrizes induzem resposta tóxica moderada quando em contato direto com osteoblastos, em ensaios de viabilidade celular por MTT. São necessários estudos complementares para se avaliar esse efeito tóxico em ensaios de degradação compatíveis com as condições em meio biológico. Além disso, é de fundamental importância avaliar a composição e concentração dos produtos de degradação liberados em tais condições.

Materiais compósitos obtidos pela inserção de nanopartículas de vidro bioativo na estrutura de blendas de poliuretanas biodegradáveis e álcool polivinílico foram obtidos com composição de nanopartículas de 10 e 25% em massa. Os compósitos produzidos com 10% em massa de BGNP apresentaram estrutura de poros na faixa desejada e potencial tóxico reduzido a níveis não significativos. Além disso, houve a formação de uma camada de HA uniforme sobre toda a extensão do material, após 7 dias de imersão em SBF. A incorporação de 10% de BGNP em espumas poliméricas da blenda PU/PVA atuou como reforço e melhorou a resistência à compressão e o módulo de elasticidade desses materiais. As espumas compósitas com 10% de nanopartículas mostraram-se candidatas excelentes para serem utilizadas como *scaffolds* flexíveis para diversos usos em engenharia de tecidos, pois atendem aos requisitos necessários de porosidade, tamanho de poros, propriedades mecânicas e elevada bioatividade, necessários à aplicação.

7.2 Sugestões para trabalhos futuros

- Utilizar a técnica de espectroscopia por comprimento de onda dispersivo (WDS) para determinar quantitativamente a composição das nanopartículas obtidas e também para determinar a composição da camada de HA formada em sua superfície após ensaios *in vitro*.
- Estudar a modificação da superfície das nanopartículas por grupos apolares, com o objetivo de se obter partículas dispersíveis em solventes e polímeros apolares.
- Estudar o efeito da composição das nanopartículas em sua bioatividade, pela preparação de materiais com componentes variados, como: monocompomente, SiO_2, bicompomente, SiO_2-CaO e SiO_2-P_2O_5 e tricompomentes, SiO_2-CaO-P2O5, e/ou variando-se as composições das frações mássicas de cada componente.
- Utilizar as técnicas de análise termogravimétrica (TG e DSC) para obter mais informações a respeito dos segmentos rígidos e macios da poliuretana obtida.
- Estudar o efeito da variação na composição dos componentes dos segmentos rígidos e flexível nas propriedades das poliuretanas.
- Avaliar o efeito tóxico do produto de degradação da PU em ensaios de degradação compatíveis com as condições em meio biológico.
- Determinar a composição e concentração dos produtos de degradação liberados em tais condições.
- Sintetizar PUs a partir de outros poliois biodegradáveis, tais como, polietileno glicol (PEG) e polibutadieno líquido hidroxilado (PBLH), de custo menor que os PCLs empregados. E/ou utilizar outros diisocianatos alifáticos, como lisina diisocianato (LDI) e diciclohexilmetano diisocianato (HMDI) e avaliar as propriedades dos materiais obtidos.
- Incorporar as nanopartículas na fase polimérica durante a síntese de PU em diferentes estágios da reação e avaliar se tais mudanças geram variações nas propriedades das PUs.
- Incorporar as BGNPs em diferentes polímeros biodegradáveis, como quitosana, celulose, ácido poliláctico, entre outros.

Apêndice

Este apendice apresenta informações complementares relativas ás tecnicas de caracterização dos materiais obtidos neste trabalho bem como sobre os equipamentos e locais onde foram realizadas. Os materiais foram produzidos, na forma de pó, filmes e espumas, foram sintetizados no Laboratório de Biomateriais no Departamento de Engenharia Metalúrgica e de Materiais da Universidade Federal de Minas Gerais (UFMG) e caracterizados por espectroscopia por reflexão difusa de infravermelho com transformada de Fourier (FTIR), difração de raios-X (XRD), microscopias eletrônicas de varredura (MEV) e transmissão (TEM), espectroscopia de energia dispersiva de raios-X (EDS), espalhamento de luz dinâmico (DLS), potencial zeta e análises de BET.

As análises de FTIR foram realizadas no Laboratório de Sínteses Orgânicas do Depto. de Química da UFMG, no equipamento Perkin Elmer Spectrum 100. Os espectros foram coletados na faixa do infravermelho médio de 500 a 4000 cm^{-1} no modo micro-ATR. As amostras em pó foram diluídas em KBr com uma razão de diluição de 1:100.

As análises de XRD foram realizadas no Laboratório de Metalografia e Tratamentos Térmicos do Depto. de Engenharia Metalúrgica e de Materiais da UFMG, no difratômetro PW1700 Philips. Os espectros foram coletados usando radiação Cu $K\alpha$ de 40 KV/40 mA entre 4,05 e 89,95 ° com passo de 0,06 ° e tempo de permanência de 1,5 segundo.

As análises de microscopia eletrônica foram realizadas no Centro de Microscopia da UFMG. As imagens de MEV foram obtidas no equipamento Tecnai G220 FEI e as de TEM no Quanta 200 FEG FEI, ambos equipados com EDS.

Os espectros EDS foram todos obtidos na mesma intensidade de 12 kV. As análises de composição elementar do EDS foram usadas para se estimar as composições dos óxidos e camada de hidroxiapatita formada na superfície das amostras. Vale enfatizar que tais cálculos foram usados apenas para se comparar as amostras diferentes preparadas sob mesmas condições e analisadas sob mesma intensidade do feixe. Assim, tal comparação formece uma análise semi-quantitativa das variações ocorridas nessas amostras, porém, não se pode tomar os valores de composição dos óxidos obtidas como as composições reais das amostras. Para essa determinação, seria necessário fazer análises de EDS utilizando padrões desses óxidos ou a técnica de espectroscopia por dispersão de compreimento de onda (WDS), que fornece uma análise quantitativa dessas composições.

As amostras para TEM foram preparadas em grades de cobre de 400 mesh revestidas com película de carbono. As superfícies das grades foram pré-tratadas com uma mistura água/amônia e, então, as partículas dispersas na mistura água/etanol foram depositadas nas superfícies dessas grades. O diâmetro das partículas foi medido a partir das micrografias de TEM utilizando o software ImageJ. Duas grades foram preparadas e analisadas em oito regiões diferentes. Cada região foi dividida em nove áreas e, em cada área, foi medido o diâmetro de, pelo menos, três partículas, resultando em um mínimo de 432medições.

As análises de DLS foram realizadas no Depto. de Farmácia da UFMG em equipamento HS 3000 Zetasizer Data Type 1256 equipado com laser hélio/neon de 4 mW a 633 nm e ângulo de detecção de 173°. As medições de espalhamento de luz foram feitas a 25 ± 1°C e as medições hidrodinâmicas foram realizadas em 90°, após a diluição da amostra a 10 mg/mL em solução de NaCl 10 mM NaCl. Os dados foram analisados de acordo com o método cumulativo para o diâmetro médio aparente e índice de polidispersão (PDI), o valor final foi em média de 10 medições. Análises de potencial zeta foram realizadas para determinar a estabilidade das dispersões de nanopartículas em solução salina e dimetil sulfóxido (DMSO).

As isotermas de adsorção e dessorção de N_2 foram realizadas no Laboratório de Hidrometalurgia do Depto. de Engenharia Metalúrgica e de Materiais da UFMG a 77 K em um equipamento Quantachrome 9. A área superficial específica (SA) dos materiais foi determinada pelo método de Brunauer-Emmett-Teller (BET), utilizando pontos de dados de adsorção de pressão relativa (P/Po) na faixa de 0,01-0,30. Os tipos de isotermas obtidos foram avaliados de acordo com sua forma e tipo de histerese entre os modos de adsorção e dessorção.

Caracterização Mecânica

Os ensaios mecânicos do polímero e dos compósitos obtidos foram realizados no Laboratório de Engenharia de Polímeros e Compósitos no Depto. de Engenharia Metalúrgica e de Materiais da UFMG na Máquina Universal de Ensaios EMIC-DL 300 à temperatura ambiente com célula de carga de 50 N e, no mínimo, 5 corpos de prova para cada material. As membranas foram avaliadas por teste de tração, à velocidade de 20 mm/min, e as matrizes porosas por testes de compressão, à 5 mm/min.

Estudo da Bioatividade *in vitro*

Os materiais obtidos foram imersos em recipientes contendo uma solução que simula o fluido corpóreo (SBF) e mantidos à temperatura de 37°C por diferentes períodos de tempo para se avaliar a formação da camada de hidroxiapatita (HA) na superfície desse materiais.

A estrutura química e morfologia das superfícies dos amteriais após imersão em SBF foram analisadas por FTIR, XRD, MEV e EDS.

Medidas de potencial zeta foram realizadas nessas soluções, em períodos de 0, 6 e 24 horas, 3 e 7 dias. Cada ponto no gráfico representa os valores médios calculados com base na média de nove histogramas (n=9).

Ensaios Biológicos

Para ensaios biológicos, foram utilizados osteoblastos isolados da calvária de ratos Wistar machos com 1 a 5 dias de idade, obtidos no Centro de Bioterismo da UFMG. As células usadas nos experimentos eram de passagem dois.

Os biomateriais desenvolvidos, e seus produtos de degradação, passam por testes de citotoxicidade seguindo a norma ISO10993-5 de contato direto usando cultura de osteoblastos e avaliação da viabilidade celular pelos testes MTT, Resazurina e atividade de fosfatase alcalina. Os testes foram realizados no Instituto de Ciências Biológicas da UFMG.